HIGH EFFICIENCY DEVICES BASED ON SLOW LIGHT IN PHOTONIC CRYSTALS

A Thesis
Presented to
The Academic Faculty

by

Murtaza Askari

In Partial Fulfillment
of the Requirements for the Degree
Doctor of Philosophy in the
School of Electrical and Computer Engineering

Georgia Institute of Technology
May 2011

HIGH EFFICIENCY DEVICES BASED ON SLOW LIGHT IN PHOTONIC CRYSTALS

Approved by:

Professor Ali Adibi, Advisor
School of Electrical and Computer Engineering
Georgia Institute of Technology

Professor Thomas K. Gaylord
School of Electrical and Computer Engineering
Georgia Institute of Technology

Professor Andrew F. Peterson
School of Electrical and Computer Engineering
Georgia Institute of Technology

Professor Kenneth H. Sandhage
School of Material Science and Engineering
Georgia Institute of Technology

Asst. Professor Ying Zhang
School of Electrical and Computer Engineering
Georgia Institute of Technology

Date Approved: March 18, 2011

To my parents,

Mr. and Mrs. Mohsin Askari,

ACKNOWLEDGEMENTS

I want to thank my advisor, Dr. Adibi, who gave me the opportunity to come to his group and work under his supervision. I thank him for his kind words of acknowledgement and motivation and having me to worry about the finances. I also thank him for allowing me the freedom to work in research directions that I considered worthwhile pursuing. I want to thank all the members of Photonics Research Group in general for creating a motivating and congenial environment. In particular, I want to thank some of the seniors in this group (Dr. Babak Momeni, and Dr. Mohammad Soltani) whose guidance helped me a lot in the beginning years of my optics education. I also want to thank my peers in the group (Dr. Saeed Mohammadi, Dr. Majid Badieirostami, Ehsan Hosseini, and Ali A. Eftekhar) for their friendship, support, and technical discussion. I also wish to thank Dr. Charles M. Reinke for helping me run long simulations using his parallel version of FDTD code, without which half of my work will not have been possible. I am thankful to Dr. Siva for his kind words of advice related to both work and practical life. I also want to express my gratitude to Amir Atabaki, Maysam Chamanzar, Qing Li, Fengtao Wang for their friendship and support. I also want to thank Dr. Arash Kerbaschi for his career counseling. I am highly indebted to all my teachers at Georgia Institute of Technology. In particular, I want to sincerely thank Prof. Thomas K. Gaylord, Prof. John A. Buck, Prof. Stephen E. Ralph, and Prof. Rick Trebino for teaching all I know about Optics. I want to thank Prof. Andrew F. Peterson and Prof. Glenn Smith for their inspirational teaching of electromagnetic courses. I also wish to thank Prof. Brian Kennedy and Prof. Phillip First from the Physics department. I also want to thank my other friends in Georgia Tech and in

Atlanta: Dr. Messam Abbas, Dr. Manzar Abbas, Azhar Hasan, Dr. Adeel Khalid, Dr. Abubakr Muhammad, Wasif Khawaja, Ali Asmi, Faheem Hussain, Hamza Faraz, Syed Ali Hassan, Hussain Raza, and Baqar Nasir for making my stay in Atlanta a pleasing experience. Special thanks to Dr. Messam Naqvi and Dr. Adeel Khalid for helping me in the beginning to settle down in Atlanta. I also want to express my gratitude to my relatives in US; my brother Raza Askari for his financial support in the last couple of years; my uncle Dr. Zameer Hasan for his guidance and support before and during my doctoral studies; my cousin Asma Raza and her family for their support. I am most indebted to my parents Mr. Mohsin Askari and Mrs. Night Mohsin, for instilling in me the value of knowledge and learning; for their love, support and motivation. I wish to thank them for their selfless, and tireless efforts to see me succeed. I want to thank my wife Shoa Mansoor for bearing with a poor graduate student for almost three years of her life; for her love, support and motivation. For making me reflect inside to be a better person. I also want to thank my in-laws for their love and support. In the end, I thank my most prized possession, my son Kumail M. Askari, for his innocence, smile, love, and his ability to turn my gloomy and depressing days into fun.

TABLE OF CONTENTS

LIST OF TABLES

LIST OF FIGURES

LIST OF SYMBOLS OR ABBREVIATIONS

2D Two dimensional.

3D Three dimensional.

AM-PCPML Adiabatically matched photonic crystal PML.

BOE Buffered oxide etch.

CPO Coherent population oscillation.

CROW Coupled resonator optical waveguide.

DBP Delay bandwidth product.

DBR Distributed Bragg reflector.

EIT Electromagnetically induced transparency.

FDTD Finite-difference time-domain.

FFT Fast Fourier transform.

FSR Free spectral range.

GVD Group velocity dispersion.

HPML Homogeneous perfectly matched layer.

IHC Interface hole cut.

MZI Mach-Zahnder interferometer.

NC Butt coupled.

NRC Nanotechnology Research Center.

PBG Photonic band gap.

PC Photonic crystal.

PCPML Photonic crystal PML.

PCW Photonic crystal waveguide.

PML Perfectly matched layer.

PWE Plane-wave expansion.

Q Quality factor of a resonator.

RI Refractive index.

RIU Refractive index unit.

SEM Scanning electron microscope.

SOI Silicon on insulator.

SU-8 A negative tone photoresist.

TE Transverse electric.

TM Transverse magnetic.

SUMMARY

Photonic crystals have allowed unprecedented control of light and have allowed bringing new functionalities on chip. Photonic crystal waveguides (PCWs), which are linear defects in a perfect crystal, have unique features that distinguish these waveguides from other waveguides. The unique features include very large dispersion, existence of slow light, and the possibility of tailoring the dispersion properties for guiding light. In my research, I have looked into some of the challenges in using slow light in PCWs. I have also demonstrated a sample application of refractive index sensing to show the promise the field of PCWs hold.

CHAPTER I

INTRODUCTION

Photonic crystals (PCs) are periodic dielectric structures. The periodicity can be in one, two or three dimensions. The periodicity results in unique features for light generation and propagation, which are not possible in bulk materials. One of the unique properties, exhibited by PCs, is the existence of photonic band gaps (PBGs). A PBG is a range of frequencies for which light cannot propagate inside the PC. By creating defects in a perfect PC light can be confined. For example, a point defect in a PC will confine light (with frequency inside the PBG) in three dimensions; a linear defect, in two dimensions; and a planer defect, in one dimension.

Two dimensional (2D) photonic crystals (PCs), in particular, have inspired great interest because of their ease of fabrication. By creating a linear defect in a 2D PC, we can make photonic crystal waveguides (PCWs). In these PCWs light with frequency within the PBG can be guided. For a certain range of frequencies and with certain geometric parameters of the PCW we can have slow light in these PCWs. At these slow light frequencies, light propagates at velocities less than that in a bulk material. The existence of slow light in PCWs has many applications in the field of optics, but there are challenges associated in using it. The subject of this research is to overcome the challenges in using slow light in PCWs, and to design high efficiency devices based on the slow light in PCWs.

1.1 Photonic Crystals

Since the advent of quantum mechanics and the demonstration of existence of matter waves, physicists have widely benefited from the concepts and theoretical foundations of optics and electromagnetism (EM). Seldom has optics community borrowed concepts from the physicists. Photonic crystals (PCs) [13, 14], in this sense, are an anomaly, where the optics community has immensely benefited from the vast knowledge in the areas of solid state and condensed matter physics. PCs are unique optical materials in which the dielectric permittivity (ϵ_r) or the refractive index (n) changes periodically. This periodicity and the close resemblance between Maxwell's equations and Schrodinger's equation result in the observation of similar phenomena for electromagnetic waves in PCs [15], as have previously been observed for electronic waves in crystals. For example - similar to electronic band gaps in semiconductor crystals - photonic band gaps (PBGs) appear in PCs with sufficiently large refractive index contrast between its constituent materials. A PBG is a range of frequencies in which no photon with frequency within that range can exist inside the PC.

It is not entirely unexpected that one of the most widely used methods for numerical studies of PCs, the plane-wave expansion (PWE) method [16, 17, 15], has been adapted from the modeling of electronic waves in a crystal. The PWE method uses the frequency domain to solve an eigen-value problem to find eigen-frequencies (ω) which can propagate inside the PC for a given wavevector (k). This method is used to calculate dispersion and the field profile of the modes in PCs. The other most widely used method, the finite difference time domain (FDTD) method [18, 19], is used to study the temporal behavior of fields inside the PCs. The PC community also uses methods based on the diffraction grating model [20, 21, 22]. These methods are used to study phenomena occurring at the interface of a homogeneous and a periodic medium, or the propagation of the fields through

PCs with finite dimension.

Although the study of PCs started with the desire to control the spontaneous emission of atoms in three dimensions [13], the interest in PCs is no longer limited to this application. Similarly, the technological challenges in fabricating three dimensional (3D) PCs and their not so easy integration with current integrated electrical/optical technology, have spurred interest in their two dimensional (2D) counterparts, which can easily be fabricated with the mature semiconductor fabrication techniques. Since the pioneering works of Eli Yablonovitch [13] and Sajeev John [14], huge advances have been made in controlling the propagation of electromagnetic fields inside a PC. Applications of PCs can be broadly categorized in two areas: (i) PBG based devices and (ii) non-PBG based devices. For PBG based devices, PCs have been used as reflective planes for antennas [23], 3D and 2D waveguides [24, 25], resonators [26], high extraction LEDs [27, 28], and low threshold lasers [29, 30]. Similarly for non-PBG based devices, novel phenomena such as superprism [31, 32], negative diffraction [33, 34], and ultra-refraction [35, 32] have been demonstrated in PCs.

1.2 Slow Light

The incredible speed of light and its non-interaction with matter has been of great benefit to mankind. It has allowed us to look deeper into our galaxy and universe, and to transmit data over long distances using optical fibers. On the other hand, slow light has its own benefits and has several applications in areas, such as nonlinear optics, optical switching, optical buffering and quantum optics [36].

When light is slowed down, its energy density gets scaled by the group index or the slow down factor [37]. Nonlinear effects depend on optical intensities; therefore the nonlinear interactions also scale with the slow down factor. By appropriately designing slow light waveguides, the efficiency of Raman amplification

has been enhanced by a factor of 10,000 [38]. Similarly, the size of an integrated thermo-optic switch has been reduced by an order of magnitude using slow light [39]. For quantum information processing, storing the quantum state of light is important. It has been shown that pulses of light can be stored in a Bose-Einstein condensate without loss of their quantum properties [40].

Light has been slowed down to unimaginably small numbers such as 17 m/s using electromagnetically induced transparency (EIT) in an ultra-cold atomic gas [41], and to 90 m/s in a room temperature solid using coherent population oscillation (CPO) [42]. These techniques (EIT and CPO) utilize material resonances that inhibit wavelength tunability. Other drawbacks include low transmission, low bandwidth (at most kHz), complicated experimental setup, and/or extreme low temperatures. Similarly, these techniques do not allow integration on a chip. Rather than using material resonances, light can also be slowed down using structural resonance, such as in coupled resonator optical waveguides (CROWs) [43]. In a CROW, light hops from one resonator to another and the quality factor (Q) controls how much time light spends in each resonator. CROWs have been implemented in a microring architecture [44, 45] or using photonic crystals cavities [46, 47]. Delay lines based on CROWs have been theoretically studied [48, 49] and experimentally demonstrated [50, 51, 52]. Although CROWs allow tunability of the wavelength, by merely changing the size of the resonator, these CROWs require very fine control of the resonances of multiple resonators and the coupling coefficients between them [49]. This precise control of resonance is almost impossible to achieve with current fabrication technology.

Photonic crystal waveguide (PCW) based delay lines, rather than using material or structural resonances, rely on the dispersion of the guiding region. The strong dispersion in PCWs arises due to the periodicity of the PCW. This dispersion can be engineered by modifying the size and location of the holes [53, 54, 55].

PCW based delay lines offer the advantages of large bandwidth, wavelength tunability, ease of fabrication using current fabrication techniques, inherently lossless operation [56], and scalability of delay with the length of structure. Delay lines based on PCWs have already been reported with one of the largest delay bandwidth products (DBP) [57], a figure of merit for slow light devices.

Any new opportunity comes with unique challenges. Using slow light in PCWs is no different. A few of the issues associated with using slow light in PCWs are as follows:

1. Low coupling efficiency from a ridge waveguide to small group velocity modes in PCWs.

2. Bends in PCWs suffer from low transmission and large dispersion at small group velocities.

3. Challenges in FDTD simulation of PCWs such as:

    - Large simulation times required for simulating pulse propagation at small group velocities.
    - Absorbing boundary conditions reported in literature do not work well in absorbing dispersive and small group velocity waves. As a result reflections from these absorbing boundary conditions compromise the validity of the FDTD simulations.

To reap full benefits of PCWs, these challenges need to be overcome. In this research, I have addressed these issues and have demonstrated high efficiency, compact and highly sensitive refractive index sensors.

The thesis is organized in the following way. In the first chapter, I briefly explain the simulation methods that I have used for my research. The second chapter, talks about the fabrication method used to fabricate PCW structures in this

research. The next four chapters discuss our methods of solving the issues (as mentioned above) associated with the use of slow light in PCWs. For example, Chapter 6 tackles the low coupling efficiency of small group velocity modes to ridge waveguide modes. Chapter 5 mentions our method of overcoming low transmission and large dispersion issues with PCW bends. Chapters 4 and 7 go into details of our proposed solutions to the issues related with the FDTD simulation of PCWs. Chapter 7, for example, talks about our proposed absorbing boundary condition for FDTD simulations, and Chapter 4 talks about our analytical modeling of PCWs to reduce the large pulse propagation simulations times required for FDTD simulations to seconds. In Chapter 8 we present an example of a high efficiency device based on slow light in PCWs. We present our design and experimental demonstration of highly compact, high sensitivity refractive index sensors based on slow light in PCWs. All the chapters are self consistent and the reader can directly go to any chapter without having to read other chapters before it.

CHAPTER II

SIMULATION METHODS FOR PHOTONIC CRYSTAL WAVEGUIDES

The two most widely used methods for numerical studies of PCs are the plane wave expansion (PWE) method [16, 17, 15] and the finite-difference time-domain method [19]. I have extensively used these methods for simulating my structures in this research. In this chapter, I will briefly describe these two methods.

The mathematical foundation of optics lies on Maxwell's equations. The beauty of these equations is that these are valid from DC (direct current) or zero frequency all the way to cosmic rays (10^{14} GHz) and beyond. For PCs that are composed of lossless ($\sigma = 0$) and non-magnetic ($\mu = \mu_o$) dielectrics, the Maxwell's equations can be written as [58]:

$$\nabla \times \mathbf{E} + \mu_o \frac{\partial \mathbf{H}}{\partial t} = 0 \quad (1)$$

$$\nabla \times \mathbf{H} - \epsilon_0 \epsilon_r \frac{\partial \mathbf{E}}{\partial t} = 0 \quad (2)$$

$$\nabla \cdot [\epsilon_r \mathbf{E}] = 0 \quad (3)$$

$$\nabla \cdot \mathbf{H} = 0 \quad (4)$$

2.1 Plane-wave Expansion Method

It is not entirely unexpected that one of the most widely used methods for numerical studies of PCs, the plane-wave expansion (PWE) method [16, 17, 15], has been adapted from the modeling of electronic waves in a crystal. The PWE method uses the frequency domain to solve an eigen-value problem to find eigen-frequencies (ω) which can propagate inside the PC for a given wavevector (k). This method is

used to calculate dispersion and the field profile of the modes in PCs. In the PWE method we solve Maxwell's equations in the frequency domain. We consider time harmonic variation of fields, i.e. fields with time variation of the form exp(-iωt), where ω is the frequency of the temporal oscillations. With this temporal behavior, all the time derivatives can be replaced by $-i\omega t$. Equations. 1 and 2 take on the following form:

$$\nabla \times \mathbf{E} - i\omega\mu_o\mathbf{H} = 0 \tag{5}$$

$$\nabla \times \mathbf{H} + i\omega\epsilon_0\epsilon_r\mathbf{E} = 0 \tag{6}$$

Taking the curl of Eq. 5 and using Eq. 6 and vice versa we get the following:

$$\frac{1}{\epsilon_r}\nabla \times \nabla \times \mathbf{E} - \frac{\omega^2}{c^2}\mathbf{E} = 0 \tag{7}$$

$$\nabla \times \frac{1}{\epsilon_r}\nabla \times \mathbf{H} - \frac{\omega^2}{c^2}\mathbf{H} = 0 \tag{8}$$

where c = $1/\sqrt{\epsilon_o\mu_o}$ is the speed of light in vacuum.

The above two equations are an example of eigen-value problem with $\frac{\omega^2}{c^2}$ as the eigen-values. In PWE method, we solve one of these eigen-value equations to obtain the eiqen frequencies (ω) of the structure. The corresponding eigenvectors give us field profile corresponding to the eigen-frequency. In the PWE method, we assume that our structure is infinitely periodic. That is,

$$\epsilon_r(\mathbf{r}) = \epsilon_r(\mathbf{r} + \sum_{i=1,N} n_i\mathbf{a}_i) \tag{9}$$

for any value of integer n_i. In the above equation, $\mathbf{a}_i$'s are the lattice vectors and N could be either 1; 2; or 3 depending on whether it is one; two; or three dimensional periodic structure. In my case, I have used two dimensionally periodic structures so the value of N is 2. Since the structure is periodic, we can expand ϵ_r or $\frac{1}{\epsilon_r}$ in the

form of a Fourier series. For example, $\frac{1}{\epsilon_r}$ can be written as:

$$\frac{1}{\epsilon_r(\mathbf{r})} = \sum_{\mathbf{G}} \kappa(\mathbf{G}) \exp(i\mathbf{G}.\mathbf{r}), \tag{10}$$

where $\kappa(\mathbf{G})$'s are the coefficients of Fourier expansion and $\mathbf{G}$'s correspond to lattice vectors in the reciprocal space. A reciprocal lattice vector can be expressed as a linear combination of primitive reciprocal lattice vectors $\mathbf{b}_i$s, such that:

$$\mathbf{G} = \sum_{i=1,N} l_i \mathbf{b}_i, \tag{11}$$

where l_i's are arbitrary integers. As above N can be 1, 2 or 3 depending on the dimensionality of the periodicity. The primitive reciprocal lattice vectors $\mathbf{b}_i$'s are given by:

$$\mathbf{a}_i \cdot \mathbf{b}_j = 2\pi\delta_{ij}. \tag{12}$$

Since ϵ is a periodic function of the spatial coordinate $\mathbf{r}$, the Bloch theorem [59, 16, 15] allows us to choose eigen-functions of the form:

$$\mathbf{H}(\mathbf{r}) = \mathbf{H}_{\mathbf{k}n}(\mathbf{r}) = \mathbf{u}_{\mathbf{k}n}(\mathbf{r}) \exp(i\mathbf{k}.\mathbf{r}) \tag{13}$$

where $\mathbf{u}_{\mathbf{k}n}(\mathbf{r})$ is periodic and has the same periodicity as the PC. In the above equation, $\mathbf{k}$ is the wavevector in the first Brillouin zone ($-\pi \leq \mathbf{k}.\mathbf{a_i} \leq \pi$) and n is the band index. Since $\mathbf{u}_{\mathbf{k}n}(\mathbf{r})$ is periodic, it can also be expanded in the Fourier series similar to $\frac{1}{\epsilon}$ itself. Hence, Eq. 13 can be written as:

$$\mathbf{H}_{\mathbf{k}n}(\mathbf{r}) = \sum_{\mathbf{G}} \mathbf{H}_{\mathbf{k}n}(\mathbf{G}) \exp(i(\mathbf{k}+\mathbf{G}).\mathbf{r}) \tag{14}$$

Using Eq. 14 and 10 in Eq. 8, we get:

$$\nabla \times \sum_{\mathbf{G}^\dagger} \kappa(\mathbf{G}^\dagger) \nabla \times \sum_{\mathbf{G}^*} \mathbf{H}_{\mathbf{k}n}(\mathbf{G}^*) \exp(i(\mathbf{k}+\mathbf{G}^*+\mathbf{G}^\dagger).\mathbf{r}) = \frac{\omega_{\mathbf{k}n}^2}{c^2} \sum_{\mathbf{G}} \mathbf{H}_{\mathbf{k}n}(\mathbf{G}) \exp(i(\mathbf{k}+\mathbf{G}).\mathbf{r}) \tag{15}$$

where $\omega^2_{\mathbf{k}n}$ is the eigen-frequency of $\mathbf{H}_{\mathbf{k}n}(\mathbf{r})$. With $\mathbf{G}^\dagger + \mathbf{G}^* = \mathbf{G}$, the above equation becomes:

$$\nabla \times \sum_{\mathbf{G}} \kappa(\mathbf{G} - \mathbf{G}^*) \nabla \times \sum_{\mathbf{G}^*} \mathbf{H}_{\mathbf{k}n}(\mathbf{G}^*) \exp(i(\mathbf{k} + \mathbf{G}).\mathbf{r}) = \frac{\omega^2_{\mathbf{k}n}}{c^2} \sum_{\mathbf{G}} \mathbf{H}_{\mathbf{k}n}(\mathbf{G}) \exp(i(\mathbf{k} + \mathbf{G}).\mathbf{r}) \tag{16}$$

Using the relation $\nabla \times (\mathbf{V} \exp(i\mathbf{u}.\mathbf{r})) = i\mathbf{u} \times \mathbf{V} \exp(i\mathbf{u}.\mathbf{r})$ twice in the above equation, we get:

$$-\sum_{\mathbf{G}} \sum_{\mathbf{G}^*} \kappa(\mathbf{G} - \mathbf{G}^*)(\mathbf{k} + \mathbf{G}) \times [(\mathbf{k} + \mathbf{G}) \times \mathbf{H}_{\mathbf{k}n}(\mathbf{G}^*)] \exp(i(\mathbf{k} + \mathbf{G}).\mathbf{r}) = \frac{\omega^2_{\mathbf{k}n}}{c^2} \sum_{\mathbf{G}} \mathbf{H}_{\mathbf{k}n}(\mathbf{G}) \exp(i(\mathbf{k} + \mathbf{G}).\mathbf{r}) \tag{17}$$

Projecting the above equation on the basis functions $\exp(i(\mathbf{k} + \mathbf{G}).\mathbf{r})$, where $\mathbf{G}$ is one of the reciprocal lattice vectors as in Eq. 11, gives:

$$\sum_{\mathbf{G}^*} \kappa(\mathbf{G} - \mathbf{G}^*)(\mathbf{k} + \mathbf{G}) \times [(\mathbf{k} + \mathbf{G}) \times \mathbf{H}_{\mathbf{k}n}(\mathbf{G}^*)] = -\frac{\omega^2_{\mathbf{k}n}}{c^2} \mathbf{H}_{\mathbf{k}n}(\mathbf{G}) \tag{18}$$

By solving this equation numerically, we can find the eigen-values ($\omega^2_{\mathbf{k}n}$) and eigen-functions ($\mathbf{H}_{\mathbf{k}n}(\mathbf{r})$) of the PC for a given wavevector ($\mathbf{k}$) in the first Brillouin zone. We can then generate the dispersion relation by plotting $\omega^2_{\mathbf{k}n}$ vs. $\mathbf{k}$.

2.1.1 2D PWE Method

All the equations presented till now are generic and can be used for problems with any dimensionality (i.e., 1, 2 or 3 dimensions). Since I have used 2D PWE, from this point onwards, I will talk specifically about the 2D case. In the 2D case, we assume the structure to be uniform in the third direction (e.g. z-direction). As a result of this non-variation along z-axis all the derivatives w.r.t z vanish when we restrict the propagation in the x-y plane or the plane of periodicity. When we replace the

z derivatives with zero in the vectorial Eqs. 5 and 6, these equations decouple into two independent sets of equations:

$$\begin{aligned} \frac{\partial}{\partial y}E_z(\mathbf{r}) &= i\omega\mu_o H_x(\mathbf{r}) \\ \frac{\partial}{\partial x}E_z(\mathbf{r}) &= -i\omega\mu_o H_y(\mathbf{r}) \\ \frac{\partial}{\partial x}H_y(\mathbf{r}) - \frac{\partial}{\partial y}H_x(\mathbf{r}) &= -i\omega\epsilon_o\epsilon_r E_z(\mathbf{r}), \end{aligned} \tag{19}$$

and

$$\begin{aligned} \frac{\partial}{\partial y}H_z(\mathbf{r}) &= -i\omega\epsilon_o\epsilon_r E_x(\mathbf{r}) \\ \frac{\partial}{\partial x}H_z(\mathbf{r}) &= i\omega\epsilon_o\epsilon_r E_y(\mathbf{r}) \\ \frac{\partial}{\partial x}E_y(\mathbf{r}) - \frac{\partial}{\partial y}E_x(\mathbf{r}) &= i\omega\mu_o H_z(\mathbf{r}). \end{aligned} \tag{20}$$

Equation 19 refers to a TE mode of the 2D PC where the electric field is along z-axis, and Eq. 20 refers to the TM modes of the 2D PC, where the electric field is in the x-y plane. Note that in the literature TE/TM are used interchangeably for the same polarization. When we eliminate E_x and E_y from the set of Eqs. 20, we get the following:

$$\mathscr{P}_H H_z(\mathbf{r}) \equiv \left\{ \frac{\partial}{\partial x}\frac{1}{\epsilon_r}\frac{\partial}{\partial x} + \frac{\partial}{\partial y}\frac{1}{\epsilon_r}\frac{\partial}{\partial y} \right\} H_z(\mathbf{r}) = \nabla \cdot \left\{ \frac{1}{\epsilon_r}\nabla H_z(\mathbf{r}) \right\} = -\frac{\omega^2}{c^2}H_z(\mathbf{r}) \tag{21}$$

where $\mathscr{P}_H$ is the differential operator as defined in the equality. As Eq. 8, the above equation presents itself as an eigen-value problem with $\mathscr{P}_H$ as an eigen operator and $-\frac{\omega^2}{c^2}$ as the eigen-value, with ω as the eigen-frequency. The above differential operator can be converted into an algebraic operator by using the Bloch form for H_z (where $H_{z,\mathbf{k}n}(\mathbf{r}) = \sum_{\mathbf{G}} H_{z,\mathbf{k}n}(\mathbf{G}) \exp(i(\mathbf{k}+\mathbf{G}).\mathbf{r})$, similar to the expansion in Eq. 14) and Eq. 10 in the above equation with the understanding that now **r**, **k**, and

G are two dimensional (and lie in the x-y plan). With these substitutions and using a similar procedure as outlined from Eq. 15 – Eq. 18 with the exception that we now use the relations $\nabla\left(V\exp(i\mathbf{u}.\mathbf{r})\right) = i\mathbf{u}Vexp(i\mathbf{u}.\mathbf{r})$ and $\nabla\cdot(\mathbf{u}V\exp(i\mathbf{q}.\mathbf{r})) = i\mathbf{q}.\mathbf{u}V\exp(i\mathbf{q}.\mathbf{r})$ rather than $\nabla\times(\mathbf{V}\exp(i\mathbf{u}.\mathbf{r})) = i\mathbf{u}\times\mathbf{V}\exp(i\mathbf{u}.\mathbf{r})$, we get the following algebraic form for the eigen-value problem.

$$\sum_{\mathbf{G}^*}\kappa(\mathbf{G}-\mathbf{G}^*)(\mathbf{k}+\mathbf{G})\cdot(\mathbf{k}+\mathbf{G}^*)H_{z,\mathbf{k}n}(\mathbf{G}^*) = \frac{\omega_{\mathbf{k}n}^2}{c^2}H_{z,\mathbf{k}n}(\mathbf{G}) \tag{22}$$

where $\omega_{\mathbf{k}n}$ and $H_{z,\mathbf{k}n}$ denote the eigen-frequency and eigen-mode respectively. The above equation is the eigen-value equation for the TM modes of the 2D-PC. Here I have concentrated on the derivation of the TM eigen-value equation, since I have used a triangular lattice PC for my research and this triangular lattice PC has a TM band gap. The eigen-value equation for the TE modes (E_z) can be derived in a similar manner. Here I just quote the result:

$$\sum_{\mathbf{G}^*}\kappa(\mathbf{G}-\mathbf{G}^*)|(\mathbf{k}+\mathbf{G})|^2E_{z,\mathbf{k}n}(\mathbf{G}^*) = \frac{\omega_{\mathbf{k}n}^2}{c^2}E_{z,\mathbf{k}n}(\mathbf{G}). \tag{23}$$

The above equations are mostly used to write the numerical codes for obtaining the dispersion and modes of PCs and PCWs.

2.1.1.1 Some Implementation Details

In this section, I will talk about some implementation details for writing a numerical code in Matlab for calculating band structure of the PCs and PCWs.

The first step in calculating the band structure is finding the Fourier coefficients in the Fourier series expansion of $\frac{1}{\epsilon}$. The inverse Fourier transform is used to calculate the coefficients.

$$\kappa(\mathbf{G}) = \frac{1}{V_o}\int_{V_o}\frac{1}{\epsilon(\mathbf{r})}\exp(-i\mathbf{G}.\mathbf{r})d\mathbf{r} \tag{24}$$

This integral can be calculated numerically. For cases with rectangular unit cells we can use Matlab's fft2() function. This function takes the 2D Fourier transform of the input. For example, for my PCWs I have used this fft2() function to calculate the Fourier coefficients for my unit cell. The unit cells for (i) a PC consisting of a triangular lattice of air columns in Si, and (ii) a PCW defined by removing one row or air holes in the PC are shown in Figure 1. Since the unit cell for the PCW is rectangular, the Fourier coefficients for this case can be calculated by using fft2() function of Matlab.

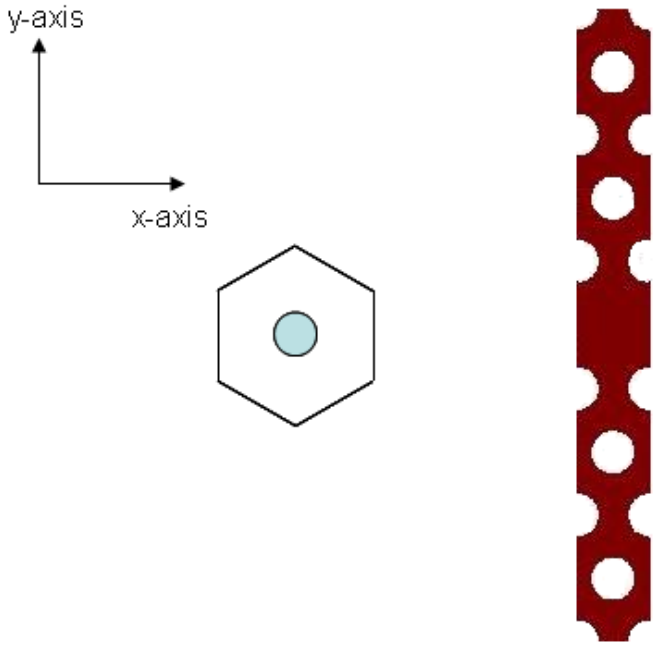

(a) (b)

Figure 1: (a) Unit cell of a PC consisting of a triangular lattice of air columns in Si. (b) Unit cell of a PCW in the triangular lattice PC of (a).

For simple enough unit cells (e.g., a 3D crystal with a unit cell consisting of one dielectric sphere or a 2D crystal with a unit cell consisting of one circular dielectric rod, as in case of the PC of Figure 1(a)) Eq. 24 can be computed analytically. I will only present the analytical solution of this equation for the 2D case of a circular

dielectric rod. For the 3D case of a dielectric sphere see Ref. [16, 15]. For the 2D case V_o in Eq. 24 represents the area of the unit cell. The dielectric function in the 2D case can be written as:

$$\frac{1}{\epsilon(\mathbf{r})} = \frac{1}{\epsilon_b} + \left(\frac{1}{\epsilon_a} - \frac{1}{\epsilon_b}\right)\mathcal{S}(\mathbf{r}), \tag{25}$$

where $\mathcal{S}(\mathbf{r})$ is given by:

$$\mathcal{S}(\mathbf{r}) = \begin{cases} 1 & \text{for } |\mathbf{r}| \leq r_a, \\ 0 & \text{for } |\mathbf{r}| > r_a. \end{cases} \tag{26}$$

Using Eq.s 25 and 26 in Eq. 24, we get

$$\kappa(\mathbf{G}) = \frac{1}{\epsilon_b}\delta_{\mathbf{G}0} + \frac{1}{V_o}\left(\frac{1}{\epsilon_a} - \frac{1}{\epsilon_b}\right)\int_{V_o} \mathcal{S}(\mathbf{r})\exp(-i\mathbf{G}.\mathbf{r}). \tag{27}$$

The integral in the above equation can be solved by using polar coordinates and assuming the angle between $\mathbf{G}$ and $\mathbf{r}$ to be φ (which implies $\mathbf{G}.\mathbf{r} = Gr\cos(\varphi) = -Gr\sin(\varphi - \frac{\pi}{2})$). For $\mathbf{G} \neq 0$, the integral in the above equation can be written as:

$$\begin{aligned} &\int_{V_o} \mathcal{S}(\mathbf{r})\exp(-i\mathbf{G}.\mathbf{r})d\mathbf{r} \\ &= \int_0^{r_a}\int_0^{2\pi} r\exp\{iGr\sin(\varphi - \frac{\pi}{2})\}\partial\varphi\partial r \\ &= \int_0^{r_a}\int_0^{2\pi} r\sum_{l=-\infty}^{\infty}\mathcal{J}_l(Gr)\exp\{il(\varphi - \frac{\pi}{2})\}\partial\varphi\partial r \\ &= 2\pi\int_0^{r_a}\mathcal{J}_0(Gr), \end{aligned} \tag{28}$$

where $G = |\mathbf{G}|$ and $\mathcal{J}_l$ is the Bessel function of the l^{th} order. Going from second to third equality in Eq. 28, I have used the following relation:

$$\exp(iw\sin\phi) = \sum_{l=-\infty}^{\infty}\mathcal{J}_l(w)\exp(il\phi). \tag{29}$$

If we further use the relation,

$$\{w\mathcal{J}_1(w)\}' = w\mathcal{J}_0(w), \tag{30}$$

we obtain from Eq. 28

$$\int_{V_o} \mathcal{S}(\mathbf{r}) \exp(-i\mathbf{G}.\mathbf{r}) d\mathbf{r} = \frac{2\pi r_a}{G} \mathcal{J}_1(Gr_a). \tag{31}$$

We can denote the area fraction of the circular rod by

$$f = \frac{\pi r_a^2}{V_o}. \tag{32}$$

Now, using Eq.s 31 and 32 in Eq. 27, we get for $\mathbf{G} \neq 0$

$$\kappa(\mathbf{G}) = 2f \left(\frac{1}{\epsilon_a} - \frac{1}{\epsilon_b} \right) \frac{\mathcal{J}_1(Gr_a)}{Gr_a}, \tag{33}$$

and for $\mathbf{G} = 0$,

$$\kappa(0) = \frac{f}{\epsilon_a} + \frac{f-1}{\epsilon_b}. \tag{34}$$

The second step in the implementation is setting up a matrix representation of the the system of algebraic equations as given in Eq. 22. The coefficients of $H_{z,\mathbf{k}n}(\mathbf{G})$ make up the matrix with $\mathbf{k}$ as the input. The matrix is then passed as an argument to the Matlab function eig() to obtain the eigen-values ($\frac{\omega_{\mathbf{k}n}^2}{c^2}$) and eigen-vectors ($H_{z,\mathbf{k}n}(\mathbf{G})$) corresponding to the input value of $\mathbf{k}$. The input $\mathbf{k}$ is varied along the high-symmetry directions to obtain the dispersion. To obtain the eigen-mode (H_z) of the structure at a given frequency ($\omega_{\mathbf{k}n}$) and $\mathbf{k}$, we solve the Bloch representation of H_z, similar to Eq. 14, with coefficients ($H_{z,\mathbf{k}n}(\mathbf{G})$) of the expansion already obtained. E_x and E_y fields can be calculated by using the first two equations of the set of Eqs. 20.

The above procedure is used to calculate the bandgap of the triangular lattice PC of air rods in Si. For PCWs, I have used the above procedure to obtain both the

dispersion of the guided modes of the PCW as well as the mode profile for these modes[1].

Figure 2 shows the band diagram of a triangular lattice of air holes in Si. The radius of air holes is 30% of the lattice constant. The epsilon used for Si is 7.9. The real space triangular lattice and the Brillouin zone are shown as an inset. The shaded region in the Brillouin zone is the irreducible Brillouin zone. Also indicated alongside the Brillouin zone are the high symmetry points (Γ, M and K). The band diagram is calculated by varying the wavevector (k) along the lines connecting the high symmetry points.

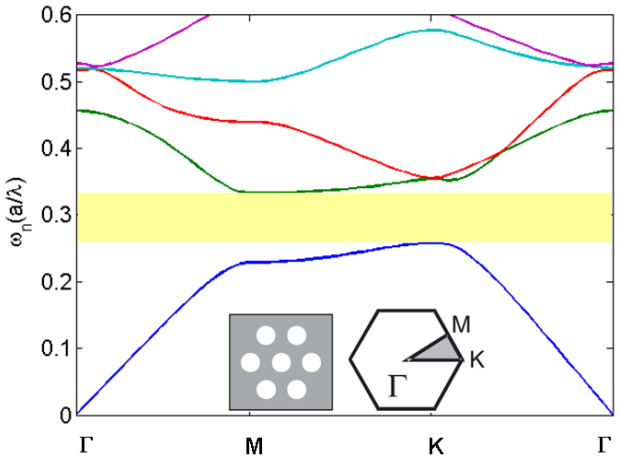

Figure 2: Band diagram of a triangular lattice of air holes in Si. The radius of air holes is 0.3 times the lattice constant. The effective epsilon used for calculating the band diagram for Si is 7.9. The yellow rectangle specifies the bandgap region. The inset shows the real space (left) and the Brillouin zone (right) of the triangular lattice PC.

Similarly, I have used my PWE code to generate the dispersion diagram and the field profile for the modes of a PCW defined in the PC with parameters as outlined in the above paragraph. Numerous examples of the dispersion diagram and field profile for the PCW used in this research are shown in the following chapters.

[1]E-mail the author at murtazaaskari@gmail.com to get working Matlab codes for 2D PWE method.

2.2 *Finite-difference Time-domain Method*

The finite-difference time-domain (FDTD) method [19], in contrast to the PWE method, solves the Maxwell's curl equations (Eqs. 1 and 2) in the time domain. The FDTD method is much more versatile and powerful than the PWE method in the sense that FDTD allows you to simulate any structure, whether the structure is periodic or non-periodic. The simulation of infinitely periodic structures structures in FDTD requires use of special boundary conditions (periodic boundary conditions). Since there are no matrix inversions to be performed, there is no inherent limit on the size of the problem that can be simulated with FDTD. It is also relatively straight forward to cast the bigger FDTD problems into the parallel computation realm. One of the big advantages of the FDTD method is that it allows calculating the wideband frequency response of the structures using just one simulation.

I have extensively used FDTD method in my research. I have used it to obtain the dispersion diagram of a PCW. I have used it to obtain wideband frequency response of PCW bends and ridge to PCW couplers. I have also used it to obtain the transmission and reflection characteristics of ridge to PC waveguide couplers in time domain. I have also used it to study the effect of dispersion on a pulse propagating through a PCW at different center frequencies (i.e. with different group velocities).

The interest in FDTD has grown tremendously since the seminal work of Yee [18]. Although numerous enhancements and additions to the original Yee's formulation have been presented for increasing the stability and accuracy of the FDTD method, I will mostly limit myself to Yee's formulation in this section as I have used this formulation throughout my research. An excellent treatment of Yee's original formulation and other enhancements can be found in Ref. [19]. In the following, I will present a modified version of the treatment presented in Ref. [19].

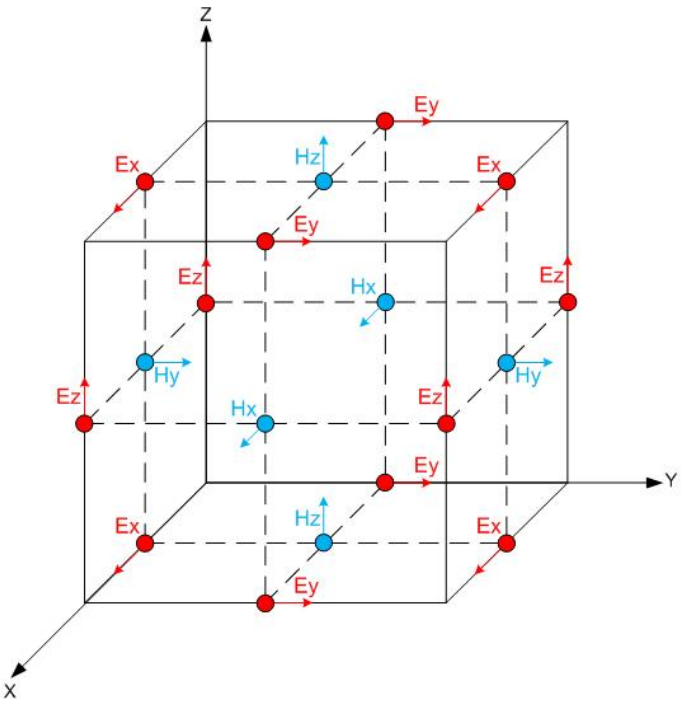

Figure 3: The cubic unit cell used in Yee's algorithm for discretizing the simulation domain. Also shown are the (E) and (H) components and their spatial staggering as implemented in the algorithm.

Yee's algorithm starts with discretizing the simulation domain into unit cells, similar to one shown in Figure 3[2]. Yee's algorithm staggers the **E** and **H** fields in the unit cell in such a manner that each (E) component is surrounded by four circulating (H) components and vice versa. Yee algorithm also staggers the (E) and (H) components in time domain in what is commonly known as the leapfrog arrangement. In the leapfrog arrangement, all (E) components are computed and stored using previously computed (H) components. The (H) components are then calculated and stored using the recently computed (E) components. This cycle continues until the simulation finishes.

[2]Image taken from `http://fdtd.wikispaces.com/The+Yee+Cell`. Downloaded 02/201

2.2.1 Finite Differences and Notations

Before I go into the details of FDTD method, it is useful to mention the notation that will be used extensively in presenting the mathematical formulation of FDTD. Any function u of space and time evaluated at a specific point in space and time is denoted as

$$u(i\Delta x, j\Delta y, k\Delta z, n\Delta t) = u^n_{i,j,k}, \tag{35}$$

where Δt is the increment in time and $\Delta x, \Delta y$ and Δz are the spatial increments. Yee'a algorithm uses centered finite-difference (central-difference) for the both the space and time derivatives. These central-differences are second-order accurate. Examples of central-differences in spatial and time derivatives are

$$\frac{\partial u}{\partial x}(i\Delta x, j\Delta y, k\Delta z, n\Delta t) = \frac{u^n_{i+1/2,j,k} - u^n_{i-1/2,j,k}}{\Delta x} + \mathcal{O}[(\Delta x)^2], \tag{36}$$

$$\frac{\partial u}{\partial t}(i\Delta x, j\Delta y, k\Delta z, n\Delta t) = \frac{u^{n+1/2}_{i,j,k} - u^{n-1/2}_{i,j,k}}{\Delta t} + \mathcal{O}[(\Delta t)^2]. \tag{37}$$

Replacing the partial derivatives in Maxwell's curl's equations (Eqs. 1 and 2) with the central-differences as shown in the above notation allows us to simply write these equations in a form that is easily programmable.

2.2.2 Finite-difference Expressions for Maxwell's Equations in Two Dimensions

For my research I have used the 2D FDTD method. As mentioned in Section 2.1.1, in 2D Maxwell's equations decouple into two independent cases: namely TE (E_z) and TM (H_z). As in Section 2.1.1, I will restrict myself to the TM case, since I have only used this in my research. Also I will restrict myself to the lossless ($\sigma = 0$) and the non-magnetic case ($\mu = \mu_o$). For an excellent treatment of FDTD for all possible cases, the readers are advised to refer to Ref. [19]. For an arbitrary time variation, Maxwell's equations for the TM case are given as:

$$\frac{\partial}{\partial t}E_x = \frac{1}{\epsilon}\frac{\partial}{\partial y}H_z,$$
$$\frac{\partial}{\partial t}E_y = -\frac{1}{\epsilon}\frac{\partial}{\partial y}H_z,$$
$$\frac{\partial}{\partial t}H_z = \frac{1}{\mu_o}\left[\frac{\partial}{\partial y}E_x - \frac{\partial}{\partial x}E_y\right], \tag{38}$$

where $\epsilon = \epsilon_o\epsilon_r$. Using the central-difference forms as mentioned in (36) and (37), and with $\Delta x = \Delta y = \Delta$ we get the finite-difference expressions for the TM modes in two dimensions.

$$\frac{E_x|^{n+1/2}_{i,j+1/2} - E_x|^{n-1/2}_{i,j+1/2}}{\Delta t} = \frac{1}{\epsilon_{i,j+1/2}}\left(\frac{H_z|^n_{i,j+1} - H_z|^n_{i,j-1}}{\Delta}\right) \tag{39}$$

$$\frac{E_y|^{n+1/2}_{i-1/2,j+1} - E_y|^{n-1/2}_{i-1/2,j+1}}{\Delta t} = -\frac{1}{\epsilon_{i,j+1/2}}\left(\frac{H_z|^n_{i,j+1} - H_z|^n_{i-1,j+1}}{\Delta}\right) \tag{40}$$

$$\frac{H_z|^{n+1}_{i,j+1} - H_z|^n_{i,j+1}}{\Delta t} = \frac{1}{\mu_o}\left(\frac{E_x|^{n+1/2}_{i,j+3/2} - E_x|^{n+1/2}_{i,j+1/2}}{\Delta} - \frac{E_y|^{n+1/2}_{i+1/2,j+1} - E_y|^{n+1/2}_{i-1/2,j+1}}{\Delta}\right). \tag{41}$$

Assuming that H_z is known for all spatial points at time $t = n\Delta t$ and that E_x and E_y are known for all spatial points at time $t = (n - 1/2)\Delta t$, we can find the field values for the next time step: $t = (n + 1/2)\Delta t$ for E_x and E_y, and $t = (n + 1)\Delta t$ for H_z, from the above equations.

$$E_x|^{n+1/2}_{i,j+1/2} = E_x|^{n-1/2}_{i,j+1/2} + \frac{\Delta t}{\epsilon_{i,j+1/2}\Delta}\left(H_z|^n_{i,j+1} - H_z|^n_{i,j-1}\right) \tag{42}$$

$$E_y|^{n+1/2}_{i-1/2,j+1} = E_y|^{n-1/2}_{i-1/2,j+1} - \frac{\Delta t}{\epsilon_{i,j+1/2}\Delta}\left(H_z|^n_{i,j+1} - H_z|^n_{i-1,j+1}\right) \tag{43}$$

$$H_z|^{n+1}_{i,j+1} = H_z|^n_{i,j+1} + \frac{\Delta t}{\mu_o\Delta}\left(E_x|^{n+1/2}_{i,j+3/2} - E_x|^{n+1/2}_{i,j+1/2} - E_y|^{n+1/2}_{i+1/2,j+1} + E_y|^{n+1/2}_{i-1/2,j+1}\right). \tag{44}$$

Hence by simply programming the above equations it is relatively straight forward to have a working FDTD code. A particularly useful enhancement to Yee's algorithm is the use of hexagonal grid rather than the rectangular grid for the two dimensional case. It has been shown [60, 19] that with hexagonal grids the phase velocity anisotropy errors are 1/1,200 times the errors in the Yee algorithm. The numerical phase velocity anisotropy is the different phase velocity in different directions in an empty grid. With Yee's rectangular grid, we require 29 grid points per free-space wavelength to have this phase velocity anisotropy to be less than 0.1%. An important point to keep in mind while choosing the values for Δt and Δ is that for the 2D case $S \equiv \frac{c\Delta t}{\Delta} < \frac{1}{\sqrt{2}}$ to get stable results. This condition on S is known as the Courant stability condition.

Above, I have mentioned the finite-difference implementation of Maxwell's equations in a source free region. In an actual FDTD simulation we need to excite our structure with a source. The easiest way is to use a hard point source. A hard point source can be set up by simply adding a time function to specific **E** or **H** component at a specific grid point in the FDTD grid in addition to calculating the above update equations. Most popular type of these hard point sources are either a sinusoidal source or a Gaussian finite bandwidth pulse. In our 2D TM case we can, for example, assign a time function to H_z field. A Gaussian finite bandwidth pulse excitation at a grid point $((i_s, j_s))$ is given by:

$$H_z|^n_{i_s,j_s} = H_o \exp^{-[(n-n_o)/n_{decay}]} \sin[2\pi f_o(n-n_o)\Delta t]. \tag{45}$$

For my FDTD simulations, other than the ones for generating the dispersion diagram, I have used a connection of a Si slab waveguide connected to a PCW. For these simulations, I excite my structure using a pulsed Huygens waveguide source to launch the fundamental mode of a Si slab waveguide propagating only in one direction. Since I have mostly used the FDTD code written by Dr. Charles M. Reinke, readers can either refer to his dissertation [61] or the original paper [62] for

details on implementing the Huygens source[3].

2.2.3 Absorbing Boundary Conditions

Absorbing boundary conditions (ABCs) are needed around the outer lattice boundary to simulate the infinite extent of the simulation domain. The ABCs should ideally absorb the incident energy with no reflection. The most famous of these ABCs are either the Berenger's PML [10] or the perfectly matched uniaxial medium (uniaxial PML) [63]. In the FDTD code that I developed and also the code developed by Dr. Charles M. Reinke, which I mostly used (due to the parallel computation option), the uniaxial PML has been used as the absorbing boundary condition. Exact mathematical details on implementing the uniaxial PML can be found in [19]. This uniaxial PML, however, does not work well in absorbing dispersive waves in a PCW. As part of my research I have developed my own PML, which I call the adiabatically matched PML (AM-PCPML). Details on the AM-PCPML can be found in Chapter 7.

[3]E-mail the author at murtazaaskari@gmail.com to get working 2D-FDTD codes including the source and PML.

CHAPTER III

FABRICATION OF TWO DIMENSIONAL PHOTONIC CRYSTAL BASED STRUCTURES

One of the major reasons of interest in pursuing research in two dimensional (2D) photonic crystal based devices, rather than three dimensional based PCs, is the ease of fabrication. Two dimensional PCs can be fabricated using mature semiconductor fabrication techniques. By using semiconductor devices based on 2D PCs can be mass manufactured resulting in reduced price per device.

One of the first goals of this research was to come up with an efficient fabrication process for 2D PCs. One benefit of coming up with this fabrication process was that this fabrication process is not PC specific, and can be used to fabricate other integrated optical devices such as those based on microrings, microdisk, and ridge waveguides.

All the fabrication in this research was performed at the Nanotechnology Research Center (NRC) of the Georgia Institute of Technology.

3.1 Wafer specifications and Preparation

We use silicon on insulator (SOI) wafers provided by SOItec (`http://www.soitec.com`). We use two different SOI wafers from the company, see Table 1. One has 220 nm of Si device thickness on 2 μm buried oxide (BOX) on a Si handle wafer. The other has 340 nm Si device layer on top of a 1 μm BOX layer. When we use SOI wafer with 340 nm Si device thickness, we reduce the thickness to somewhere between 220 - 250 nm by oxidizing the top Si and subsequent removal of

oxide layer with buffered oxide etch (BOE) solution. Care needs to be taken during oxidation as 44% of the final oxide thickness is consumed from Si [64]. If a thin oxide layer in needed on top of the Si device layer, I perform the oxidation in two steps. The first step is a wet oxidation step. The oxide is removed after this step. The second is a dry oxidation step and is used to grow the thin oxide. The time required to form a given thickness of oxide on Si can be obtained for a given growth temperature and type of oxidation (dry or wet) at the website: `http://www.lelandstanfordjunior.com/thermaloxide.html`.

Table 1: Specifications of the SOI wafers used for fabricating PCW structures in my research

	Diameter (mm)	**Wafer thickness (μm)**	**Crystal orientation**	**Si device thickness (nm)**	**SiO2 BOX thickness (nm)**	**Device resistivity (Ω-cm)**
Wafer I	100 mm	500	$< 100 >$	340 ± 44	1000 ± 20	15-20
Wafer II	100 mm	500	$< 100 >$	220 ± 30	2000 ± 70	14-20

3.2 Fabrication Steps

This chapter outlines the details of steps required to fabricated a working PCW based integrated optics structure. Figure 4 shows the steps involved in the fabrication.

The fabrication process can be roughly broken down into following steps.

i) CAD file preparation.

ii) Lithography and pattern definition.

iii) Etching.

iv) Undercutting.

v) Imaging.

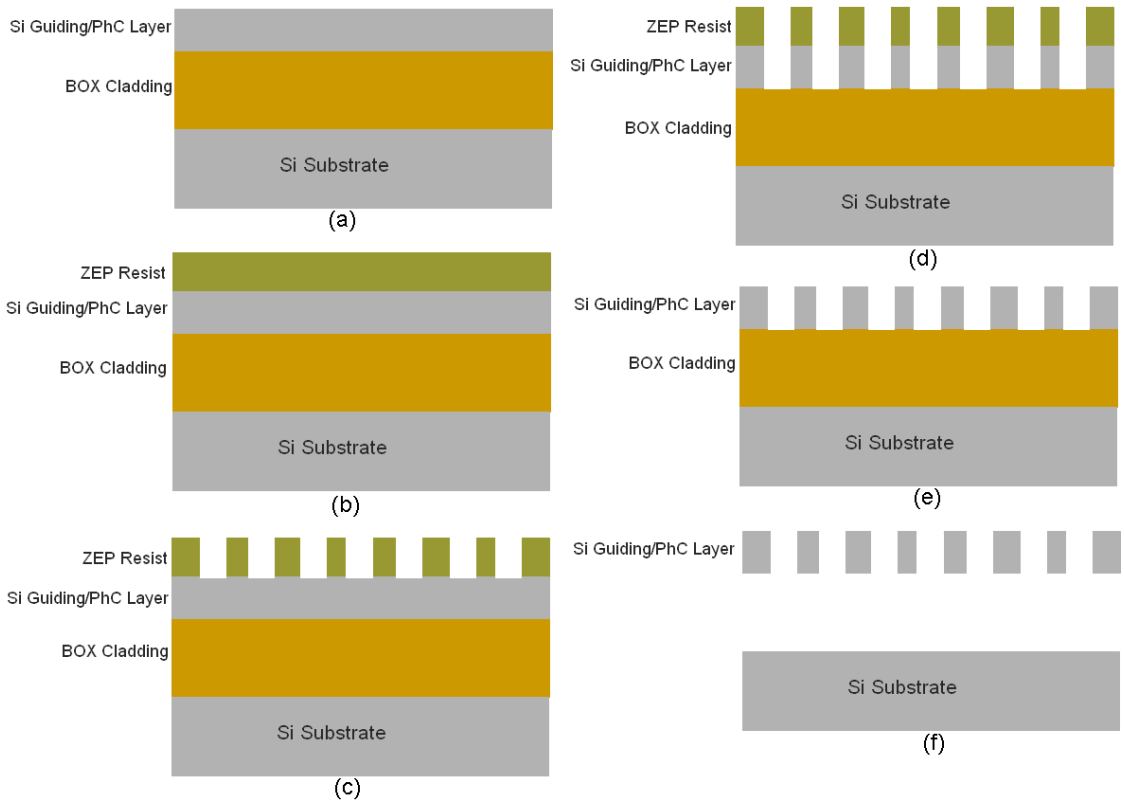

Figure 4: Fabrication process for a PCW-based structure. (a) Start off with an SOI wafer. (b) Spin on ZEP e-beam resist. (c) Pattern ZEP. (d) Etch into the guiding layer. (e) Remove the remaining ZEP after etching. (f) Undercut the BOX layer underneath the PCW region.

3.2.1 CAD File Preparation

The first step in fabricating any device is CAD file preparation. CAD stands for computer aided drawing. Different softwares can be used for this purpose. The most widely used software is AutoCAD provided by Autodesk Inc. This software is available from Georgia Tech and is also installed on various machines in NRC. Another software, which I have used, is dw-2000 provided by Design Workshop Technologies. This software is also provided by Georgia Tech. However Georgia Tech only has one license for this software. An advantage of using dw-2000 over AutoCad is that dw-2000 uses an object-oriented approach, which renders the size

of the files to be much smaller as compared to files generated by AutoCad, specially when you have a lot of repeating patterns in your file. In our case, since we have to write a lot of holes, dw-2000 would result in a much smaller sized file. On one occasion, the file generated by AutoCad was so large that the e-beam lithography system was not able to process it. Another advantage of using dw-2000 is that it allows you to directly export files to gds format. Gds format is used by the e-beam lithography (EBL) system to write patterns. With AutoCad you have to use another software (LinkCad, provided by Bay Technology) to convert it to gds format.

3.2.2 Lithography and Pattern Definition

The second step in fabrication is to use the CAD file to write patterns into a resist layer, see Figure 4 (b) and (c). Photolithography is the most widely used lithography method, which allows wafer scale patterning. The smallest pattern that you can write using photolithography depends on the wavelength of light used to expose the pattern. However since our critical dimensions are small (~100 nm), which are not resolvable by photolithography equipment available at NRC, we have used electron beam lithography (EBL). EBL is a serial lithography approach, where an electron beam is scanned across the sample to write the pattern. EBL is mostly used in a research environment where the cost of pattern writing does not matter much, and where the patterns have to be changed relatively quickly due to design iterations. EBL machine at NRC is a JBX-9300FS manufactured by Jeol ltd. The nanolithography website (`http://nanolithography.gatech.edu`) provides process details for various e-beam resists. Since I have mostly worked with ZEP resist (manufactured by ZEON corporation), this section provides details about the ZEP process. ZEP is a positive tone e-beam resist, and offers higher dry etch resistance and longer shelf life than other e-beam resists. The thickness

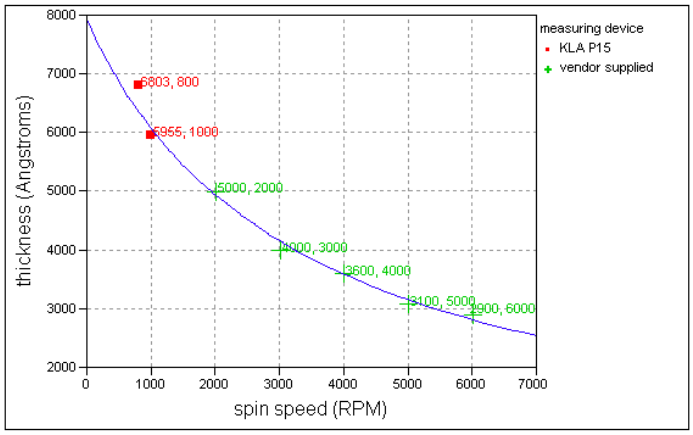

Figure 5: Spin speed curve for ZEP-520A resist on a 4" wafer. The green values are obtained from vendor and the red values are measured at NRC on KLA-15 profilometer [4].

of the resist required is primarily determined by the dry etch selectivity the resist offers over the material you are trying to etch. The etch selectivity is defined as:

$$Selectivity = \frac{Etch\ rate\ of\ material\ to\ etch}{Etch\ rate\ of\ the\ resist\ (mask)} \tag{46}$$

I have used two thicknesses for ZEP resist depending on whether I use a hardmask (thin silicon dioxide layer) or ZEP to etch Si. If I use a hardmask to etch Si, ZEP is only used to etch the hardmask layer. Since the hardmask layer is only ~50 nm thick and the selectivity between SiO_2 and ZEP is around 0.4 for our SiO_2 etch process, I use 430 nm thick ZEP. This thickness is achieved for a spin speed of 4000 rpm. The spin speed curve for ZEP-520A is shown in Figure 5. These resist thickness shown in the figure are for a 4" wafer. Since we use small pieces of SOI wafer, typically 3 cm x 3 cm, the thickness we obtain is around 1.2 times more than the values shown in the figure. When I use ZEP to directly etch into Si, I have to use a thicker resist as we have to etch between 220 - 250 nm of Si. Using a spin speed of around 2000 rpm gives us a thickness of ~600 nm.

After spin coating we have to bake the resist to allow the solvent to evaporate. We bake our samples at 180^oC for 2 min. The CAD file patterns are then written on the resist layer in the EBL machine. I use a dose of ~$250\mu C/cm^2$ for

my PC holes and ~230$\mu C/cm^2$ for my input and output Si ridge waveguides. After e-beam writing, I develop my pattern by immersing the sample in Amyl Acetate for 2 min and rinsing it with Isopropyl alcohol (IPA) after the development. These process conditions can be found at the nanolithography webpage (`http://nanolithography.gatech.edu/zep520a.html`).

Another promising e-beam resist is hydrogen silsesquioxane (HSQ), which is sold by Dow Corning corporation under the brand name of "XR-1541" e-beam resist. HSQ is a negative tone resist and is very similar to SiO_2, as a result the selectivity between HSQ and Si is high, and we can directly etch Si using a pure Cl_2 recipe. The large selectivity also allows getting vertical side walls during the etching. However, HSQ requires a much larger dose (exposure to e-beam), and hence the writing time on an e-beam machine is higher when compared to writing times required for ZEP. The longer writing time translates into higher cost for defining patterns in HSQ as compared to ZEP. Another disadvantage of HSQ is the short shelf life (6 months at 5^oC, see [65]) as compared to a longer shelf life for ZEP [66].

3.2.3 Etching

The next step in fabricating our PC devices is plasma etching, Figure 4 (d). Plasma etching is used to transfer the pattern from the resist layer into the Si device layer of the SOI wafer. I mostly etch my patterns in the STS SOE machine in the NRC. I have used two methods to transfer the pattern from ZEP layer to the Si device layer. In the first method, I use a hardmask layer on top of Si device layer. The ZEP pattern is first transferred to the hardmask layer in a CF_4/H_2 plasma with coil power of 250 W and platen power of 70 W. The process pressure is 3 mtorr. With these conditions, the oxide etch rate is around 60 nm/min. After the oxide etch step the remaining ZEP is stripped using either an 0_2 plasma or piranha solution etch, Figure 4 (e). The piranha solution is used to remove organic coatings

or residues from a wafer. I typically use a 3:1 solution of sulphuric acid (H_2SO_4) and hydrogen peroxide H_2O_2 on a hotplate at a temperature of 120^oC. The pattern is then transferred to the Si layer with a Cl_2 plasma. For this etch step, I sue a coil power of 200 W and platen power of 90 W with a pressure of 3 mtorr. For our Si etch step, the selectivity between Si and Oxide is greater than 10. Due to this huge selectivity for the Si etch step, the side wall angle is very close to 90^o. In the second method, ZEP is directly used to etch the Si layer. For this etch, I use the same process as the Si etch step of the first method. The selectivity between Si and ZEP for our Si etch process is ~0.6. After etching Si, ZEP is removed the same way as in the first step. One drawback of using ZEP to directly etch Si is that the sidewall angle is around 83–84^o. [1]

Care needs to be exercised while performing the dry etch steps, because the condition of the etch chamber greatly affects the etch rates, etch quality (side wall roughness), and selectivity. A good practice is to record the reflected powers for the RF sources (coil and platen), He flow rates, and the color of plasma for each run. These parameters are a good indication of the state of the chamber. If any of these parameters change by more than a few percent, the etch results may be different. Also before performing an actual etch, I always perform an etch rate measurement step with dummy sample to measure the actual etch rate, as the etch rate changes from one run to another.

3.2.4 Undercutting

The term undercutting refers to the removal of oxide layer underneath the PCW region to allow increased bandwidth below the light line. Figure 6 shows the dispersion diagram of a triangular lattice PCW and the BOX (SiO_2) and air light lines. If we remove the BOX underneath the PCW, the bandwidth below the light line

[1] Based on my fabrication results.

would be larger as compared to the case when there is SiO_2 underneath the PCW. Thus undercutting allows larger lossless guiding bandwidth by replacing the BOX cladding with air cladding. The BOX layer underneath the PCW region is removed by using the BOE solution, Figure 4 (f). Photolithography is required to mask off the regions where we do not want to remove the underlying oxide layer such as the input and output ridge waveguides. For photolithography I use the Shipley 1827 positive tone resist. The resist is spun using one of the spin coaters available in NRC at a spin speed of 4000 rpm for 30 seconds. Soft bake is performed for 3 minutes on a hotplate set at 100^oC. The resist is exposed to 405 nm radiation on a Karl Suss MA-6 Mask Aligner. The required dose to fully develop the pattern is $400mJ/cm^2$. Since the intensity of the light source can fluctuate over time, it is a good idea to check the lamp intensity at the exposure wavelength by using the light meter. The patterns are developed in MF-319 developer for 30 sec. The sample is then hard baked at 120^oC on a hotplate for 10 min. The sample is then dipped in a BOE solution for 5-6 minutes. The etch rate of oxide in a BOE solution at room temperature is ~100 nm/min. The photoresist is then stripped in O_2 plasma. It is important not to wet etching to remove the resist, as wet etching breaks the Si access waveguides close to the connection point with the PCWs. During undercutting oxide is removed from parts of Si waveguide close to the PCW, and can break easily when immersed in a fluid due to fluid pressure.

3.2.5 Imaging

Although imaging is not a part of fabrication, but is usually performed after the fabrication to make sure the fabrication quality is acceptable. I have used Zeiss Ultra 60 Scanning Electron Microscope (SEM) manufactured by Oxford Instruments to take SEM images of the fabricated devices. Zeiss SEM is a very high resolution SEM with a field emission source. With an in-lens detector it is relatively easy to

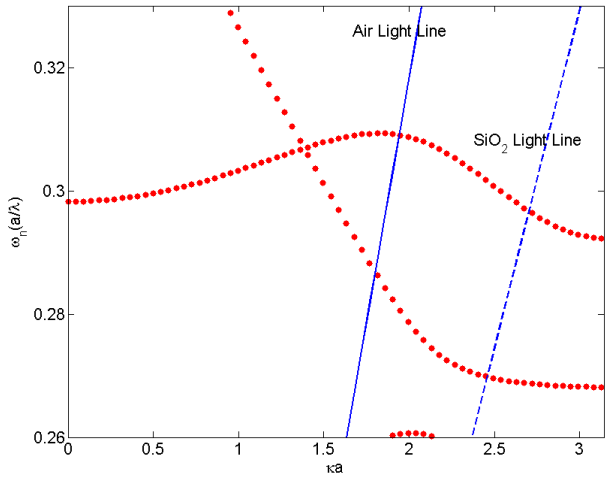

Figure 6: Dispersion diagram of a triangular lattice PCW with SiO_2 and air light lines. The bandwidth of even mode below the air light line is larger, and hence allows larger lossless bandwidth when we undercut our PCW region.

obtain clear images without coating my sample with a conductor down to 30 nm resolution. Figure 7 shows the SEM images of a couple of devices fabricated with this fabrication recipe. These SEM images show the devices fabricated by other people in our group using this recipe. SEM images of structures fabricated as part of my research are shown in other chapters.

More details on physics, chemistry and material science aspects of any of these steps can be found in Ref. [64].

3.3 Microfluidic Channel Fabrication

Microfluidic channels were required in refractive index sensing part of my research. Microfluidic channels are used to transport liquids and gases to the interaction region. SU-8 is a negative tone photoresist manufactured by MicroChem Corporation. It is available in many viscosities and is widely used in the fabrication of microfluidic channels. Reasons for using SU-8 as a microfluidic channel include its chemical inertness and mechanical strength after processing, and the

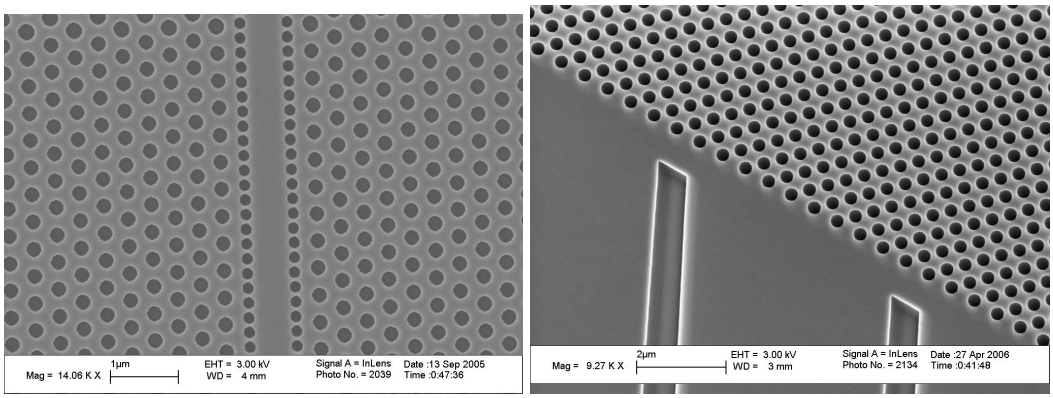

(a) (b)

Figure 7: SEM images of devices fabricated with the fabrication recipe. (a) A Bi-periodic PCW to improve the guiding bandwidth below the light line, and (b) Ridge waveguides terminating at a tilted PC interface.

ability to get very high aspect ratio structures. I have used SU-8 2 for fabricating microfluidic channels for my refractive index sensors. The processing conditions for SU-8 with different viscosities can be found at MicroChem's website (`http://www.microchem.com/products/su_eight.htm`). The process that I have used in my research is outlined below. First the SOI piece needs to be dehydrated. Dehydration is carried out by baking the sample at 200^oC on a hotplate for five minutes. If the sample is not properly dehydrated SU-8 does not stick well to the sample and can peel off after the processing. After dehydration bake, SU-8 2 is spun at 3000 rpm using a spin coater. This spin speed of 3000 rpm usually results in around 1.8 μm thick SU-8 for sample size of around 3 cm x 3 cm. Again the achieved thickness is around 1.2 times what is obtained for a 4 wafer. I then pre-bake the sample at 65^oC for a minute and then soft bake it at 95^oC for 3 minutes. A two-step soft bake process allows controlled evaporation of solvent, resulting in reduced edge bead and better resist to substrate adhesion. The resist is then exposed to 365 nm radiation using a Karl Suss MA-6 Mask Aligner. I use a dose of ~100 - 120 mJ/cm^2. Following exposure, post exposure bake (PEB) is performed

in two steps. A one minute bake at 65^oC followed by a minute bake at 95^oC on a hotplate. The pattern is then developed in SU-8 developer for around 1 minute. The sample is then rinsed in IPA. A white film formation during IPA rinse is an indication of an under developed film. In this case you can put the sample in the developer for some more time and repeat the rinse step.

In an actual product, SU-8 microfluidic channels need to be capped with a PDMS film and an inlet and an outlet needs to be provided for bring different solutions to the sensor area. However, in my case I have not capped the microfluidic channels for ease of cleaning and testing with different refractive index fluids.

CHAPTER IV

MODELING OF PCWS AS DISPERSIVE HOMOGENEOUS MEDIA

The unique feature of a PCW, which distinguishes it from waveguides with uniform cross-section is its dispersion. Figure 8(a) compares the dispersion (ω vs. κ) of the fundamental modes of a PCW and a silicon ridge waveguide. The ridge waveguide mode has a linear dispersion, which is evident from the linear fit also shown in the figure. The dispersion diagram of a PCW, on the other hand, has two distinct regions.

i) Linear region.

ii) Non-linear region.

In the linear region the dispersion of a PCW is very similar to a ridge waveguide, and can be modeled with a straight line with a nearly constant slope given by $v_g = \frac{\partial \omega}{\partial \kappa}$, where v_g is the group velocity. In the non-linear region the group velocity is no longer linear and becomes a function of frequency ($v_g(\omega)$), see Figure 8(b). The group velocity gets smaller and smaller as we approach the edge of the Brillouin zone ($\kappa a = \pi$). The dispersion in this region is huge, which simply means that the group velocity is highly non-linear. Huge dispersion in the non-linear region implies that the shape of a pulse with a considerable bandwidth and center frequency in this non-linear region will get distorted as it propagates in the PCW. This will happen because different frequency components in the pulse will travel at different velocities resulting in considerable change in pulse shape as it propagates inside the PCW. The existence of slow light and huge dispersion in the PCW

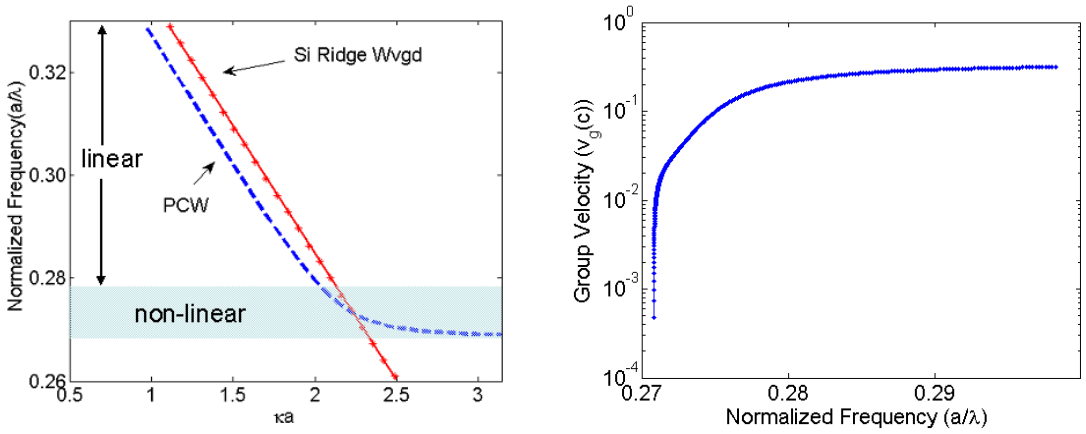

(a) (b)

Figure 8: (a) Comparison of dispersion diagrams of a PCW (blue dashed curve) and a ridge waveguide (red asterisks). Also shown is a linear fit to the ridge waveguide dispersion. The nonlinear part of PCW dispersion is shown as a shaded region. (b) Group velocity v_g as a function of frequency (ω) for a PCW.

has fueled almost all the research in PCWs.

The FDTD method is used to study the effect of dispersion on a finite bandwidth pulse propagating through the PCW. For example, FDTD is used to study how much would a pulse be delayed while propagating through a finite length of a PCW, or what would be the pulse spread or pulse shape at the output. An issue in simulating pulse propagation at small group velocities in PCWs is that these simulations take a lot of time.

A sample application of a PCW is an integrated optical delay line. The figure of merit (FOM) for this application is the delay-bandwidth product ($n_g \frac{\Delta\omega}{\omega}$). In these PCWs, it is easily possible to obtain group indices (n_g) around 50 [54, 53]. A group index as high as 200 [67] has been demonstrated experimentally. However, the dispersion can render operations at such large indices impractical. For designing a delay line it is important to find what delays are possible given a certain bandwidth of an incoming signal, so that the pulse does not get distorted beyond a certain limit. Going to smaller and smaller group velocities entails longer and longer

simulation times as it takes an optical pulse longer time to propagate through the structure. However, to avoid excessive pulse distortion at large group indices, we need to reduce the frequency bandwidth of the input pulse. Since pulse width in the time domain and pulse width in the frequency domain are inversely proportional, a smaller pulse in the frequency domain implies a larger pulse in the time domain, this fact also results in longer simulation times. Another factor that results in large simulation times is the long length of PCWs required to obtain steady state response when operating at low group velocities. More detail on this are in Section 4.1.3. All these factors: (i) smaller group velocity of pulses, (ii) large temporal width of the pulses and (iii) large simulation structures, result in very large simulation times. For example, it takes 2^{21} time steps for a pulse with a group index of 15 ($n_g = 15$) and a bandwidth equal to one channel of dense wavelength division multiplexing (DWDM) through 102 layers of a PCW. On a single Pentium 4 processor such a simulation can take up to 15 days. Although computer clusters with many processors can be employed to reduce simulation times, it may still take days for a design that requires running simulations at different central frequencies and with different bandwidths.

A goal of this research was to come up with an analytical modeling tool for characterizing pulse propagation through these PCWs. The goal was to cut the simulation time to seconds without compromising the accuracy. In this chapter, I will present various approaches for modeling pulse propagation in PCWs. I will compare our approach to some other alternative approaches. First let me briefly discuss some challenges associated with simulating pulse propagation in PCWs.

4.1 Challenges in Simulating Pulse Propagation in PCWs

I came across numerous challenges when I tried to model the dispersion diagram of a PCW. Before we can ascertain the validity of our model, we either need to

overcome these challenges or need to somehow take these issues into account in our model so that we can get a good match with the FDTD pulse propagating results. Some of these challenges are mentioned below.

4.1.1 Approaches to Obtaining Dispersion Diagram

As mentioned in Chapter 2 both FDTD and PWE methods can be used to obtain dispersion diagram of a PCW. However, due to the different approaches used in the two methods, the resulting dispersion for the same structure can be quantitatively different to the extent that the modeling of the dispersions obtained from these methods would give different results. In this section we discuss the inherent differences arising in the dispersion due to the implementation details of the two methods.

In the PWE method, we solve Maxwell's equations as an eigen-value problem. In the most commonly used version of this method, we provide the wave-vector (κ) in the first Brillouin zone ($0 \leq \kappa a \leq \pi$) and obtain the frequencies (ω) from the eigen-values for the given κ. For mathematical formulation and some implementation details of the PWE method see Chapter 2. For obtaining the dispersion diagram of a PCW, we specify the super-cell, and there are two variables that can be changed to obtain the dispersion diagram: i) the number of unit cells of a PC along the y-axis and ii) the number of plane-waves used to solve the eigen-value problem. In Chapter 2 we simply mentioned the summation on reciprocal lattice vectors ($\mathbf{G}$), see for example Eqs. 10 and 14. What we did not elaborate is how many reciprocal lattice vectors are to be considered in those summations. To exactly represent the structure in reciprocal space we need the summation to run on an infinite number of reciprocal lattice vectors. However, due to memory limitations of computation systems we have to limit the number of plane waves. Increasing the number of plane waves increases the size of the matrix to be inverted and

hence causes an increase in the computation time as well as the memory requirements. Any change in the number of plane waves used in computation affects the resulting dispersion. Figure 9(a) shows a sample super-cell that is one unit-cell long along x-axis and 5 unit-cells high along y-axis. Figure 9(b) shows the dispersion for three different values of the variables: number of periods along y (Prd) and the number of plane waves (PW) used to calculated the dispersion diagram. The figure shows that as we increase the number of plane waves the dispersion diagram moves down in frequency (see Prd = 5, PW = 9; and Prd = 5, PW = 11 dispersion curves). It may seem at first sight that the band edge moves by only 0.6%, but more importantly the group index and dispersion at a fixed frequency changes much more drastically. For example, at the center frequency of $\omega = 0.27373$ the dispersion curve with PW = 9 predicts a group index of around 224 and the dispersion with PW = 11 predicts the group index of only 19.5. Thus even though the dispersion shifts by a very small percentage the corresponding change in the group index and dispersion is huge. Hence, it is very important to use the correct dispersion when comparing the results of analytical modeling with those of FDTD pulse propagation simulations. Figure 9(b) also shows that as we increase the number of periods along y-axis the dispersion diagram moves up (see dispersion curves for Prd = 5, PW = 9; and Prd = 7, PW = 9). Again, using different curves will result in different values of group delay and the pulse spread; hence it is very important to find the curve that corresponds to the actual pulse propagation results. Another parameter that can be varied is the number of grid points per unit cell along x-axis. Varying this parameter also moves the dispersion diagram up or down in frequency. Since in our pulse propagation simulations (using FDTD) we have specified 24 grid points to equal one period along x-axis, we have used the same 24 grid points as one unit cell along x-axis for calculating the dispersion diagram of the PCW using the PWE method.

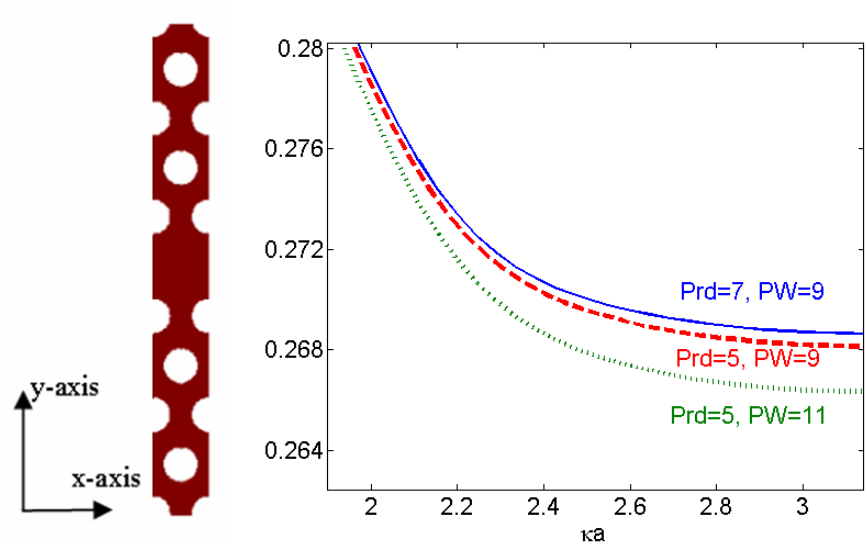

(a) (b)

Figure 9: (a) Super-cell, with one unit-cell along x-axis and 5 unit-cells along y-axis, used in calculating the dispersion diagram. (b) Dispersion diagram of the TM modes (i.e. magnetic field normal to the plane of periodicity) of the PCW for three different values of the variables, number of periods along y (Prd), and number of plane-waves (PW). Blue solid curve is for Prd = 7 and PW = 9, red dashed curve is for Prd = 5 and PW = 9, and green dotted curve is for Prd = 5 and PW = 11.

In the FDTD method we use a super-cell – similar to the one shown in Figure 9(a) – to calculate the dispersion diagram. We employ the periodic boundary condition along x-axis, to simulate the infinite extent of the PCW along x-axis, and perfectly matched layer (PML) at the boundaries of the simulation structure along the y-axis. We specify an arbitrary initial field in the middle slab region and the propagation vector (κ). The fields are propagated through the structure with the specified κ for long enough time that the remaining field is a combination of only the modes of the PCW for the specified κ. The field values are recorded as a function of time at a point that is not a symmetry point of the simulation structure; e.g, if we were to record the fields at the center of the slab along the y-axis, H_z will only have a contribution from the even mode as H_z has a null for the odd mode along the center of the unit cell in the y-direction. A Fast Fourier transform (FFT)

of the recorded time fields is taken to get the fields in the frequency domain. The FFT data is filtered and the peaks in the frequency domain are obtained. These peaks in frequency domain correspond to the frequencies of the modes supported by the simulation structure for the specified propagation vector (κ). Note that the frequencies that are sampled when we take the FFT depends on the sampling frequency in the time domain and the total number of time steps for which the field has been recorded. The actual frequency for a mode of the structure may not fall at one of the sampled frequency points and thus the dispersion diagram obtained using the FDTD method is discretized. This discretization is evident in Figure 10, where we are comparing the dispersions for two cases; i) when we use 24 grid points to represent the period along x-axis ($a_x = 24$) and the total simulation time of 2^{16} time steps (i.e., Time = 2^{16} shown with red circles in the figure), and ii) when $a_x = 35$ and $Time = 2^{20}$ time steps (shown with green plus signs). The dispersion with shorter simulation time (red circles) shows discrete steps in the frequency domain. With longer simulation times this discretization is less evident and the dispersion diagram becomes smoother. The main point here is that no matter how many simulation time steps we use, our frequency domain is sampled and we can only get our filtered frequency to be as close to the actual (eigen) frequency as the frequency spacing between samples. The two dispersions, in the figure, also show that the dispersion moves to lower frequencies as we increase the number of grid points per unit cell of the PC.

For the FDTD method, we saw that the dispersion diagram is discretized along the ω_n axis. This discretization would result in anomalous dispersion if we use the FDTD obtained dispersion diagram for our analytical modeling. Hence, I decided to use the PWE obtained dispersion. I fixed the number of grid points along x-axis to be 24, the same as our grid size in the FDTD pulse propagation simulations. However, now the question is how do I specify the variables for the PWE method

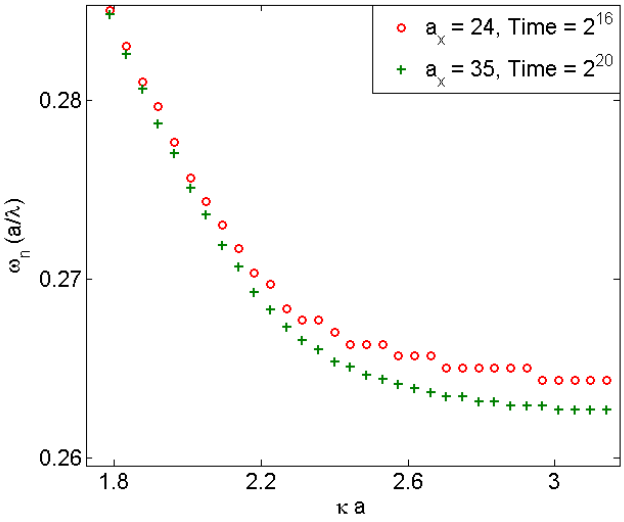

Figure 10: FDTD obtained dispersion for two different combinations of number of grid points per period along x-axis (a_x) and total time of the simulation (Time): a_x = 24 grid points and Time = 2^{16} (red circles), and a_x = 35 grid points and Time = 2^{20} (green plus signs).

(i.e., how many periods along y-axis do I use in my super-cell, and similarly how many plane waves do I use in my estimation of the periodic structure)? The answer to this question is complicated by the fact that the dispersion diagram does not simple move up or down when we change the number of plane waves used to approximate the structure in spatial frequency domain, but even the shape of the dispersion also changes (e.g., for a given delay two dispersions with different number of plane waves will have different second order dispersion). Figure 9(b) shows that as we increase the number of plane waves from 9 to 11 for Prd = 5 (red dashed curve and green dotted curve) the dispersion not only moves down but becomes less flat in the non-linear region. This observation can intuitively be explained by noting that we need an infinite number of plane waves in the spatial frequency domain to exactly replicate the structure in the spatial domain. That is, the abrupt interfaces between the air and dielectric regions require an infinite number of plane waves. However we can not use an infinite number of plane

waves due to computational limitations, so we limit the number of plane waves to approximate the actual structure. Thus, different number of plane waves will approximate the structure differently and would result in different dispersions. Our choice of the dispersion is hence determined by the dispersion's ability to closely approximate the pulse propagation results of the FDTD. I will return to this point again when I talk about the comparison of our modeling results (using different dispersions) with the FDTD obtained pulse propagation results.

4.1.2 How to Characterize the Pulse

The first question that comes to mind, when you sit down to model pulse propagation in a PCW, is what is the best way to characterize a pulse. Should one work in frequency domain and use the amplitude and phase of the pulse to characterize it, or should one work in the time domain and use some sort of Gaussian pulse characteristics to describe the pulse? The answer to this question is that you can use any method as long as you are consistent in using it.

For example, the amplitude and phase of the pulses in the frequency domain can be used to characterize the pulses. From the phase of the pulse we can compute the delay ($\frac{d\phi}{d\omega}$) and different orders of dispersions ($\frac{d^n\phi}{d\omega^n}$) by differentiating the spectral phase ($\phi(\omega)$) with respect to frequency (ω). We also need metrics to characterize the pulse. By metrics I mean how much second, third, order dispersion is tolerable or how much combined (second, third, etc.) dispersion is tolerable. Similarly, how much distortion in the pulse amplitude, if any, is tolerable. Since there are no universally accepted metrics to characterize a pulse using the frequency domain, we decided not to use the frequency domain to characterize the pulse.

If we work in the time domain we can characterize a pulse in two ways. First, by defining a theoretical Gaussian pulse, which is same as the input pulse, and using shifted versions on this theoretical Gaussian pulse to find the delay. Similarly,

the pulse spread can be characterized by comparing the pulse width of the theoretical Gaussian pulse to the output pulse from the FDTD simulation. However the difficulty lies in how to characterize the distortion in pulse shape. The other way is to use standard Gaussian pulse characteristics (i.e mean, standard deviation, skewness, and kurtosis) [68] with the time domain pulses to obtain the group delay (group velocity), pulse spread, and pulse shape distortions. For example, the mean of the pulse at different surfaces can be used to find the group delay or group velocity, the pulse spread can be obtained using standard deviation. The good point about using this approach is that we can also characterize the asymmetry of the pulse by using the skewness parameter. I have used these standard Gaussian pulse measures to characterize the input and output pulses of my pulse propagation simulations. In mathematical terms the mean, standard deviation and skewness are given by:

- Pulse Energy: $Q_T = \int_{-\infty}^{\infty} P_x(t)dt = \sum_{-\inf}^{\inf} P_x(n)\Delta t$,
- Mean: $\mu = \dfrac{\int_{-\infty}^{\infty} tP_x(t)dt}{Q_T} = \dfrac{\sum_{-\inf}^{\inf} nP_x(n)\Delta t}{Q_T}$,
- Standard deviation: $\sigma = \sqrt{\dfrac{\int_{-\infty}^{\infty}(t-\mu)^2 P_x(t)dt}{Q_T}} = \sqrt{\dfrac{\sum_{-\inf}^{\inf}(n-\mu)^2 P_x(n)\Delta t}{Q_T}}$,
- Skewness: $\gamma = \dfrac{\int_{-\infty}^{\infty}(t-\mu)^3 P_x(t)dt}{Q_T\sigma^3} = \sqrt{\dfrac{\sum_{-\inf}^{\inf}(n-\mu)^3 P_x(n)\Delta t}{Q_T\sigma^3}}$,

where $P_x(t)$ is the time domain Poynting vector along the propagation direction (x-axis in our simulations). The first equality is the definition of each term and the second equality provides the formula implemented in our code to compute these values.

4.1.3 Effect of center frequency on Pulse Settling Times and the Need to Simulate long PCWs

As alluded to in the beginning of this chapter, one of the factors that result in large simulation times is the long length of PCWs required to obtain steady-state delay response of the structure when operating at low group velocities. This is due to the fact that mathematical expressions for the modes of a PCW are not available, and we have to excite the PCW through other means. We can either use a point source inside the PCW to excite it, or we can use a connection of a slab waveguide and a PCW, see Figure 11, and excite the slab waveguide with its mode. A waveguide Huygens source [62] allows us to launch only a forward propagating pulse, and hence there would not be any reflections from the PML on the left edge of the simulation domain. A point source launches energy in both forward and backward directions. As a result, the reflections from the PML at the left edge of the simulation domain also appear at the observation surfaces and compromise the validity of the observed pulse. Also, the spatial profile of the slab waveguide mode is closer to the spatial profile of the PCW mode than the radiation pattern of the point source, and hence will evolve into the PCW mode a lot quicker than the case if we were to use the point source. Hence, I decided to use a connection of a slab waveguide to a PCW, as shown in Figure 11, for our pulse propagation experiments.

A Huygens waveguide source [62] is used to launch a forward propagating pulse in the slab waveguide. This pulse has the spatial profile of the fundamental mode of the slab waveguide. The pulse enters the PCW with the spatial profile of a slab waveguide mode. As the pulse propagates through the PCW, its spatial profile evolves from a slab waveguide mode to that of a PCW mode. From our simulation results, the distance it takes for the pulse to evolve into the PCW

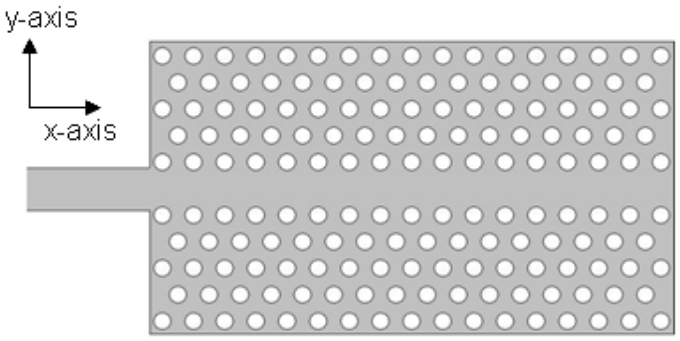

Figure 11: The structure used for simulating pulse propagation using FDTD method. The structure consists of a slab waveguide connected to a PCW. A Huygens waveguide source is used to launch a forward propagating pulse in the slab waveguide.

mode depends on the group velocity of the mode; the smaller the group velocity the larger it takes for the slab waveguide mode to evolve into the PCW mode. Hence, longer structures are needed to get accurate results when operating at small group velocities. Figure 12 (a) shows the variation in group index (n_g) as measured between consecutive observation surfaces for a 22 layer PCW for three center frequencies: $\omega_o = 0.2712$, $d\omega = 5e^{-5}$ (blue solid curve), $\omega_o = 0.275$, $d\omega = 5e^{-5}$ (red dashed curve), and $\omega_o = 0.3132$, $d\omega = 1.88e^{-4}$ (green dotted curve). The location of observation surfaces is the same in each case; the first observation surface was placed at $1a$ (one period into the PCW from the slab-PCW interface) and the distance between each subsequent observation surface was $5a$. The average group delay as measured for the three cases was: $n_g = 3.206$ for $\omega_o = 0.3132$, 5.1383 for $\omega_o = 0.275$, and 7.8826 for $\omega_o = 0.2712$. The figure shows that the variation in n_g is minimal (around 2%) when operating in the linear part of the dispersion diagram (i.e., $\omega_o = 0.3132$, see Figure 8(a)). However, there is considerable variation in n_g when operating in the non-linear part of the dispersion diagram ($\omega_o = 0.2712$ and 0.275), even though the frequency bandwidth is less than half of the case when we are operating in the linear part of the dispersion ($\omega_o = 0.3132$).

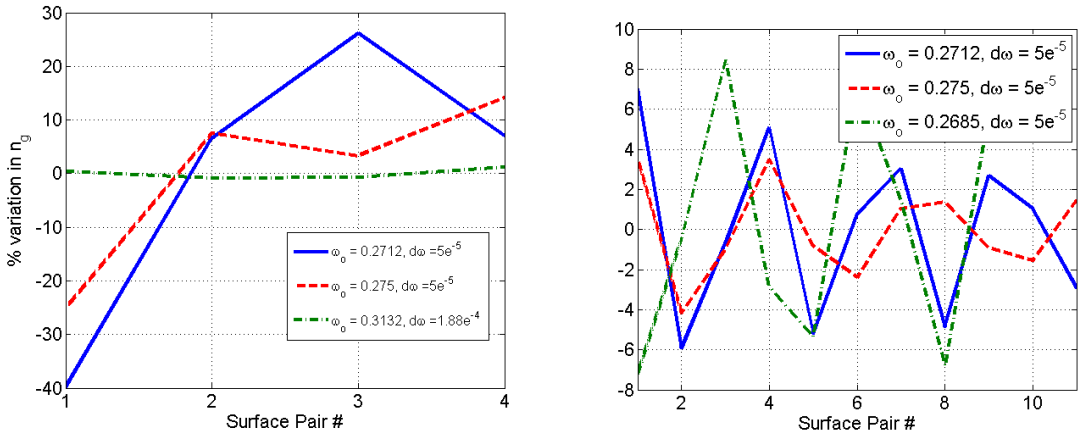

(a) (b)

Figure 12: Percentage variation in n_g between equally spaced observation surfaces for a 22 layer PCW (a) and a 102 layer PCW (b). For the 22 layer PCW (a) the delay variation is plotted for three cases: $\omega_o = 0.2712$, $d\omega = 5e^{-5}$ (blue solid curve), $\omega_o = 0.275$, $d\omega = 5e^{-5}$ (red dashed curve), and $\omega_o = 0.3132$, $d\omega = 1.88e^{-4}$ (green dotted curve). For the 102 layer PCW (b) the delay variation is plotted for: $\omega_o = 0.2712$, $d\omega = 5e^{-5}$ (blue solid curve), $\omega_o = 0.275$, $d\omega = 5e^{-5}$ (red dashed curve), and $\omega_o = 0.2685$, $d\omega = 5e^{-5}$ (green dotted curve).

The figure shows that for the same bandwidth of the pulse ($d\omega = 5e^{-5}$) the percentage variation in n_g for $\omega_o = 0.2712$ is larger (65%) than for $\omega_o = 0.275$ (40%). That is, the variation in n_g between consecutive surfaces is larger when we operate at lower group velocities. The figure shows that if we ignore the delay between the first two surfaces (i.e., the first data point) the variation is much smaller in the two cases (around 20% for $\omega_o = 0.2712$ and around 11% for $\omega_o = 0.275$), which indicates that it takes a certain propagation distance into the PCW before the slab mode evolves into the PCW mode.

Figure 12(b) further strengthens the observations mentioned in the last paragraph. The figure shows the variation in n_g for three case, two same as in Figure 12(a) ($\omega_o = 0.2712$ and $\omega_o = 0.275$) and one with $\omega_o = 0.2685$ and $d\omega$ same as the other two. ($d\omega_o = 5e{-}5$). Here the length of the PCW is 102 layers. The variation in delay for the two cases considered in Figure 12(a) is 12.6% for $\omega_o = 0.2712$ and 7.3%

for $\omega_o = 0.275$. Note that these variations are smaller than the 22 layer case. The average delay as measured was 8.0571 for $\omega_o = 0.2712$ and 5.0461 for $\omega_o = 0.275$. Also note that these group indexes are different than the ones for the 22 layer case by around 2% in each case. That is there is considerable variation in the group delay for different lengths of the PCW. We also ran simulations for 72 layer PCW for these two cases and observed that going from 72 layer to 102 layer the group index changes by less than 0.1%. The third case shown in the figure, $\omega_o = 0.2685$ has an even larger group index of 20.1437, and the variation (15.4%) in this case is also larger than the other cases. This again shows that the larger the group index the larger the variation. Based on the above two observations, we can claim that it takes longer structures for the delay to settle down as we approach larger and larger group indexes.

From the above discussion we can make the following observations.

(a) The variation in group delay (n_g) between consecutive surfaces is larger when operating at frequencies with larger group indexes (n_g) for a given length of PCW.

(b) The average group index value as measure for different lengths of PCW also changes as we increase the length of the PCW.

(c) The pulse takes some propagation into the PCW before it evolves into the mode of the PCW.

4.1.4 Effect of Slab to PCW Coupler on the FDTD Obtained Pulse Propagation Results

My work on ridge to PCW couplers indicates that the response of the butt coupler is not uniform for all operating frequencies, see Chapter 6. I also showed in that chapter that by appropriately designing the coupling region the response of the coupler can be improved to be much more uniform across the frequency range of

interest. I also studied the effect of couplers on the pulse propagation simulations and their correlation with the mathematical modeling of the PCW dispersion. Table 2 displays some of the pulse characteristics for different simulation conditions, such as: couplers (taper or butt coupler), length of the PCW, and the bandwidth of the input pulse. The center frequency in each case is the same, $\omega_o = 0.2685$. The first column displays the simulations parameters,i.e., the length of the PCW, the coupler, and the bandwidth of the input pulse used for the simulation. The second column displays the average delay as measured while propagating inside the PCW. The location of observation surfaces in all simulations was the same, with the first observation surface placed 10 periods inside the PCW and subsequent observation surfaces placed at a distance of $8a$, where a is the PCW period. The third column shows the variation in delay as measured between equidistant surfaces. The fourth column shows the percentage increase in pulse σ with respect to the first surface. The fifth column displays the pulse energy, see Q_T in Section 4.1.2, coupled into the PCW. The first two entries are for a taper coupled PCW and the others are for a butt coupled PCW. Comparing the delay values for the taper coupled case with those obtained for the butt coupled case, we see that larger delay values are obtained for the taper coupler case and that the delay values as obtained from butt coupled simulations approach the taper coupler case as the length of PCW is increased or if the bandwidth is decreased. These observations can be explained by considering the coupling response of a butt coupler: the coupling is not uniform in the non-linear region of the dispersion diagram and the efficiency decreases as we approach smaller and smaller group velocities, see Figure 30(a) in Chapter 6. This butt coupler response biases the coupling towards larger group velocities and hence simulations with butt couplers result in smaller delay values. This effect of this bias decreases as we decrease the input bandwidth, and hence the delay approaches the delay values as obtained with taper coupler simulations.

Since the response of taper coupler is much more uniform at low group velocities (see Figure 34 in Chapter 6), we observe larger group delay values for the taper coupler simulations as compared to butt coupler simulations. Column three shows that the variation in delay is larger for the butt coupled PCW as compared to the taper coupled PCW, which shows that our taper couplers help in evolving the slab mode into the PCW mode. The percentage increase in pulse standard deviation (σ) is greater for taper coupled PCW simulation again due to better coupling at low group velocities for the taper coupler. As mentioned above the butt coupler has a bias for larger group velocities, this bias can also be viewed as bias towards less dispersive part of the dispersion, and hence the butt coupler results in lower pulse spread. The last column shows that much larger pulse energy is coupled into PCW for the taper coupler than the butt coupler; again reiterating the fact that taper couplers allow more efficient injection of light at low group velocities.

Table 2: Pulse characteristics for taper coupler and butt coupler for different lengths of PCW and bandwidths. The center frequency is the same for all cases, $\omega_o = 0.2685$.

No.	**PCW length, coupler, bandwidth**	**Delay**	**% variation in delay**	**% increase in σ w.r.t 1^{st} surface**	**Pulse energy**
1.	52a, Taper coupler, 9.4e-5	21.18	3	2.15	7293.85
2.	102a, Taper coupler, 9.4e-5	21.21	3.5	8.93	7305.6
3.	102a, Butt coupler, 9.4e-5	19.41	10	0.86	2649
4.	202a, Butt coupler, 9.4e-5	20.15	10.42	2.84	2642.49
5.	102a, Butt coupler, 5e-5	20.14	15	7.71	1634.55

The above observations show that with a butt coupler the results are biased towards less dispersive and higher group velocity frequency points, and that the use of a taper coupler allows us to remove this bias in the FDTD pulse propagation results. Hence, we have used taper coupler PCWs in our pulse propagation FDTD simulations to confirm the validity of our modeling approach.

4.2 Unique Features of Pulses Propagating in a PCW.

In this section, we discuss some of the interesting and unique features that we observe for pulses propagating inside the PCW.

4.2.1 Negative Local Values for Poynting Vector

The Poynting vector ($\vec{P}$) represents the direction and magnitude of power flow. In the time domain, it is given by $\vec{P} = \vec{E}x\vec{H}$, where $\vec{E}$ and $\vec{H}$ are the time domain electric and magnetic fields. Referring to our simulation structure shown in Figure 11, and considering that we are exciting the TM mode of the slab and PC waveguides, the fields consist of Hz, Ex and Ey components. Since we are only exciting the forward propagating mode, the Poynting vector should have an x-component (P_x) that is positive. One of the unique features of pulse propagating inside the PCW is that although the spatially integrated (along a line observation surface in the y-direction) P_x is always positive, locally it has negative values. This is primarily due to the nature of Bloch mode, which consists of both forward and backward propagating components. This observation is consistent with results reported in Ref. [69], where they show the spatial map of $\vec{P}$ in a PCW. We also observed similar features in our pulse propagation simulations.

4.2.2 Pulse Compression due to Small Group Velocity

Another interesting feature I observed during these simulations is that the pulse gets compressed when it enters into the PCW, and the amount of compression depends on the group velocity of the mode in the PCW. The smaller the group velocity the larger the compression. These observations are similar to the reported results [37]. A result of this compression is that the field intensities scale with the compression ratio. The enhanced intensities at low group velocities can easily be explained by energy conservation principles [37].

4.3 Modeling Approach and Some Implementation Details

After discussing the issues in modeling pulse propagation, lets turn our attention to different modeling approaches. There are multiples ways of approaching the modeling issue. For example, one may take a wide band frequency input pulse, let it propagate in the time domain through a PCW of known length using an FDTD simulation and record the output pulse. Convert the pulses to the frequency domain, and from the amplitude and phase of the input and output pulses extract the amplitude and phase response of the medium through which the pulse has propagated (in our case a PCW). The frequency domain response of the system can then be used to find the output pulse for any given input pulse. This approach can be viewed as finding the impulse response of the system. If the system is linear and time invariant (LTI) this impulse response can be used to find the output for any given input by using the formula.

$$Y(\omega) = H(\omega)X(\omega). \tag{47}$$

Although in optics we need one additional condition of space invariance to be able to apply this method, in our case we do not need to worry about satisfying this condition, as we are assuming that the input location is fixed. Fixed input location in our case means that we are always exciting the input slab waveguide's fundamental mode, and that the connection between the input slab waveguide and the PCW is fixed. However, the problem with this approach for finding the impulse response of the PCW is that the output pulse would also have the signature of the slab to PC waveguide coupling in addition to the propagation response of the PCW. The other issue is that even though we may be able to extract the amplitude response of the PCW, we can not unambiguously extract the phase response due to the 2π periodicity in phase; i.e, we can not tell if the phase is ϕ or $2n\pi + \phi$, where n could be any non-negative integer. So we need another way of unambiguously

finding the frequency response of our structure.

On careful consideration, the dispersion diagram actually does provide us with the frequency response of the PCW. The dispersion diagram provides us with the propagation constant (κ) as a function of frequency (ω) for different modes of the PCW. As long as we are coupling only to a single mode, by multiplying the $\kappa(\omega)$ with the propagation distance (l), we can find the phase accumulated by each frequency component of the pulse. Thus, the dispersion diagram explicitly provides us with the phase response of the PCW, provided we are in the single mode region of the dispersion diagram. The amplitude response, on the other hand, can implicitly be extracted from the dispersion diagram provided certain conditions are met. For 2D simulations there is only one condition: the length of the PCW should be long enough that no energy in the frequency range of the mode gap can propagate through the PCW. In other words, all the energy is the mode gap is simply reflected. With this assumption in mind we can simply put the amplitude response for frequency components in the mode gap region to be zero. For all other frequency components we put the amplitude response as unity, as PCW is inherently lossless in the two dimensional sense. In 3D, however, there is an additional condition that we have to keep in mind. In 3D, the propagation in the PCW is inherently lossless only below the light line. For frequencies above the light line, the light slowly leaks out of the waveguide. Thus, for accurate amplitude response we need to know the expression for the decay of energy for frequency components above the light line. The main point of the above discussion is that for the 2D case, which I have considered in my research, and most 3D cases (since we mostly want to operate below the light line) we also know the amplitude response of the PCW from its dispersion diagram.

For the modeling, I have used Matlab. We start with the input pulse. First I take the Fourier transform using the fft() method. For all sampled frequency points

within the single mode region of the PCW, we extract the propagation constant from the dispersion obtained use the PWE method. Since the sampled frequency points may not lie at the points where we have generated the dispersion, we use interpolation (interp1() method in Matlab with 'pchip' as the interpolation method; pchip is the shape-preserving piecewise cubic interpolation) to find the propagation constant κ at the sampled frequency points. The phase of the output pulse in the frequency domain is then obtained by simply multiplying the sampled propagation constants (κ_{samp}) with the propagation length. The spectral amplitude of the output pulse is obtained by multiplying the spectral amplitude of the input pulse by 1 if the sampled frequency lies in the single mode range of the PCW dispersion, or zero if the sampled frequency lies outside the single mode frequency range.

In Section 4.1.1, we discussed why we chose to use the dispersion diagrams obtained using the PWE method. However, we did not finalize which dispersion to use. In other words, we did not finalize what values for the variables: the number of plane waves and the number of periods along y-axis, to use for the dispersion. This turned out to be the most important question, and it really took me sometime to find the correct dispersion that gives us good agreement with the FDTD pulse propagation simulation results. To cut down one more variable, I fixed the number of periods along y to be the same as in the FDTD pulse propagation simulations. Figure 13(a) shows the dispersion for three different values of number of plane waves used in the PWE method. It is obvious from the figure that the dispersion in the linear (or the high group velocity) region is very similar for the three different values of number of plane waves. We also observe the same (i.e. similar group delays) when we compare the FDTD pulse propagation simulation results at large group velocities to the analytical results based on modeling any of these dispersions. A comparison of FDTD obtained group delays and those predicted by the three dispersions for pulses with center frequencies lying in the high group

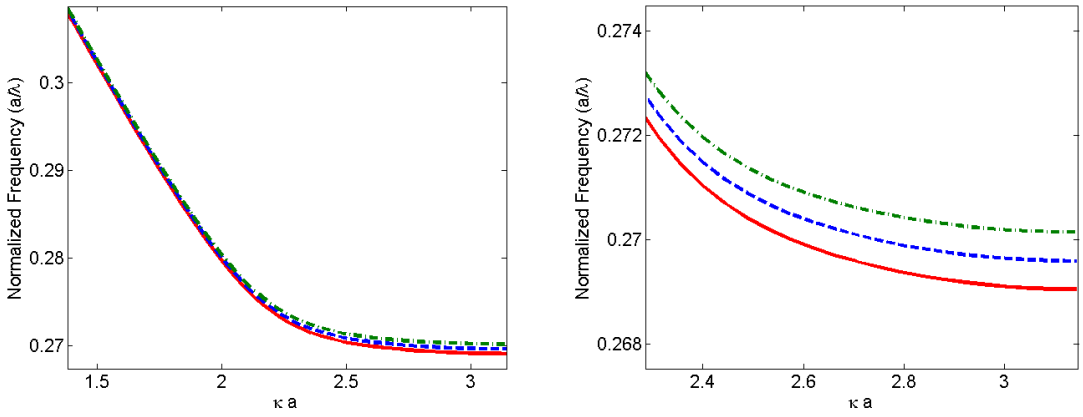

(a) (b)

Figure 13: (a) PWE obtained dispersion diagram of the single mode region of the PCW for three values of number of plane waves: 19 (red solid curve), 17 (blue dashed curve), and 15 (green dash-dotted curve). A magnified version of the dispersion around the non-linear region is shown in (b).

velocity region are shown in Table 3. The difference between the FDTD obtained and analytical modeling obtained group delay is less than 3% for each case. Similarly, the numbers predicted by the three dispersions for the pulse spread are also very similar.

Table 3: Comparison of FDTD obtained group delays and those predicted by the modeling of the three dispersions shown in Figure 13. The center frequencies in each case lie in the linear (or high group velocity) region of the three dispersions [1].

ω_o	$d\omega/\omega_o$	**Group Delay**			
		FDTD	**PW = 19**	**PW = 17**	**PW = 15**
0.2865	4.5exp(-5)	3.554100	3.644700	3.677400	3.710700
0.2827	2.59exp(-5)	3.89900	4.040900	4.008200	4.041500

In Figure 13(b), I show the zoomed in version of the three dispersions of Figure 13(a). The dispersions have been zoomed in around the non-linear (low group velocity) region of the dispersions. The figure shows that there is considerable difference between the dispersions at low group velocities. Similar to the discussion

in Section 4.1.1, the three dispersions will predict considerably different group velocities and other Gaussian statistics. For example, consider a pulse with a center frequency of 0.2685 and a bandwidth of $2.4605\exp(-5)$, the group index obtained from the FDTD simulation for a length of 302 period PCW was 21.0124. However, the group delays predicted by the dispersions of Figure 13 in my analytical model are considerably different numbers (29.948 for PW = 15, 116.636 for PW = 17, and 274.5341 for PW = 19). As is obvious from Figures 13 and 8, the dispersion not only shifts as we change the number of plane waves used in the PWE method, the dispersion is also different; i.e., for the same group delay different dispersions will predict different pulse standard deviation and skewness. In the next step, I used the shifted versions of these dispersions to find the best match. For example, when we find the group delay as a function of frequency for the dispersion with 19 planes waves we see that we get the same delay of 21.0124 at a different frequency of $\omega_o = 0.2708$. If I shift this dispersion down by the difference 0.0023 (0.2685 - 0.2708) and use this shifted dispersion in my analytical model I get the same delay as that obtained from the FDTD simulation, and the results for pulse spread and skewness are also very similar. I repeated the same procedure with other dispersions as well to find the dispersion that results in best match with the FDTD results. The dispersion with 19 plane waves gave us the best results. Figure 14 compares the FDTD obtained and the analytical model predicted percentage increase in the pulse standard deviation (σ) with respect to the input pulse and the evolution of skewness parameter (γ) as the pulse propagates through a 302 layer PCW. The difference in the predicted value and the actual FDTD obtained value for the increase in σ is less than 1% after a propagation of 302 layers of PCW. Also the skewness result agree pretty well with the FDTD simulation results [1]. Thus, our model with the use of shifted dispersion correctly predicts the group delay, pulse standard deviation and the skewness of a Gaussian pulse propagating inside

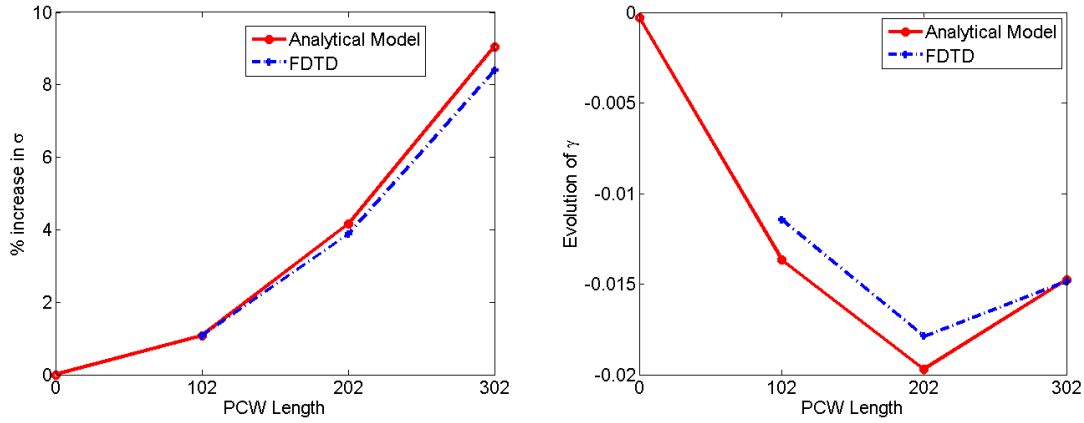

(a) (b)

Figure 14: Comparison of FDTD obtained (blue dashed) and analytical model predicted (red solid) Gaussian parameters. (a) Comparison of % increase in pulse standard deviation (σ) and (b) evolution of skewness (γ) as pulse propagates through 302 layers of a PCW.

the PCW. Note that our analytical model takes less than a minute to find all these parameters, whereas the FDTD simulations took six days in total on a computer cluster of 16 processors. To obtain the FDTD simulation points in the figure, I had to run three parallel FDTD simulations with 102, 202 and 302 layers of PCW. The pulses were monitored in the output slab waveguides of each simulation. When I use the same shifted version of dispersion to compute the group delay for the two operating points mentioned in the Table 3, I get less than 0.5% difference from the FDTD obtained results.

In my analytical model, I am modeling the propagation of Gaussian pulses through a medium with a given dispersion. This dispersion could be of a PCW, or a hypothetical medium that is homogeneous but dispersive. In other words, the model can predict the Gaussian pulse propagation characteristics for any medium as long as we know the dispersion of the medium. In yet another way, we can say that I am modeling the PCW as a homogeneous dispersive medium. With this understanding, we can say that the good comparison between the analytical

model and the FDTD results shows that a PCW can be modeled as a dispersive homogeneous medium. With this model, we can cut down the large simulation times on a cluster of computers to seconds on a single PC (personal computer), thus saving time and computational resources. All these gains have been achieved without compromising the validity of the results.

CHAPTER V

PCW BENDS

Bends are an integral part of any integrated optics platform; they allow compact integration of multiple optical functionalities in a single chip. The spatial extent of bends in a PCW is on the order of a lattice period. The lattice period in a PCW is of the order of the wavelength of light (inside the PC material), thus the size of bends in PCWs, is roughly on the order of the wavelength of light. Compare this to bends in a silicon ridge waveguide platform, where radiation becomes a major loss mechanism for any bend radius below 5 μm; bends in PCWs are more than an order of magnitude smaller. The smaller bends in PCWs make these PCWs a promising candidate for compact integrated optical functionalities.

An ideal bend must provide high transmission and low dispersion over a large bandwidth. Although dispersion is not a critical parameter in waveguides with continuous translation symmetry, it can be a limiting factor in application of waveguides with discrete translation symmetry, which are inherently dispersive. Extensive research has been carried out to design PCW bends with high transmission [70, 71, 7]. However, the dispersive behavior of PCW bends has largely been overlooked. Since PC structures are inherently dispersive, any design for bends in PCWs should consider their dispersive behavior, especially when wide bandwidth is required (e.g., in ultrafast optics) or in situations when an optical signal goes through a PCW bend multiple times (e.g., in a loop-based delay structure).

In this part of my research, I studied PCW bends keeping both their transmission and dispersion behavior in view. I identified the air holes that have the most

effect on the PCW bend performance and showed how these air holes can be engineered to achieve both high transmission and low dispersion over a large bandwidth. I have come up with a systematic method of designing high performance bends, which is discussed along with the comparison of our designed bends with other reported bend designs in this chapter.

5.1 Design Philosophy and Simulation Platform

Different design methodologies have been used to design PCW bends. In one approach the bend has been modeled as a cavity, and the design is based on tuning its resonance and field profile to achieve high transmission [70]. In another approach, the bend is modeled as an impedance-matching region, and the design is focused on optimizing the impedance of the bend region to achieve minimum reflection [71]. Both these techniques are inherently used for low bandwidth matching and these techniques do not result in a wide bandwidth PCW bend due to the narrow band nature of resonance or impedance matching. The PCW bend design technique proposed here, on the other hand, is based on the mode matching technique [7] that can allow wide bandwidth operation. As throughout my research, I have also used the triangular lattice PCWs for designing high performance PCW bends. While this lattice is the most widely used platform, our approach is very versatile and can be easily extended to other 2D PC lattices. In our approach, we model the PCW bend as a coupling section (CS) between two (ΓJ directed) waveguides [7], as shown in Figure 15.

The input light couples from the input waveguide (ΓJ section) into the PCW bend, coupling section (CS) or ΓX section, and then couples into the output waveguide (ΓJ section). To ensure good transmission over a large bandwidth, the guided modes within the two sections (i.e., the ΓJ and ΓX) must be similar in terms of both

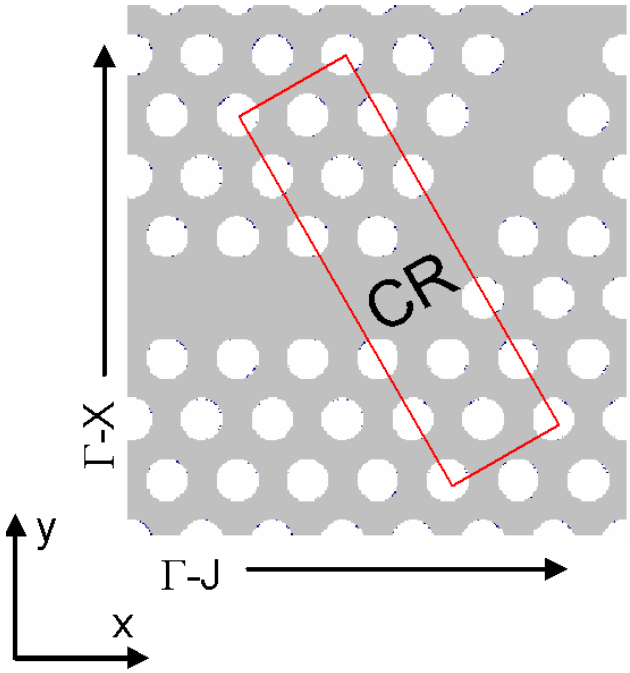

Figure 15: Simulation structure indicating the coupling section (CS).

the dispersion and the field profile of the modes. The dispersion provides information about the number of modes and the group velocity of the modes. When light - propagating in a single mode - couples from one section to another, the energy is distributed into the modes of the second section; hence, it is important that the second section is also single mode so that the energy is not coupled to unwanted modes. Similarly, the group velocity of the modes in the two sections should be similar to avoid reflections. The field profile, on the other hand, provides information about the distribution of the electromagnetic field along the guiding region. Since the tangential fields are continuous at an interface, it is important to match the field profiles of the two sections to avoid power reflection at the interface.

Figure 15 shows a 2D PCW bend in a triangular lattice PC of air holes (with radius r) in Si. To simplify the simulations, we have used the effective index model for Si ($n_{eff} = 2.811$) to allow for 2D analysis. The effective index is calculated using a one dimensional (1D) mode solver [72]. The radius of air holes is $r = 0.3a$ (a = lattice constant) to ensure maximum photonic bandgap (PBG) for transverse

magnetic TM modes (i.e., modes with magnetic field perpendicular to the plane of periodicity). It is generally preferred to have two PCW bends to have parallel input and output waveguides. However, in our simulations we have used only one PCW bend to avoid the Fabry Perot (FP) effect due to reflection between the bends. We have used 2D finite difference time domain (2D-FDTD) [19] with incorporation of absorbing boundary conditions [73] to analyze the PCW bend transmission and dispersion characteristics. For our simulations, lattice period (a) is equal to 24 FDTD grid points. To calculate the PCW bend power transmission spectrum in 2D-FDTD, we used a pulsed Huygens source [62] to excite the fundamental TM mode in the slab waveguide that is coupled to the simulation structure. The spectrum of the power transmitted through the bend is calculated by taking the Fourier transform of the fields and then integrating the Poynting vector over a surface of 161 grid points, centered at the middle of the output PCW. It is important to note that a point observation surface is not suitable for recording fields in a PCW waveguide as the transverse mode profile changes a lot going from a high group velocity mode to a low group velocity mode. The power transmission spectrum is then calculated as the ratio of the power transmitted through the bend to the power transmitted through a similar PCW structure of equal length but with no bends. This allows us to remove the effect of coupling from the slab waveguide to the PCW. For calculating the band structure and field profile of the modes in the two sections, we have used the plane-wave expansion method [17] with the super cell technique. To further reduce the computation cost we have employed the effective index approximation to simplify the problem from three dimensional (3D) to 2D. The effective index used in our calculation is the same as the one used in our 2D-FDTD calculations.

5.2 *Bend Design*

The dispersion diagrams of the guided modes of the two sections: ΓJ and ΓX, are shown in Figure 16(a). We concentrate on the single mode normalized frequency region for the ΓJ waveguide $0.266 \leq \omega_n \leq 0.291$, eclipsed in Figure 16(a). This range of frequencies is of most interest for integrated optics applications. Figure 16(a) shows that the ΓJ section has a single mode in the frequency range of interest, whereas ΓX section has two modes. It is also evident from Figure 16(a) that the modal dispersion of the two sections are different in the frequency range $0.266 \leq \omega_n \leq 0.272$; the ΓJ section has low group velocities, whereas ΓX section has large group velocities.

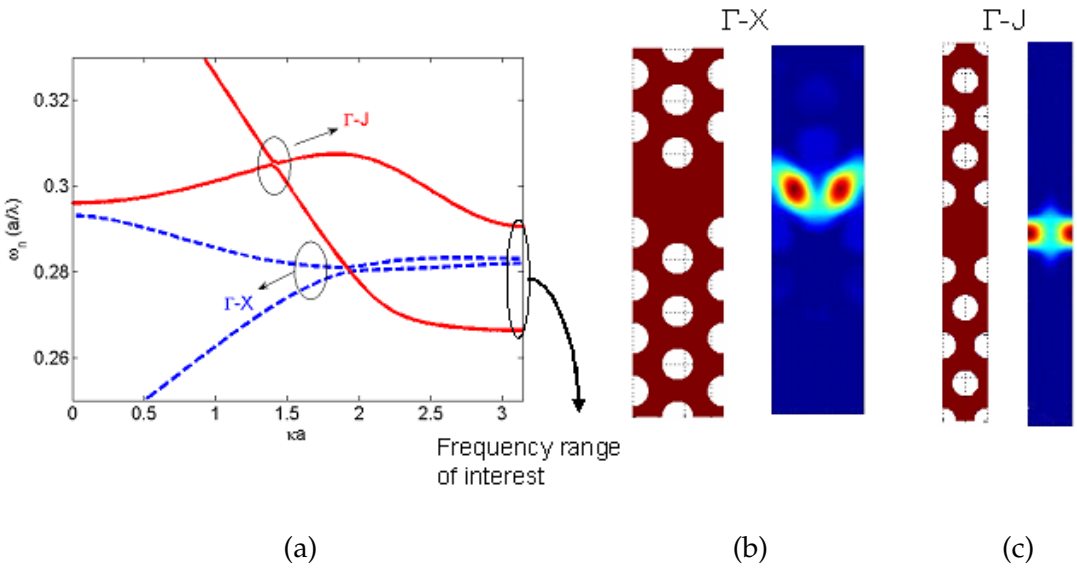

Figure 16: (a) Dispersion diagram for ΓJ (solid) and ΓX (dotted). (b) Unit cell and field profile (Hz) at $\omega_n = 0.27$ of the even-like mode for ΓX (or CS) section. (c) Unit cell and field profile (Hz) at $\omega_n = 0.27$ for the even mode in the ΓJ section.

Figure 16(b) and (c) show the intensity profile for the out-of-plane (or z) component of the magnetic field of the even and even-like mode in the ΓJ and ΓX sections respectively. Here, we are using the terms even-like and odd-like for the modes in the ΓX section because they have similar field profiles to even and odd modes of

the ΓJ waveguide, but they can not be termed as even/odd in the ΓX section as this section lacks mirror symmetry. The location of the intensity maximum within the unit cell is different for the two sections; it is concentrated at the edge of the unit cell of the ΓJ waveguide along the x-axis (see Figure 16(c)), whereas it is shifted towards the center of the unit cell for the ΓX waveguide (see Figure 16(b)). Since the tangential component of the magnetic field is continuous at an interface, it is expected that the difference in the location of the intensity profiles of the two sections would result in unwanted reflections. Figure 17(a) and 17(b) respectively shows the transmission and phase response of the simple bend structure, shown in Figure 15. The phase accumulated by the pulse in going through the bend section is calculated by subtracting the phase of the output pulse through the bend simulation from the phase of the output pulse through the straight PCW simulation.

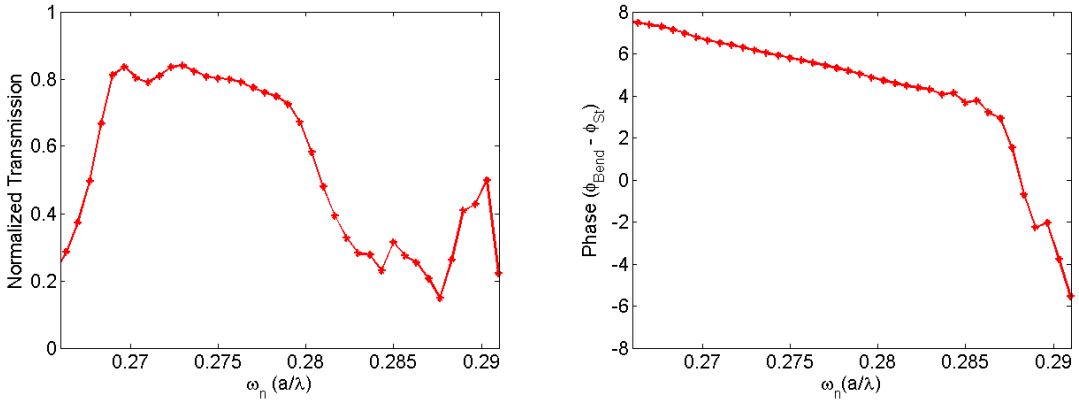

(a) (b)

Figure 17: (a) Transmission and (b) phase of the simple bend, structure shown in Figure 15 with r/a = 0.3. The transmission and phase through the bend is normalized to those through a straight PCW with similar length.

The total length of the PCW is kept the same in the two simulations, which allows us to extract the phase that the pulse accumulates while passing through the bend section. The differences in the dispersion and field profile of the two sections (i.e., ΓX and ΓJ in Figure 16(b) and (c)), as noted above, reflect as an overall reduction of

transmission and the presence of low transmission regions at the lower and upper ends of the single mode frequency range as shown in Figure 17(a). The phase response also shows strong dispersive behavior in the upper end of the frequency range of interest (see Figure 17(b)).

5.2.1 Effect of Individual Air Holes

Figure 16(b) shows that the electromagnetic energy in the bend section is mainly concentrated in the middle of the waveguide region. Therefore, it is expected that the holes in the vicinity of the center of the waveguide region would have the maximum effect on the transmission and phase response of the bend. Thus, our design approach was to optimize the bend section, to achieve a better transmission and phase response, by engineering the size of the air holes that are in vicinity of the maximum field region [74, 2]. We identified five holes in this region and represent them by their radii, as shown in Figure 18. It was important to first study the effect of individual air holes on the dispersion and the field profile of the coupling section, before we could design better PCW bends.

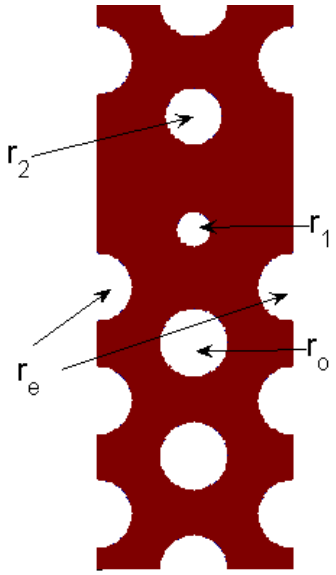

Figure 18: Important air holes for control of dispersion and field profile in a PCW bend.

The air hole identified as r_1, in Figure 18, is close to the center of the ΓX guiding section of the bend. The effect of increasing r_1 on the dispersion of the guided modes of the ΓX section is shown in Figure 19(a). As r_1 is increased, the ΓX dispersion moves to higher frequencies. This can be used to make the coupling section single mode in the frequency range of interest, by moving the range of frequencies in which ΓX has two guided modes out of the frequency range of interest (i.e., the single mode region of the ΓJ section as shown in Figure 16(a)). Since the even-like mode is more concentrated in the center of the guiding region as compared to the odd-like mode, the effect of increasing r_1 is more pronounced for the even-like mode. Increasing r_1 moves the even-like mode up in frequency more than the odd-like mode causing a decrease in the single mode bandwidth of the even-like mode of the ΓX section. The effect of increasing r_1 on the field profile of the even-like mode of the ΓX section, shown in Figure 19(b) and 19(c), is twofold. The field profile moves outward towards the edges of the unit cell of the coupling section. Thus, it provides a better match to the field profile of the even mode of the ΓJ section. It also moves the field profile upwards (i.e., towards the inside of the bend); thus, it helps the electromagnetic energy to bend inwards.

The above discussion illustrates the effect of increasing r_1 on the dispersion and the field profile of the ΓX section. However, hole radius r_1 can not be increased beyond a value of $r_1/\mathrm{a} = 0.25$ (if this was the only hole radius we were changing) as above this value of r_1/a the lower frequency edge of the even-like mode dispersion of ΓX section moves above the lower frequency edge of the even mode of the ΓJ section. In order to compensate for this, we have to reduce the radius of another air hole to bring the ΓX dispersion down. For this we reduce the radius of air hole r_2 that causes the dispersion diagram to move down, and the field profile of the ΓX section to move up towards the inside of the bend region. Decreasing r_2 also decreases the tilt in the field profile maximum causing it to look a lot more vertical

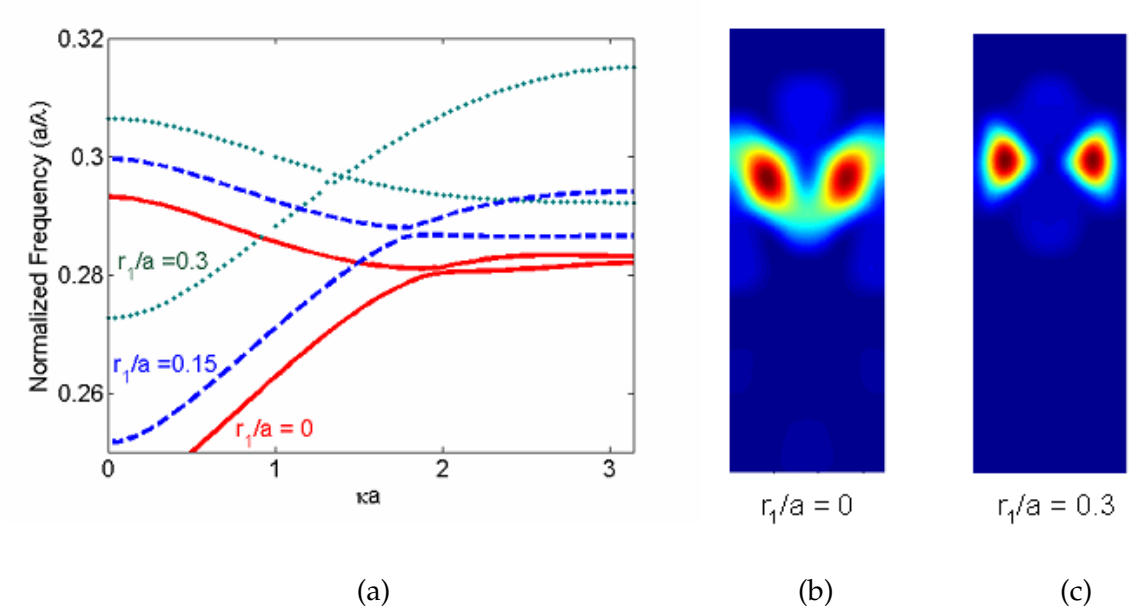

Figure 19: (a) ΓX waveguide dispersion as a function of r_1/a with $r_1/a = 0.0$ (solid), $r_1/a = 0.15$ (dashed) and $r_1/a = 0.3$ (dotted). (b) Field profile of the even-like guided mode in the ΓX region with (b) $r_1/a = 0.0$ and (c) $r_1/a = 0.3$. The size of all other holes is the same ($r/a = 0.3$) [2].

(i.e., similar to the field profile of the mode in the ΓJ section). These effects of changing r_2 are easily predicted by considering its location within the ΓX unit cell and the effect of r_1 on the dispersion and field profile. For example, if we reduce the value of r_2/a to 0.25 from its original value of 0.3 in a simple bend, the value of hole radius r_1/a can be increased up to a value of 0.31 without the low frequency edge of the even-like mode of the ΓX dispersion moving above the low frequency edge of the even mode of the ΓJ dispersion.

The effect of increasing the size of r_e in Figure 18 is shown in Figure 20. Figure 20(a) shows that the dispersion diagram of the even-like mode of the ΓX section moves up at larger r_e similar to what is observed for increasing r_1. On the other hand, since the r_e holes are at the edges of the guiding region, along the y-direction, the odd-like mode is more sensitive to the change in air hole r_e than the even-like mode. As a result the odd-like mode moves up more than the even-like mode,

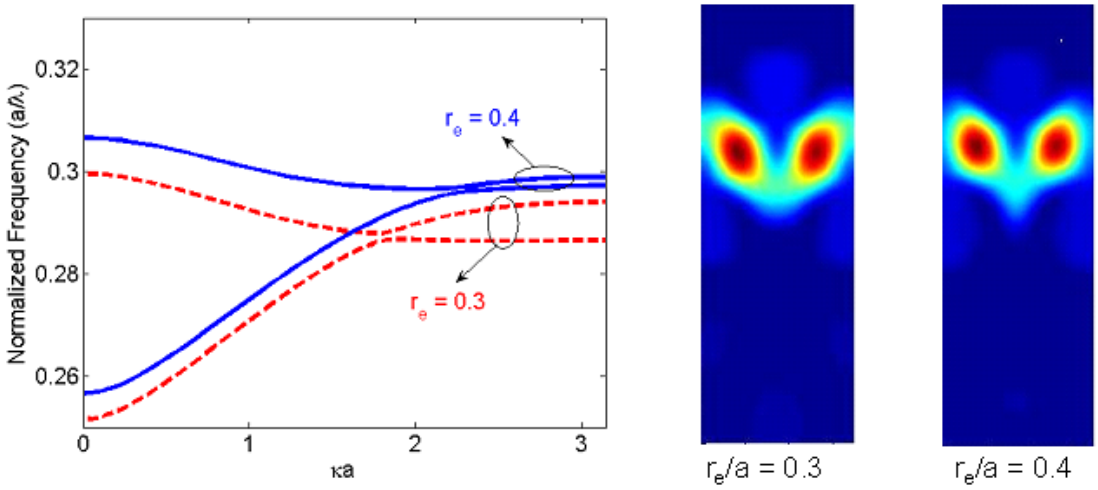

Figure 20: (a) Effect of increasing r_e in Figure 18, on dispersion diagram of the ΓX section. The field profiles of the even-like mode for (b) $r_e/a = 0.3$ and (c) $r_e/a = 0.4$. For these figures $r_1/a = 0.15$ and all the other hole radii are of value $r/a = 0.3$.

as shown in Figure 20(a). This increases the bandwidth of the single mode region with only even-like mode as the guided mode. By increasing r_e/a from 0.3 to 0.4, the odd-like mode moves out of the frequency range of interest at the higher frequency end. At the same time, increasing r_e pushes the field profile upwards (i.e., towards the inner corner of the bend) and helps bending the electromagnetic energy.

The primary effect of changing r_1, r_2, and r_e on the dispersion diagram is to move it up or down, and it has a minimal effect on its shape or slope. The slope of the dispersion, however, can be changed by modifying the holes that are not in the immediate vicinity of the guiding region (e.g., r_o in Figure 18). Figure 21 compares two ΓX dispersions with the ΓJ dispersion (dotted curve). The two ΓX dispersions, one with r_o = 0.37a (solid curve) and the other with $r_o = 0.38a$ (dashed curve), lie on top of one another for most of the frequency range of interest. The other hole radii ($r_1 = 0.28a$, $r_2 = 0.25a$, and $r_e = 0.4a$) are the same for these two

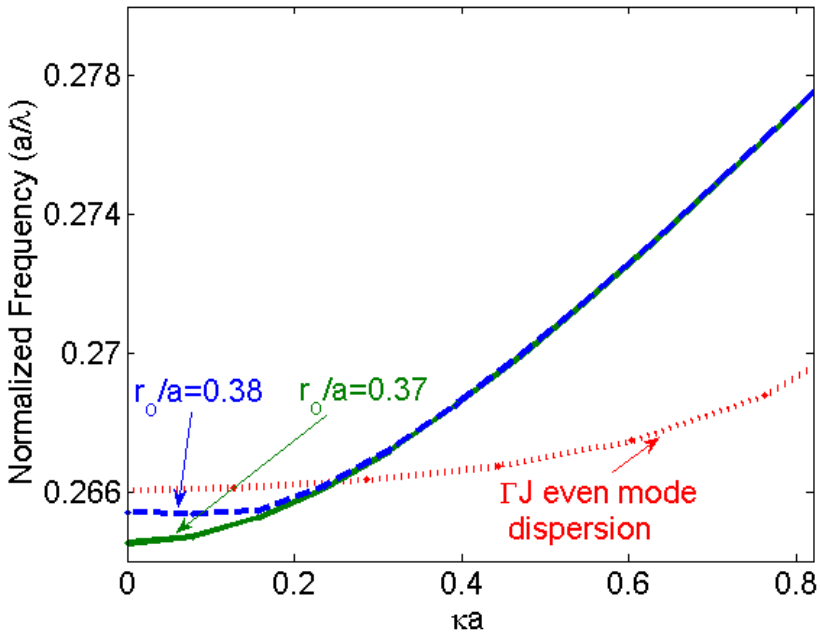

Figure 21: ΓX dispersion for different air hole radius r_o/a with other hole radii constant at $r_1 = 0.28a, r_2 = 0.25a, r_e = 0.4a$. The dispersion diagram of the structure with $r_o = 0.38a$ (dashed curve) is flatter than that for the structure with $r_o = 0.37a$ (solid curve). The dispersion of the even mode in the ΓJ section with $r/a = 0.3$ is shown for comparison (dotted curve).

dispersions. These two dispersions differ only at the low frequency end ($\kappa a < 0.2$), in which the dashed curve with a larger value of r_o is flatter. As we increase r_o the dispersion of the mode that lies below the even-like mode (not shown in figure to maintain clarity) moves up in frequency and couples with the even-like mode. This coupling causes the even-like mode to flatten. The air hole r_o can not be increased beyond the value of $0.38a$, as beyond this value the mode that lies below the even-like mode, moves into the frequency range of interest. Figure 21, also shows the dispersion of the ΓJ even mode (dotted curve), which suggests that the flatter the even-like mode of the ΓX coupling section, the more it resembles the ΓJ even mode dispersion. This would result in a better group velocity match over a larger range of propagation constant (κ) or frequency.

To further assist the electromagnetic energy to bend, we also use the interface

between the ΓJ incident section and the ΓX coupling section (see Figure 22(a) and 22(b)). The effect of increasing the radius of interface hole on the field pattern of the ΓJ even mode is shown in Figure 22(c) and 22(d). Increasing the radius of interface air hole (r_{int}), at the upper edge of the interface, tilts the field profile inwards, thus helping the electromagnetic energy to bend [74].

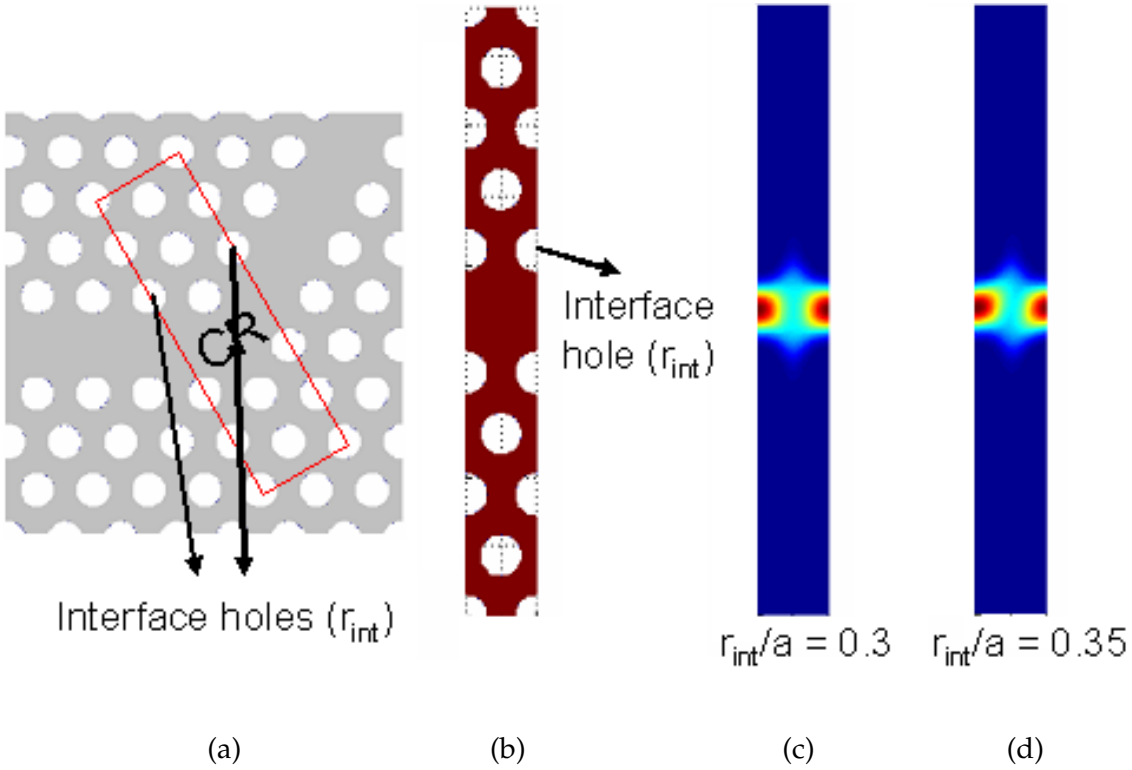

Figure 22: Location of interface holes in the bend region (a) and in the ΓJ unit cell (b). Field profiles for $r_{int}/a = 0.3$ (c) and $r_{int}/a = 0.35$ (d); all other holes have $r/a = 0.3$.

The effect of changing the location of air holes such as r_1, r_2 and r_o on the transmission and phase behavior of bends was also studied. Our simulations indicated that this change in location of air holes improves the transmission and phase response at large group velocities at the expense of transmission and phase response at low group velocities. Since our focus was on the low group velocity region, we did not consider changing the hole locations in our systematic design and optimization of the bend performance.

The main point of the above discussion is that each hole in the vicinity of the guiding region affects both the dispersion and the field profile of the mode in the ΓX section. Thus, any optimal design needs to take into account the coupled effect of all the air holes on both the dispersion and the field profile. The effect of individual air holes on the dispersion and field profile is summarized in Table 5.2.1. This table and the understanding gained in studying the effect of individual air holes was then used to systematically design PCW bends with both high transmission and low dispersion throughout the frequency range of interest. This systematic design is presented in the next section.

Table 4: Effect of individual air holes on the dispersion and field profile of the ΓX region [2].

Air Holes	**Effect on even-type mode dispersion**	**Effect on odd-type mode dispersion**	**Effect on field profile**
r_1	Major	Minor	Major
r_2	Major	Minor	Major
r_e	Minor	Major	Minor
r_o	Major (only at low v_g and negligible otherwise)	Negligible	Negligible

5.2.2 Systematic Design

Having studied the effects of individual air holes on the dispersion and field profile, we turned our attention to the systematic design [2]. First, the air hole r_e is increased to 0.4a, this pushes the odd-like mode up in frequency and increases the single mode guiding bandwidth of the even-like mode of the ΓX bend section. It also moves the field profile up towards the inside of the bend (see Figure 20 for the effects of increasing r_e on the dispersion). The air holes r_1 and r_2 are then used to align the lower frequency end of the ΓX even-like mode dispersion to the lower frequency end of the ΓJ even mode dispersion. This can be achieved for different combinations of r_1 and r_2 (e.g., $r_1 = 0.29a$ and $r_2 = 0.25a$; $r_1 = 0.32a$ and $r_2 = 0.22a$;

and $r_1 = 0.35a$ and $r_2 = 0.19a$) as the ΓX even-like mode dispersion is equally sensitive to both r_1 and r_2. Our simulations show that the transmission and the phase response for all of the above combinations of r_1 and r_2 are very similar with only minor variations in the transmission or phase in the frequency range of interest. Emphasizing more on the transmission at small group velocities, the best bend performance is obtained for $r_1 = 0.35a$, $r_2 = 0.19a$, $r_e = 0.4a$ and $r_o = 0.38a$ due to the better field profile match of the modes of the two sections (ΓJ and ΓX) at small group velocities. The value of 0.38 is chosen for r_o/a as it allows a better group velocity match for the even-like mode of ΓX section to the small group velocity modes of the ΓJ section (see Figure 21).

The above mentioned values of hole radii are an optimum within the parameter space explored in this study. Although this combination of hole radii may not represent the global optimum, it should provide an excellent starting point for more sophisticated optimization schemes (e.g., genetic algorithm) to obtain the global optimum.

The insensitivity of the transmission and phase response of our designed bends to different combinations of hole radii as mentioned above indicate a good tolerance of the structure to the change in size of air holes that might happen during fabrication [2]. We also studied the sensitivity of the bend performance to changes in hole radii to within a couple of percent of the optimized bend hole radii, as can be expected in fabrication. It was found that this random change in hole sizes results in only minor changes in transmission and phase response and hence, the designed bends have good tolerance to fabrication variations.

In Figure 23, we compare the performance of our optimized bend design with that of a simple bend (with no modification to the holes in the vicinity of the guiding region). Figure 23(a) shows that our design has higher transmission at both the high and low frequency ends of the single mode region ($0.266 \leq \omega_n \leq 0.291$), which

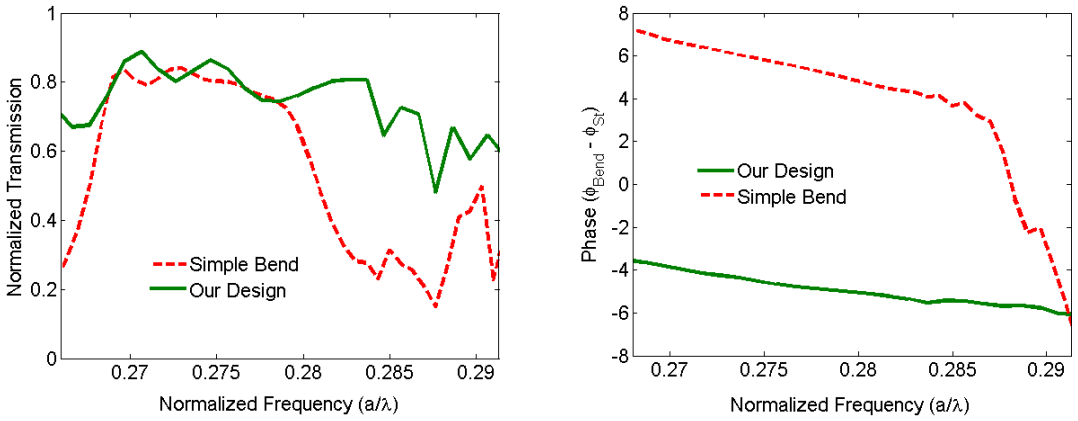

(a) (b)

Figure 23: Comparison of (a) normalized transmission and (b) phase of our bend design with $r_1 = 0.35a$, $r_2 = 0.19a$, $r_e = 0.4a$ and $r_o = 0.38a$ (solid curve) with a simple bend with $r_1 = 0$, $r_2 = 0.3a$, $r_e = 0.3a$ and $r_o = 0.3a$ (red-dashed curve). The PC is a triangular lattice of air holes in Si. For all other air holes $r/a = 0.3$ [2].

respectively correspond to fast and slow group velocity range of operation for the PCW bends. The 3 dB bandwidth of our design is almost twice that of the simple bend, and it covers the entire single mode guiding region of the input and output PCW. Figure 23(b) compares the phase response of our bend design with that of a simple bend. The phase response of our design is almost linear throughout the frequency range of interest, whereas the simple bend shows strong dispersive behavior at the high frequency end ($\omega_n > 0.285$). Thus, the dispersion introduced by our design would be negligible as compared to that introduced by the simple bend. The main advantages of our design as compared to a simple bend are that it has high transmission and negligible dispersion throughout the frequency range of interest.

5.3 *Comparison with Other Report Bend Designs*

In this section, we compare the results of our bend design with other bend designs reported in the literature [74].

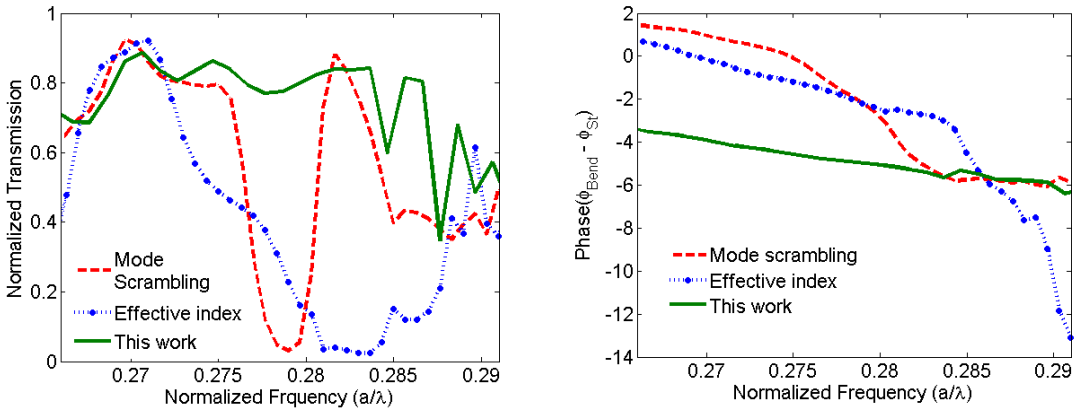

(a) (b)

Figure 24: Comparison of (a) normalized transmission and (b) phase response of our design (solid curve) with bends designed using the mode scrambling technique [5] (dashed curve), and that using the effective index matching technique [6] (dotted curve).

Benisty et al. [5] have treated the bend as a mode scrambler. They move the holes from the inner corner of the bend to the outer corner to convert the bend section from a single 60^o section to two 30^o sections. For a fair comparison, we simulated the design in [5] using our simulation platform and the results of the mode scrambling technique (dashed curve) are compared with our design (solid curve) in Figure 24. From the transmission comparison (Figure 24(a)), our design works better for most of the single mode frequency range. Only for a small range of frequencies around $\omega_n = 0.27$ does the bend designed using the mode scrambling technique perform better. However, this bend has very low transmission in the frequency range $0.277 \leq \omega_n \leq 0.281$. The phase response (shown in Figure 24(b)) of our design is considerably more linear than that of the mode scrambling technique of [5] that shows a strong dispersive behavior for frequencies $\omega_n > 0.275$. Actually,

even the phase response of a simple bend, as shown in Figure 23(b), is better than the phase response of the design in Ref. [5]. Hence, our design is less dispersive than the design reported in Ref. [5] for an optical pulse propagating through the bend.

Figure 24 also compares the performance of our bends (solid curve) with that of bends designed in [6] (dotted curve), simulated using our platform. In [6], Moll et al. reduce the size of the holes in the vicinity of the bend section to match the effective index that the mode encounters in the bend section to what it encounters in the straight waveguide section. From the transmission comparison in Figure 24(a), it is obvious that although the effective index scheme works well over a small bandwidth in the low frequency range, it results in a bend with low transmission for $\omega_n \geq 0.272$. Comparison of the phase response also shows that our design is less dispersive than the design reported in [6], which shows a strong dispersive behavior for frequencies $\omega_n > 0.283$.

Chutinan et al. [7] consider the bend section as a ΓX waveguide section, similar to what we used in our work. A simple bend has two modes, as shown in Figure 16(c). In [7] the bend section is made single mode by adding holes in the center of the waveguide. In Figure 25 we compare the transmission and phase response of the bend designed in [7] (dotted curve), simulated using our platform, and our bend (solid curve). The shape of the transmission curve in the two cases is reasonably similar but the transmission amplitude for our bend is better over most of the frequency range of interest, especially at small group velocities [2]. The phase response of the two designs is very similar, showing minimal dispersion. The point to note is that the design reported in [7] consists of four additional air holes per bend in the middle of the guiding region. These air holes in the middle of the guiding region will likely result in higher out-of-plane scattering losses, which can not be seen in 2D simulations and will require 3D simulations.

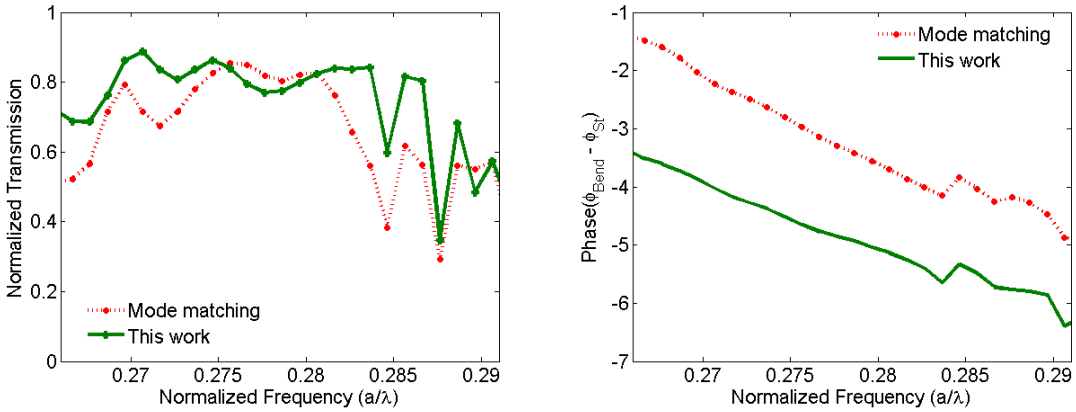

(a) (b)

Figure 25: Comparison of (a) normalized transmission and (b) phase response of the bend designed in this work (solid curve) with those designed by mode matching technique [7] (dotted curve).

The results presented in this chapter clearly show that a PCW bend can be modeled as a coupling section between ΓJ directed input and output waveguides. We showed that by matching the dispersion and field profile of the ΓJ guiding regions and the ΓX bend region in a triangular lattice photonic crystal waveguide, we can achieve both high transmission and linear phase response for the bend throughout the entire frequency range of interest. This design was achieved by systematically modifying the size of only four air holes in the vicinity of the guiding region in the bend. We also compared the transmission and phase response of our bends with other results reported in the literature and showed that our design provides better characteristics. Although we applied our approach to the triangular lattice PCWs, it is quite general and can be extended to any PC lattice.

5.4 Fabrication

We fabricated PCW samples with our designed bends using the fabrication process outlined in Chapter 3. We fabricated PCWs with single and double bend on the same chip, see Figure 26 (b) and (c) [8]. We also fabricated a straight ridge waveguide, and a straight PCW for comparison purpose; these are shown along with a PCW with a single bend in Figure 26(a). We have kept the length of the PCWs short to make sure the propagation losses (for modes above the light line, and for slow group velocity modes) do not confound our bend's characterization results. Also, as seen in the SEM images, we have used our designed couplers (see Chapter 6) to allow better coupling to low group velocity modes and to make sure the bend performance is not affected by this coupling. Although for simulations we have only used a single bend, as mentioned in Section 5.1, for fabrication and characterization we have used both single and double bends. For a single bend (as in Figure 26(a) and (b)), the output waveguide is at 60^o with respect to the input waveguide. To ensure the output waveguide is perpendicular to the cleaved output facet, we had to introduce a -60^o bend in the output ridge waveguide.

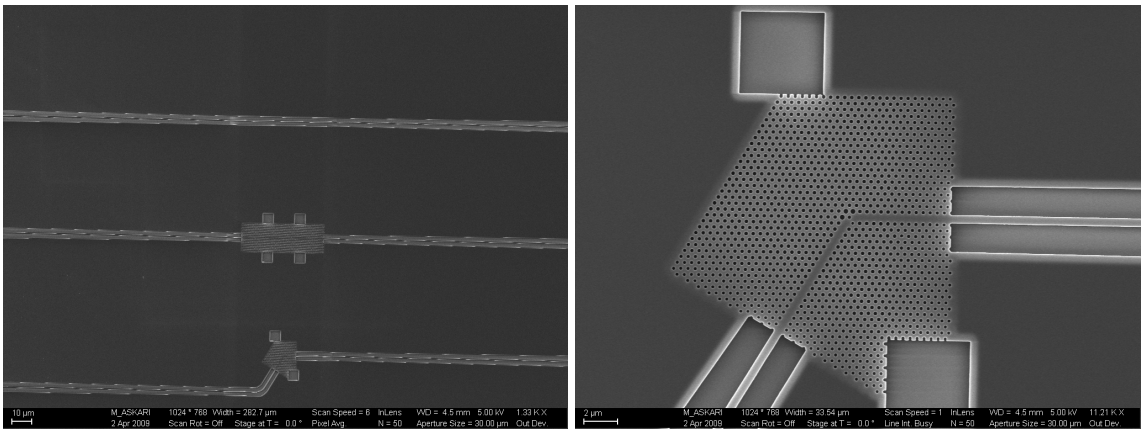

(a) (b)

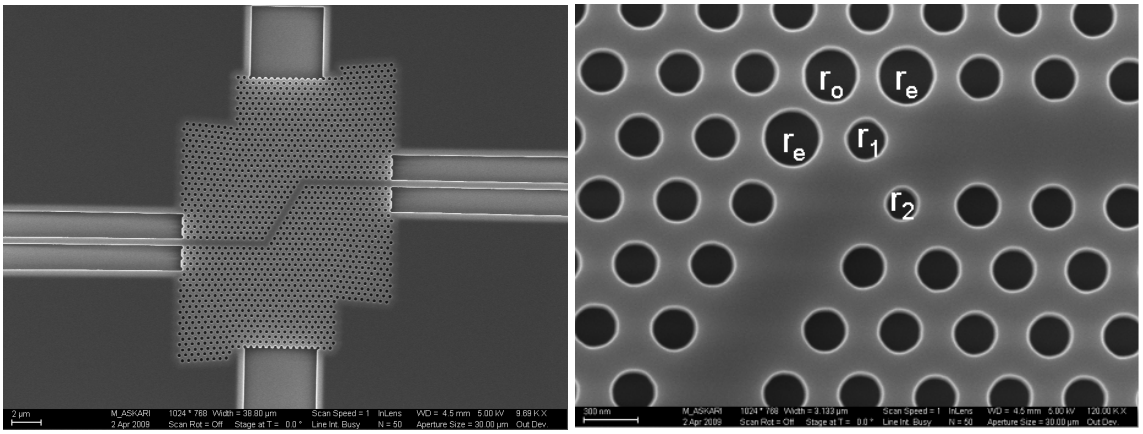

(c) (d)

Figure 26: SEM images of fabricated structures: (a) a ridge waveguide, a straight PCW, and a PCW with a single bend. (b) A close up of a PCW with a single bend. (c) A PCW with double bend, and (d) a close up of the bend region with the important air holes marked on the SEM.

5.5 Characterization

The fabricated bends were characterized using a swept wavelength setup. The setup consists of a tunable laser (Agilent Technologies Model 81680A, linewidth 100 kHz), operating in the continuous sweep mode, as the source. The light is coupled in and out of the chip through the access waveguides using single mode lensed fibers. The polarization of the input light is controlled using the fiber polarization controller. The output light is converted to an electrical signal in a photoreceiver (Thorlabs PDB 150C) and interfaced to a computer through a data acquisition (DAQ) card (National Instrument PCI-6251, 16-Bit, 1 MS/s). The start of each laser wavelength sweep triggers the DAQ card to start data acquisition. The characterization results of the fabricated structures are shown in Figure 27.

In Figure 27(a) and (b), we are comparing the transmission through a PCW with one and two bends respectively for our designed bends (blue solid curve) and a simple bend (red dotted curve) [75]. These two figures show that the response of our designed bends does not change except for 1 nm in the long wavelength range when we go from a single bend to two bends, whereas for a simple bend the cut-off at both the short wavelength and long wavelength edges becomes sharper; indicating that there is considerable loss in a simple bend when compared with our bend design. Figure 27(b) shows that with our designed bends, the 3 dB bandwidth is increased by 12-13 nm in the small group velocity region (long wavelength edge of the curve). The increase in transmission bandwidth at the large group velocity end is larger than 30 nm, shown in Figure 27(b), and extends to wavelengths smaller than 1460 nm allowed by this laser. We had to use another laser to find the short wavelength edge below which the transmission drops by more than 3 dB. The total 3 dB transmission bandwidth for large group velocities (shorter wavelengths) is around 42 nm. Combining the 3 dB transmission bandwidth increase at both the long and short wavelength ends results in a total of 55 nm bandwidth increase.

This to our knowledge is the highest reported increase in the 3 dB guiding bandwidth as compared to a simple bend. Figure 27(c) shows the same information as in 27(b) with the only difference that now the information is displayed in normalized frequency (a/λ) domain, to allow us better comparison with the simulation results of Figure 23(a). In Figure 27(c), for a simple bend the low frequency drop off in transmission occurs around $\omega_n = 0.269$ and the high frequency transmission drop occurs around $\omega_n = 0.281$; similar to what is predicted by simulations in Figure 23. Whereas the transmission through our bends remain high even above $\omega_n = 0.288$, similar to what was predicted by simulations (Figure 23(a)). Thus, using our bend design the transmission bandwidth increases from around 80 nm for a simple bend to around 134 nm, which is around a 70% increase in the total guiding bandwidth.

Figure 27(c) compares the transmission through a PCW consisting of two of our designed bends, see Figure 26(c), with that of a straight PCW, the middle structure of Figure 26(a). This figure shows that the 3 dB guiding bandwidth of our designed bends in only 1 nm less than that of a straight PCW. Thus, our designed bends allow very good transmission through almost the complete single mode frequency range of interest ($0.266 \leq \omega_n \leq 0.291$).

In this chapter, we discussed our approach to designing high transmission and low dispersion PCW bends. We showed that to design large bandwidth bends in PCWs we need to take into account both the dispersion and field profile of modes in the ΓJ and ΓX directed waveguides [2]. We showed that our design allows increasing the bandwidth of a PCW bend by almost 70%, which now effectively covers the complete single mode frequency range of the PCW used in this research.

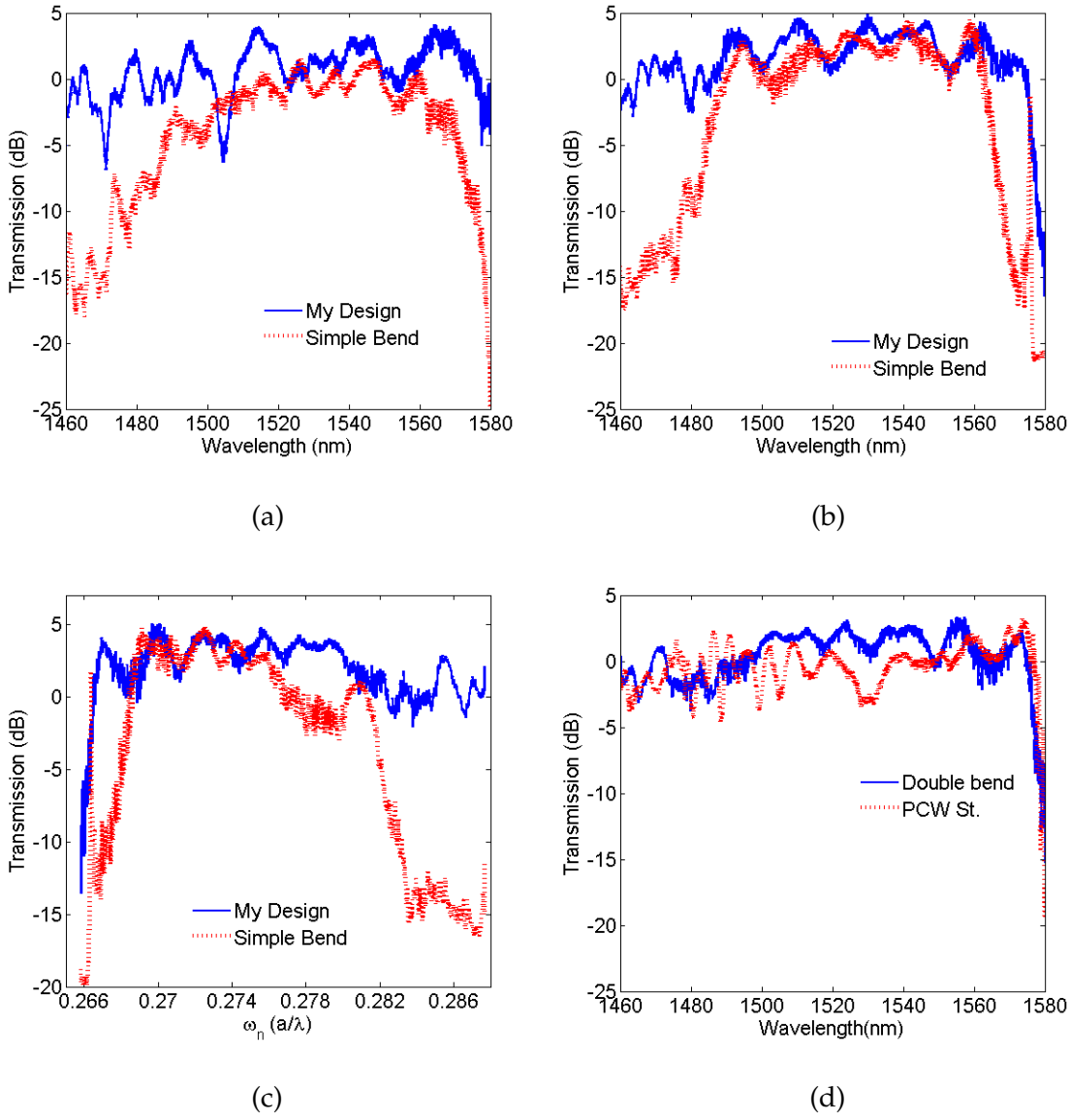

Figure 27: Comparison of the transmission response of our designed bend (blue solid curve) with a simple bend (red dotted curve) for (a) a single bend in wavelength domain, (b) a double bend in wavelength domain, and (c) a double bend in normalized frequency, $\omega_n(a/\lambda)$, domain [8]. (d) Comparison of the transmission response of a PCW consisting of two of our designed bends (blue solid curve) with a straight PCW, with no bends (red dotted curve).

CHAPTER VI

RIDGE TO PC WAVEGUIDE COUPLERS

For any technology to offer a viable integrated optics platform it should be able to perform well in all the building blocks of an integrated optics platform. These building blocks include waveguides, bends, couplers, cavities etc. This chapter deals with one of these important aspects of an integrated optics platform; i.e., coupling from a ridge waveguide to a PCW and vice versa.

Various research groups around the world have studied this coupling [76, 77, 78] and in this chapter we present our approach for efficient coupling of light into low group velocity PCW modes. Figure 28(a) shows the dispersion diagram of a W1 waveguide in a PC consisting of triangular lattice of air holes, with r/a = 0.3. The term W1 is widely used in the literature to refer to a waveguide with one row of air holes deleted from a perfect PC to form the PCW. The dispersion diagram has two distinct regions.

a) A linear region with almost uniform high group velocity.

b) A non-linear region with varying low group velocities.

The group velocity is given by the slope of the dispersion diagram ($\frac{\partial \omega}{\partial k}$). The larger the slope the larger the group velocity and vice versa. Most of the PCW based applications work in the low group velocity regime, as this region offers characteristics that are not available in a ridge waveguide platform. For example, this region has large dispersion and small group velocities. Also, the dispersion of this region is tailorable by changing the size or location of air holes next to the guiding region. This flexibility of designing the dispersion along with the low

group velocities that this region offers is not possible in a ridge waveguide platform. Some applications that use this region of the dispersion diagram are delay lines, dispersion compensation, PCW based wavelength division multiplexing and demultiplexing. As discussed in Chapter 1 a typical structure envisioned for integrated optics applications is shown in figure 28(b). The light is coupled on chip into a Si ridge waveguide. The Si ridge waveguide is then coupled to a PCW. Optical processing takes places inside the PCW region. The light is then coupled back into a ridge waveguide and routed to other optical processing blocks based on PCs or for output coupling. Thus each optical chip can consist of a number of ridge to PCW couplers. Hence, these couplers were studied as part of this research and one of the goals of the research was to develop high bandwidth and efficient ridge to PCW couplers. For achieve this goal, we studied various factors that affect coupling of light from a ridge waveguide into a PCW, and showed how these factors can be utilized to achieve high transmission over large bandwidths and especially in the low group velocity region of the even mode dispersion of a PCW.

6.1 Simulation Platform

To simulate the performance of a ridge to a PCW coupler, we have used the structure shown in Figure 40(a). The structure consists of a dielectric slab waveguide connected to a PCW with a coupling region in between. As mentioned in Chapter 1, the PC used throughout this research is a 2-D triangular lattice of infinite air columns in silicon ($n_{eff} = 2.811$). The refractive index of the dielectric slab waveguide is also that of silicon. The radius of air holes (r) is 30% of the lattice period (a) to ensure maximum PBG for TM polarized light (magnetic field parallel to the axis of air columns). The PCW is made by removing one row of air holes in the ΓJ direction. The width of the slab waveguides is equal to d, which is the same as the distance between the edges of the closest circle on each side of the PCW as

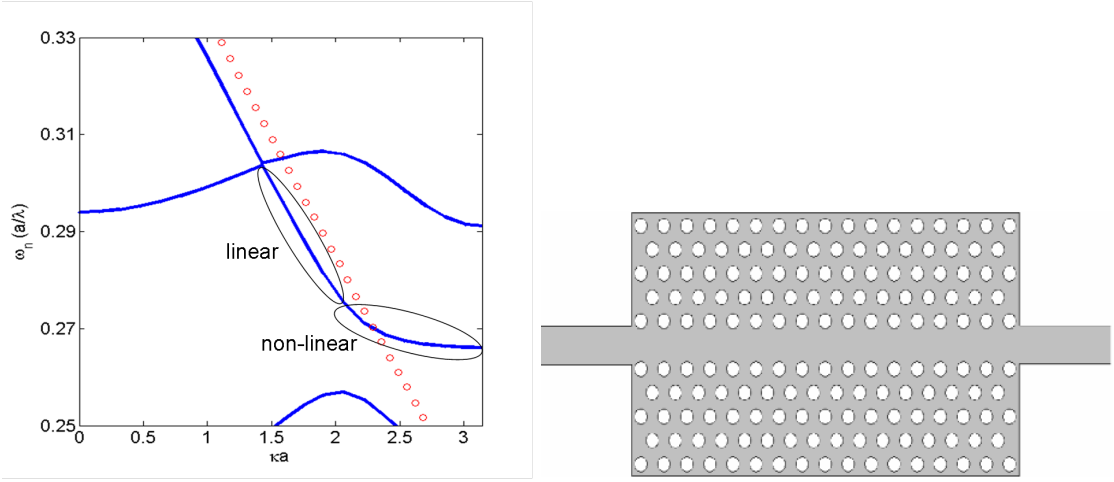

(a) (b)

Figure 28: (a) Dispersion diagram of a PCW (blue solid curve) showing the linear and the non-linear part of the even-mode dispersion. Also shown (red open circles) is the dispersion for the fundamental mode of a slab waveguide. (b) Structure of interest in most integrated optics applications consisting of PCW based functional blocks.

shown in the figure. To analyse the structure we used 2-D finite difference time domain (2D-FDTD) [18] method. To absorb the incoming electromagnetic fields and ensure there is no reflection from the ends of the structure we have used the adiabatic perfectly matched layers as designed in this research. More details on the adiabatic PML can be found in Chapter 7. In our simulations the lattice period (a) is equal to 24 grid points.

To calculate the power transmission spectrum (power transmission coefficient verses frequency) from the slab waveguide to the PCW, we used a pulsed Huygens source [62] to excite the fundamental TM mode in the slab waveguide. The spectrum of the power transmitted into the PCW is calculated by taking the Fourier transform of the fields and then integrating the Poynting vector over a surface of 168 unit cells (equivalent to 7 periods) centered at the middle of the PCW. This choice of the length of the observation surface is not arbitrary and was chosen to ensure the transverse profile of the mode does not affect the calculation of power

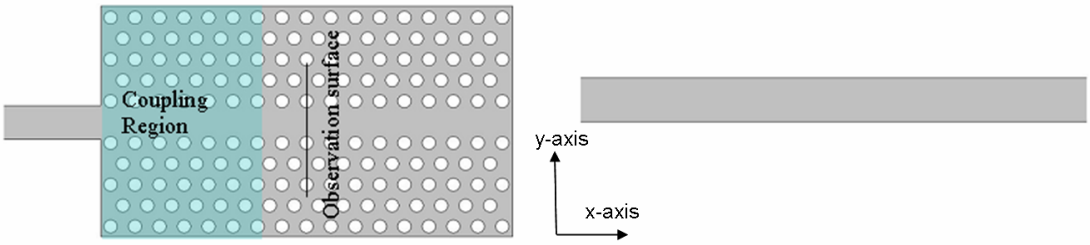

(a) (b)

Figure 29: (a) Structure used for simulating the coupling between a ridge and a PC waveguide. (b) Reference structure used for normalizing the transmission from a slab to a PC waveguide.

transmission coefficient. The length of the observation surface is important for our simulations as the transverse mode profile of the fundamental mode of the PCW changes as we move from the large group velocity region to the small group velocity region. This choice of the length of the observation surface ensures that the sum of the normalized transmitted and reflected powers is one throughout the frequency range of interest and does not change with the group velocity. The power transmission coefficient was calculated as the ratio of the transmitted power to the power transmitted through the reference structure of equal length and consisting only of the slab waveguide as shown in Figure 40(b).

To calculate the band structure, dispersion diagram, and field profile of modes we have employed the plane-wave expansion (PWE) method with super cell technique [17]. To further reduce the computation cost we have employed the effective index approximation to simplify the problem from 3D to 2D. The effective index used in our calculation is 2.811, the same as the one used in our 2D-FDTD calculations. This effective index corresponds to a thickness 250 nm of undercut Si slab used in our SOI fabricated devices.

6.2 *Design Philosophy*

Using the above mentioned simulation platform, we calculated the transmission spectrum for a simple butt coupled PCW (i.e., with no modification done to the PC in the coupling region of Figure 40(a)) in the single mode frequency range ($0.267 \leq \omega_n \leq 0.291$) of the PCW. The transmission response is shown in Figure 30(a).

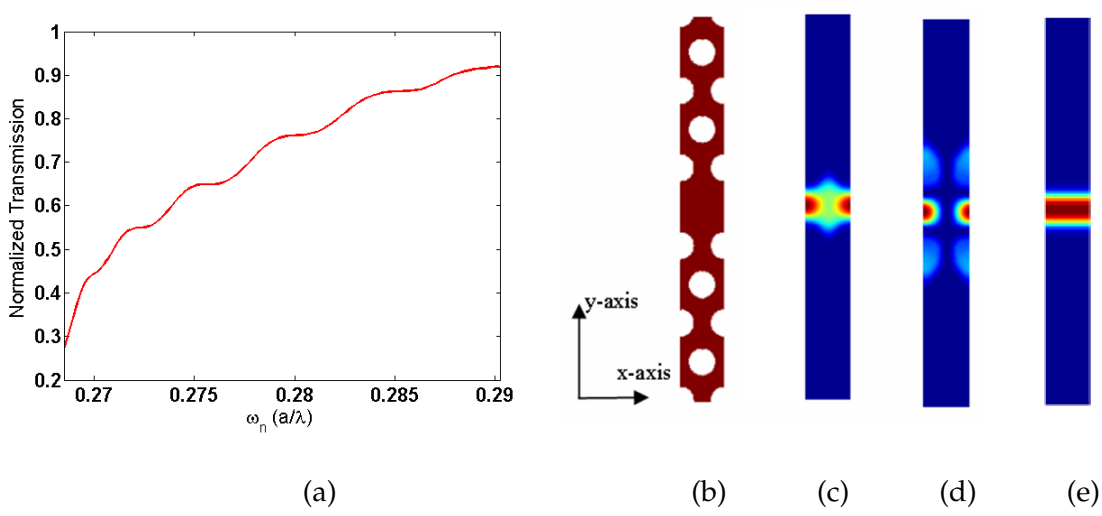

Figure 30: (a) Transmission from a slab waveguide to a butt coupled PCW. (b) Unit cell for calculating field profiles. (c) Field profile ($|H_z|^2$)of the even mode at $\kappa a = 1$. (d) Field profile of even mode at $\kappa a = \pi$. (e) Field profile for the fundamental mode of a slab waveguide.

The transmission drops from more than 90% at large group velocities to less than 30% at the lowest group velocity point of the dispersion diagram, which also happens to be the even mode cut-off point. Figure 30 also shows the field profiles ($|H_z|^2$) of the PCW mode in the linear and the non-linear regions of the fundamental mode dispersion. The field profile of the mode at low group velocity or the non-linear region, shown in Figure 30(d), is more spread out along the y-axis and sees more of the photonic crystal than the mode profile at large group velocity (Figure 30(c)) [79]. If we compare the field profile of the fundamental mode of a slab waveguide as shown in Figure 30(e) to the mode profiles of the PCW at low and high group velocities, we find that the slab waveguide mode profile is very similar

to the field profile at large group velocities and hence we see better transmission into the PCW at large group velocities. The difference in the transverse spread of the field profile of the PCW at low group velocity and that of the slab waveguide is one of the reasons for the low transmission of energy from a slab waveguide to a butt coupled PCW at low group velocities. The other reason is evident from Figure 28(a), where the dispersion diagrams of the PCW and the fundamental mode of the slab waveguide are plotted. The group velocity of the fundamental mode of the slab waveguide is very similar to that of the linear region of the PCW and hence the mode does not see much of a group velocity difference when entering from the slab waveguide into the PCW in the frequency range corresponding to the high group velocity/linear region of the PCW dispersion. The slab waveguide mode, however sees a large group velocity mismatch with the PCW mode in the low group velocity/non-linear region of its dispersion. This large group velocity mismatch is the other reason for the low coupling efficiencies at low group velocities. Thus there are two main reasons for the low transmission into low group velocity modes of the PCW.

(i) Group velocity mismatch

(ii) Modal profile mismatch.

We discuss our approach in solving this issue of low transmission in PCWs at low group velocities in the following subsections.

6.2.1 Taper Coupler

In our first design that we call Taper Coupler [79], we always couple light from a slab waveguide to the large group velocity modes of the PCW and then adiabatically transform the large group velocity modes to low group velocity target modes. This idea is motivated by the fact that we have a better group velocity and modal

profile match between the slab waveguide and the large group velocity region of the PCW mode. Figure 31(a) shows the dispersion diagram of a PCW as a function of r/a.

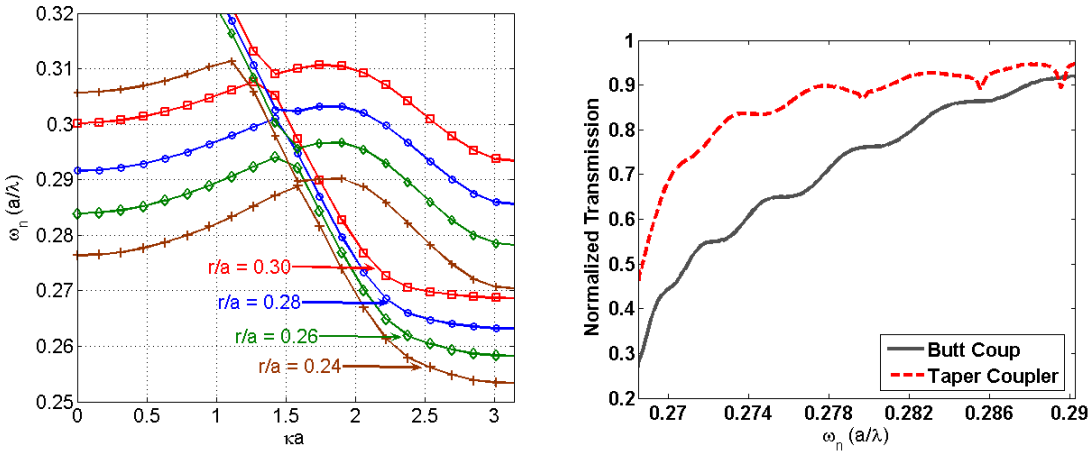

(a) (b)

Figure 31: (a) Dispersion diagram of PCW as a function of r/a. The dispersion is shown for four different values of r/a: r/a = 0.30 (red curve with squares), r/a = 0.28 (blue curve with circles), r/a = 0.26 (green curve with emeralds), and r/a = 0.24 (brown curve with plus signs). (b) Comparison of normalized transmission into a butt coupled PCW and a taper coupled PCW, where we have tapered the radius of air holes.

The dispersion moves to lower frequencies as r/a is decreased. Comparing the dispersion of a PCW with r/a = 0.3 (red curve with squares) and that of a PCW with r/a = 0.24 (brown curve with plus signs), we see that the low group velocity modes of a PCW with r/a = 0.3 lie in the same frequency range as the large group velocity modes of a PCW with r/a = 0.24. Thus, to couple light into the low group velocity modes of a PCW with r/a = 0.3, we can couple light to large group velocity modes of a PCW with a smaller value of r/a (e.g., 0.26 or 0.24) and then slowly change the PCW parameters to take it from the smaller initial value of r/a to the final value of r/a = 0.3. This decrease in the value of r/a can be achieved either by decreasing the radius (r) of the air holes, or by increasing the period, a. The effect of this taper

is shown in Figure 31(b), where we compare the transmission into a taper coupled PCW with that of a butt coupled PCW. The transmission into the slow group velocity modes of the PCW increases considerably by using the taper coupler instead of the butt coupler. For the taper coupler, the coupling region of Figure 40(a) consisted of a PCW in which the radius of air holes is linearly increased from an initial value of r/a = 0.24 to the final value of r/a = 0.30 over nine periods of the PCW. The period was kept constant (24 grid points of the FDTD grid) through the coupling region. The linear taper can also be implemented by keeping the radius constant and decreasing the period of PCW in the coupling region. These two tapers will be compared in the experiments section.

The boundary conditions for the electromagnetic fields dictate that the tangential magnetic and electric fields are continuous at an interface, so it is important to consider the tangential field profile of the modes in the slab waveguide and the PCW. In our case (TM mode) H_z is the tangential component of the fields at the interface of slab and PC waveguides. The field profiles for the PCW modes at high and low group velocities and the field profile for a slab waveguide fundamental mode are shown in Figure 30 (c) - (e). From the mode profiles of the PCW (Figure 30(c) and (d)), we see that the mode profile is not uniform and varies along the length (x-axis) of the unit cell. Along the x-axis, the field is maximum at the edge of the unit cell and is null in the center. Whereas, along the y-axis the field is maximum at the center of the Si slab, which is typical of a waveguide even mode. Since the mode profile of a slab waveguide is uniform along the x-axis of the waveguide with maximum in the center along the y direction (see Figure 30(e)), it is obvious that the location where we terminate the slab waveguide into the PCW would affect the transmission in to the PCW. This effect is shown in Figure 32(c), where we are comparing the transmission from a slab waveguide to a PCW for two different terminations.

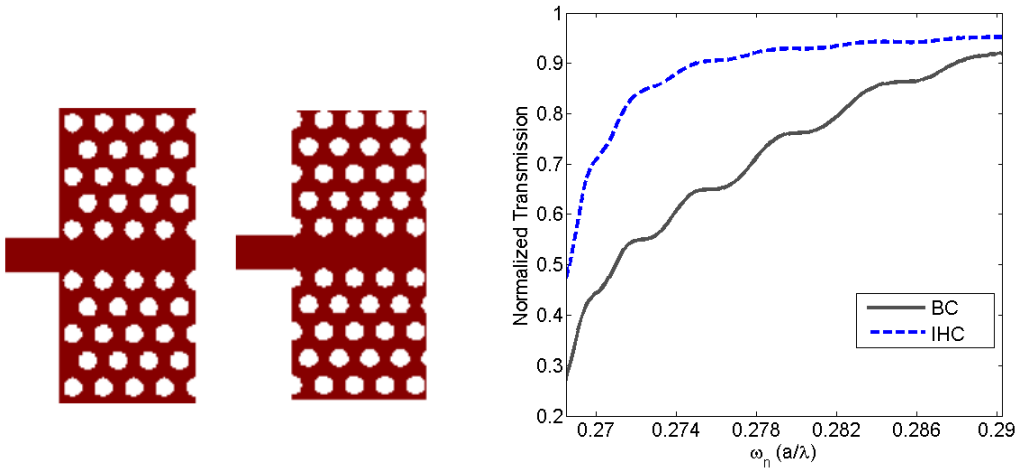

(a) (b) (c)

Figure 32: Two terminations used to study the effect of termination on coupling: (a) termination NC, and termination IHC. (c) Comparison of normalized transmission from a slab to a PC waveguide with terminations BC and IHC.

The two terminations: NC and IHC, are shown in Figure 32(a) and (b) respectively. Termination BC (butt coupled) is the same termination we have used to calculate transmission for the butt coupled PCW in Figure 30(a) and Figure 31(b). Termination IHC (interface hole cut) refers to the termination where we have joined the slab waveguide to the PCW right at the center of the air holes, or in other words to the edge of the unit cell as shown in Figure 30(b). Figure 32(c) compares the transmission into the PCW for these two terminations, which clearly indicates that the coupling improves considerably throughout the frequency range of interest and more so for low group velocities by merely changing the termination. The better coupling for the termination IHC is not unexpected, as the fields are maximum at the edges of the PCW unit cell as shown in Figure 30(c) and (d), with the transverse profile of the mode much similar to that of the slab waveguide mode profile as shown in Figure 30(e) [79].

Since we have an improvement in coupling due to two independent effects: tapering and termination, it seems logical to use both to find the optimum coupling

performance. To further optimize the coupling, we studied the effect of

i) length of the taper and

ii) the initial r/a .

To study the effect of the initial r/a, we fixed the length of the taper at $5a$ and studied the coupling as a function of the initial r/a. Transmission into the PCW for three different values of initial r/a: 0.24, 0.25, and 0.26 is shown in Figure 33(a).

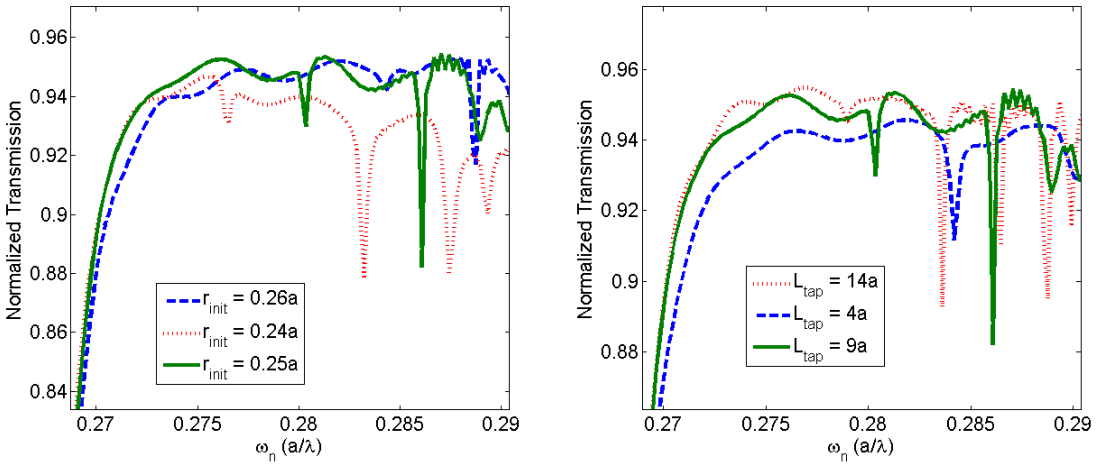

(a) (b)

Figure 33: Optimization of taper coupler. (a) Normalized transmission for three different values of initial hole radius (r_{int}): 0.24 (red dotted curve), 0.25 (green solid curve), and 0.26 (blue dashed curve). (b) Normalized transmission as three different values of taper length (L_{tap}): $4a$ (blue dashed curve), $9a$ (green solid curve), and $14a$ (red dotted curve).

The best performance is obtained for the coupler with an initial r/a = 0.25. The coupler with this value of initial r/a performs better than the coupler with an initial r/a = 0.24 in the large group velocity region of the target PCW (r/a = 0.3), as the odd mode for a PCW with r/a = 0.24 lies in the same frequency range as the large group velocity modes of the target PCW with r/a = 0.3. Similarly, the coupler with an initial r/a = 0.25 performs better than the coupler with an initial r/a = 0.26 in

the low group velocity region (low frequency end of the transmission curve), as the low group velocity modes for a PCW with r/a = 0.26 have some overlap with the low group velocity modes of the target PCW (with r/a = 0.3).

To study the effect of length of the taper on the transmission, we kept the initial *r/a* constant at 0.25 and varied the length of the taper. The effect of varying the length of the taper on the transmission is shown in Figure 33(b). As expected, we see better performance for longer taper lengths, as the electromagnetic energy sees a more gradual change in the PCW parameters (r/a) and hence smaller difference in the local mode properties. Another point to note is that we see more dips in transmission as we increase the length of the taper. This observation is easily explained by the Fabry-Perot effect. From Fabry-Perot theory we know that the longer the length of the cavity the more dips we see. Also the dips get sharper as the length of the taper increases. Thus, depending on the application we can choose a longer taper length if the application does not require broadband operation and is only concerned with the transmission at low group velocities or we can use a shorter taper if the application uses the entire single mode bandwidth of the PCW.

By combining the effects of better group velocity match (achieved using tapers) and better field profile match (achieved using the IHC termination) between the modes of the slab and the PCW modes, we expect to get the best performance possible using the adiabatic matching approach. In our final design we combine the effect of both tapering *r/a* and the IHC termination. In Figure 34 we plot the transmission response for our final design (green dashed curve).

In our final design, we linearly tapered the *r/a* from an initial value of 0.25 to the target value of 0.3 in nine periods of the PCW, with the period *a* fixed at 24 grid points. For comparison purposes, we have also plotted the transmission response for a coupler with an IHC termination and no input taper (blue solid curve with

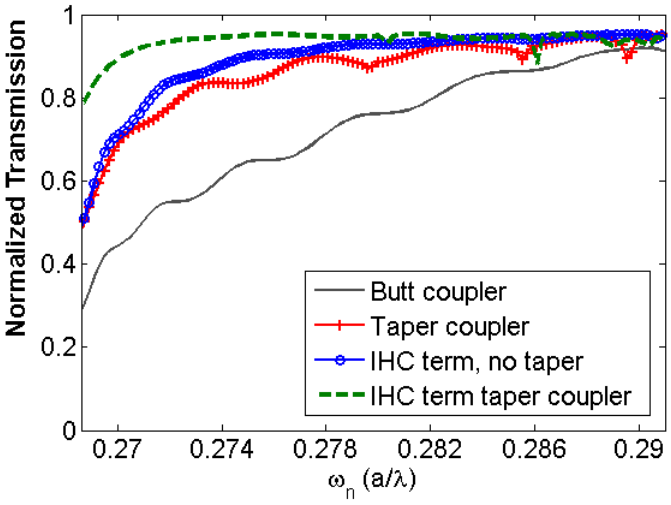

Figure 34: Comparison of normalized transmission for the final design, IHC term taper coupler (green dashed curve) with IHC term coupler without taper (blue solid curve with circles), taper coupler without IHC term (red solid curve with plus signs) and a simple butt coupler.

circles) and a coupler with an input taper without the IHC termination (red solid curve with plus signs). These two curves shows the individual effects of better mode profile match and better group velocity match, respectively. Also shown for comparison is the response from a butt coupled PCW(black solid curve). The figure clearly shows that by combining these two effects (group velocity match and mode profile match), we can get almost a constant transmission of around 95% throughout most of the frequency range of interest. The improvement in transmission is better for lower group velocities with the transmission at the low group velocity edge having increased from 27% (for the butt coupled case) to 77%.

6.2.2 Air wedge Coupler

In the taper coupler design, we improved the coupling into the low group velocity region of the PCW dispersion by coupling light into the high group velocity region of the PCW and then adiabatically transforming the high group velocity modes into the low group velocity modes. For the air wedge coupler, we thought

of directly modifying the slab waveguide mode into the PCW mode. To achieve this coupling, we thought of the structure shown in Figure 35. The idea is to start from a slab waveguide and gradually transform it into a PC waveguide. In other words, we start by replacing the slab waveguide structure with the PCW structure at a location where the evanescent fields of the slab waveguide mode are very small in amplitude and linearly move to larger and larger field values (i.e., towards the middle slab region) until we have completely transformed the structure into the PCW.

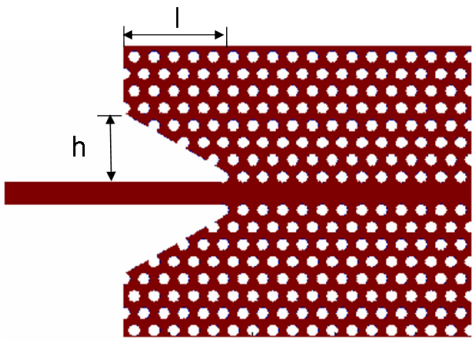

Figure 35: Schematic of an air wedge coupler. Height (h) and length (l) are the two parameters used for optimizing the performance of the coupler.

From the schematics of air wedge coupler, as shown in Figure 35, we have two parameters to consider for optimizing the coupler performance. The two parameters are:

(a) the height of the air wedge, shown as h in the figure and

(b) the length of the air wedge region, shown as l in the figure.

The height of the air wedge coupler was varied in steps of a_y (the periodicity along y-axis). The evanescent field of the PCW mode at low group velocity extends roughly one a_y, along the y-axis direction, into the PC as shown in Figure 30(d). Hence, $h = a_y$ is not a good choice. For $h = 2a_y$ (second hole away from the middle slab along y-axis), there is very little field amplitude for either the PCW modes

(Figure 30(c) and (d)) or the slab mode, and therefore is a good choice for the height of the air wedge coupler. With $h = 2a_y$, the evanescent field has decayed enough that the mode profile does not see much of a discontinuity, as it evident from Figure 36. Since we can get 100% transmission into the PCW for an air wedge coupler of height $2a_y$, we did not consider other values of height for the optimization.

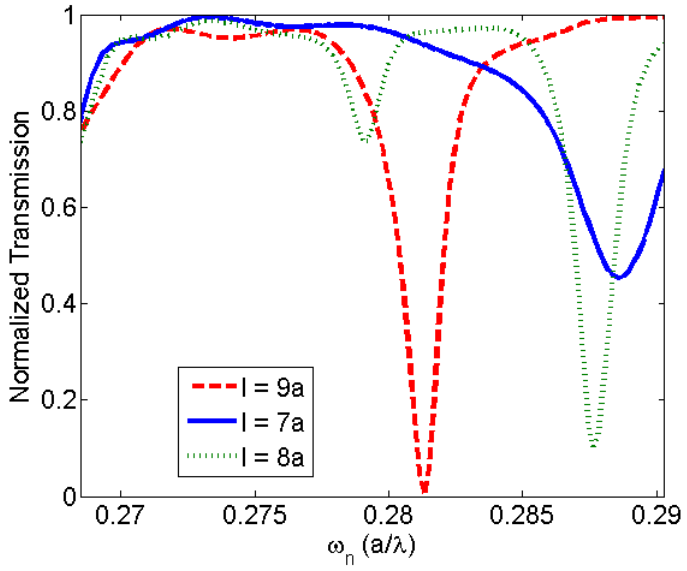

Figure 36: Normalized transmission for air wedge couplers with three different lengths (l): l = 7a (blue solid curve), l = 8a (green dotted curve), and l = 9a (red dashed curve).

For the effect of length (l) on the transmission properties of air wedge coupler, we kept the height fixed at $2a_y$ and varied the length. Figure 36 shows the transmission through air wedge couplers for three different lengths: l = $7a$ (blue solid curve), $l = 8a$ (green dotted curve), and $l = 9a$ (red dashed curve). We see Fabry-Perot dips in the response and the dips move as we change the length of the coupler. For some length, one of these Fabry-Perot dips can fall in the low group velocity frequency range and decrease the transmission that is the case when we go from length $7a$ to $9a$. For the three lengths shown in the figure, we can get 100% transmission in the whole single mode frequency range of the PCW. The region for

100% transmission changes with different designs, as the Fabry-Perot dips move, and depending on the application we can choose one of the lengths. Since our present focus is on low group velocity modes of the PCW, the air wedge coupler with length $7a$ performs the best. For the air wedge coupler with length $7a$ we can get 100% transmission over a very broad range and the minimum transmission at the low group velocity edge (the low frequency edge of the graph) is around 80%.

6.3 Comparison of the Two Designs

In the previous two sections, we presented two designs for achieving good coupling from a slab waveguide to a PCW in the low group velocity region. The taper coupler design was based on coupling the slab modes to high group velocity modes of the PCW and then adiabatically transforming the high group velocity modes into the low group velocity modes of the PCW. Whereas, for the air wedge coupler, we adiabatically transform the mode of the slab waveguide into the PCW mode; we start from the small values for the evanescent field and move towards larger field values until we reached the middle slab region and the slab waveguide has been converted into a PC waveguide. The two designs are compared in Figure 37(a). Also shown on the same plot is the transmission response from a butt coupled PCW.

The final taper coupler design (shown in the figure with red dashed curve) has a flatter response with low magnitude transmission dips. The transmission is close to 95% throughout most of frequency range of interest and reaches a minimum of around 77% at the mode edge. The air wedge coupler, on the other hand, has close to 100% transmission in a smaller range but throughout the low group region it has better transmission than the taper coupler. The minimum transmission in the low group velocity range is around 80%. The air wedge coupler, however, is more sensitive to Fabry-Perot effects with bigger transmission dip. The air wedge coupler

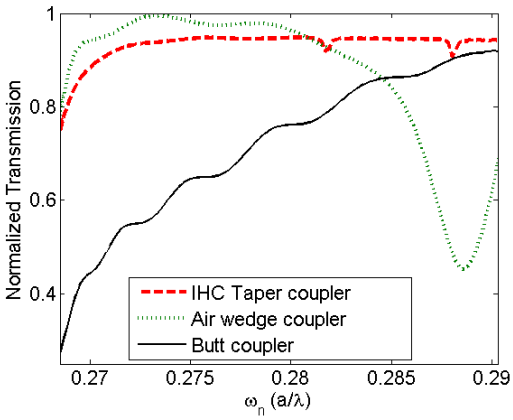

Figure 37: (a) Comparison of normalized transmission of the two designs: taper coupler (red dashed curve) and air wedge coupler (green dotted curve) with the butt coupler (black solid curve).

is also more sensitive to the effective index of the mode, which apart from other factors also depends on the thickness of the Si slab. Thus, based on the bandwidth requirement of the application either of the two designs can be used. For applications involving use of all the single mode guiding bandwidth we can use a tapered coupler, and for applications targeting only the slow group velocity region we can use the air wedge coupler, which allows us to get up to 100% transmission into the PCW.

6.4 Fabrication

Motivated by the simulation results, we proceeded towards fabricating our structures. The details of our fabrication process can be seen in Chapter 3. Briefly, we defined our patterns in the dw-2000 software bought from Design Workshop Technologies. The patterns were transferred to the e-beam resist (ZEP) on SOI samples using the e-beam lithography system. After developing, the patterns were transferred to the Si device layer using anisotropic dry etching in a Cl_2 plasma. After etching, the remaining resist is removed using piranha or an O_2 plasma. We then used photolithography to selectively remove the BOX (buried oxide) layer from

underneath the PC patterns. A BOE (buffered oxide etch) solution was used to remove the buried oxide layer. The BOX layer is removed to allow more bandwidth below the light line for the PCW modes. The remaining PR (photoresist) is then removed using an O_2 plasma. The photoresist can not be removed using wet etching after the undercutting, as wet etching of resist results in debris on the PCW region, which is difficult to remove, and also at times this wet etching results in breaking the access ridge waveguides. When we undercut our PCW structure, BOX underneath parts of the access ridge waveguides closer to the PCW region is also removed; rendering these access ridge waveguides fragile and likely to break when immersed in liquids. SEM images of some of the fabricated structures are shown in Figure 38.

As mentioned in the Section 6.2.1, there are two ways of implementing the tapers: (i) by keeping the period constant and tapering the air hole radius, or (ii) by keeping the air hole radius fixed and tapering the period. Although we have mostly mentioned air hole tapered couplers in that section, we also fabricated the period taper couplers, since e-beam lithography allows a lot more accuracy in the position of the air holes rather than their size. These images show input and output ridge waveguides coupled to the PCWs using the different coupler designs as mentioned in the Section 6.2. These ridge waveguides are used to route light from/to the input/output facet of the chip to/from the PCW. Figure 38 shows the SEM image of the fabricated butt coupled PCW in (a), the air wedge coupler in (b), the air hole taper coupler in (c), and the period taper coupler in (d).

6.5 Characterization

The fabricated samples were characterized using our swept wavelength setup. The details of the characterization setup can be seen in Section 5.5 of Chapter 5. Exact characterization of PCWs is challenging, as there are three loss factors that affect

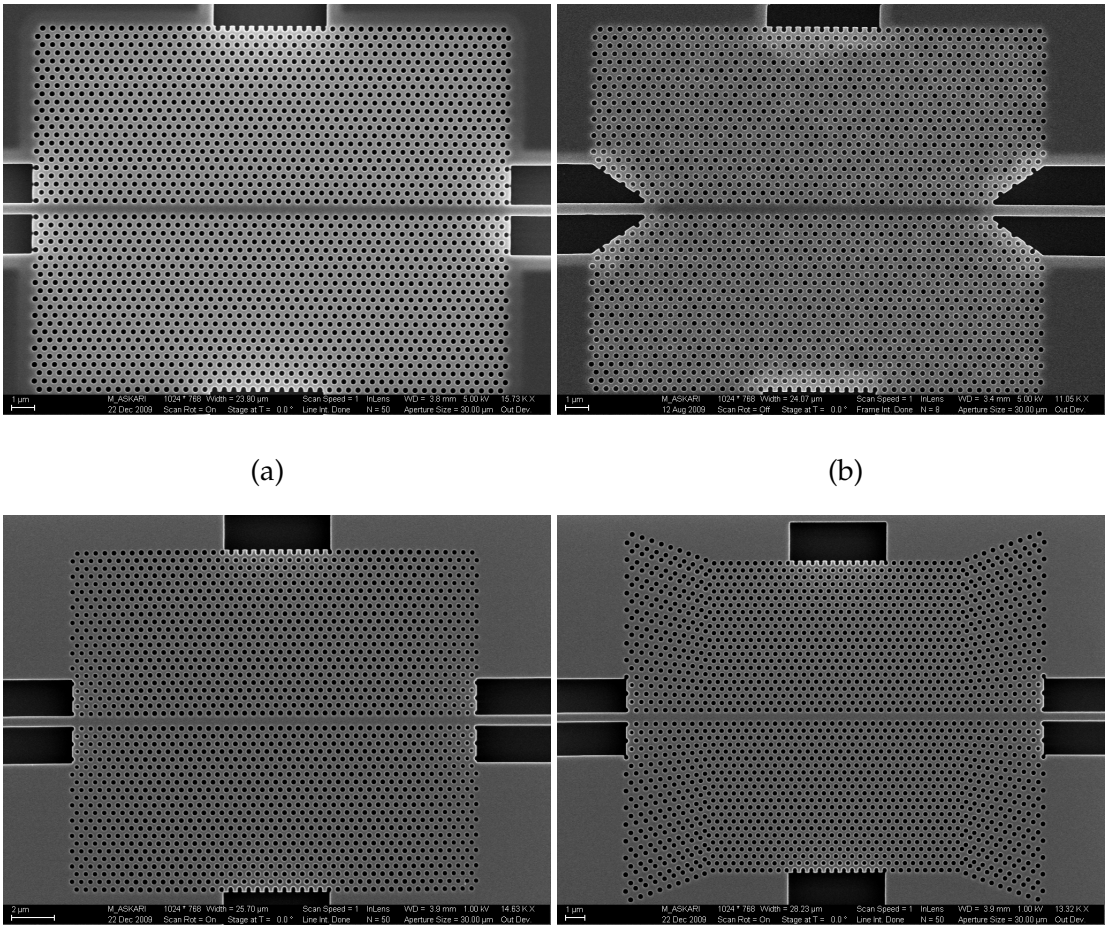

(a) (b)

(c) (d)

Figure 38: SEM images of fabricated structures [3]: (a) butt coupled PCW, (b) air wedge coupler, and two realizations of taper coupler (c) air hole taper coupler, and (d) period taper coupler. The length of PCW in each case is $50a$.

the transmission and it is almost impossible to decouple them [3]. The three loss factors that affect the transmission are following.

i) Low coupling efficiencies at low group velocities.

ii) Propagation loss increases with decreasing group velocities.

iii) Radiation loss due to modes above the light line.

Of the three factors mentioned above, the first two manifest in low transmission at low group velocities and the third lowers the transmission at high group velocities.

To get the exact coupling coefficient as a function of group velocity, we need to decouple all three effects. Keeping these challenges in mind, we have devised the following strategy to get a measure of coupling loss at low group velocities. For each coupler, we had patterns with three different lengths of the PCW: 50a, 100a and 150a on the same chip. Since the propagation losses are minimum for PCWs with smallest length (50a in our case), these patterns were used to characterize the coupling response. However, since there is a chance for some energy below the mode edge $\omega_n < 0.267$ to tunnel though to the output ridge waveguide for short lengths of the PCW, the patterns with 100a and 150a long PCWs were used to find the edge of the even (fundamental) mode of the PCW. The characterization data for the 50a long PCW is then used to calculate the coupler response in the frequency range as obtained from patterns with longer PCWs. As mentioned in Section 6.1, the simulation results were optimized with 2D-FDTD simulations with a fixed $n_{eff} = 2.811$. However, in practice, n_{eff} is not constant and changes with frequency. Also, the thickness of device layer of an SOI wafer can change from wafer to wafer and within a 4-inch wafer. Hence, the results optimized through simulations may not be the optimum results for actual fabricated devices. To find the optimum parameter values for the fabricated devices, we varied the optimization parameters of each coupler design around the values obtained through simulations (mentioned in Section 6.2). For example, for an air wedge coupler we used three values for the length of the air wedge region (6a, 7a and 8a). Since the taper coupler has two parameters (initial r/a and the length of taper) to optimize and we have two ways of tapering (air hole taper and period taper), we used an air hole taper coupler to optimize for the length of the taper region and a period taper coupler to optimize for the initial r/a. Hence, for the air hole taper coupler we fixed the initial r/a at 0.25 (obtained from simulation results) and used three values of taper length (7a, 8a and 9a). For the period taper coupler, we fixed the length of the taper to 9a (obtained

from the simulation results) and used three different values of initial r/a: 0.23, 0.24, and 0.25. Since the laser output is not constant with frequency, all the transmission spectra were normalized with respect to the transmission spectra through a ridge waveguide. The underlying assumption is that the losses in a ridge waveguide are wavelength independent. Figure 39 shows the characterization results for some of the fabricated couplers.

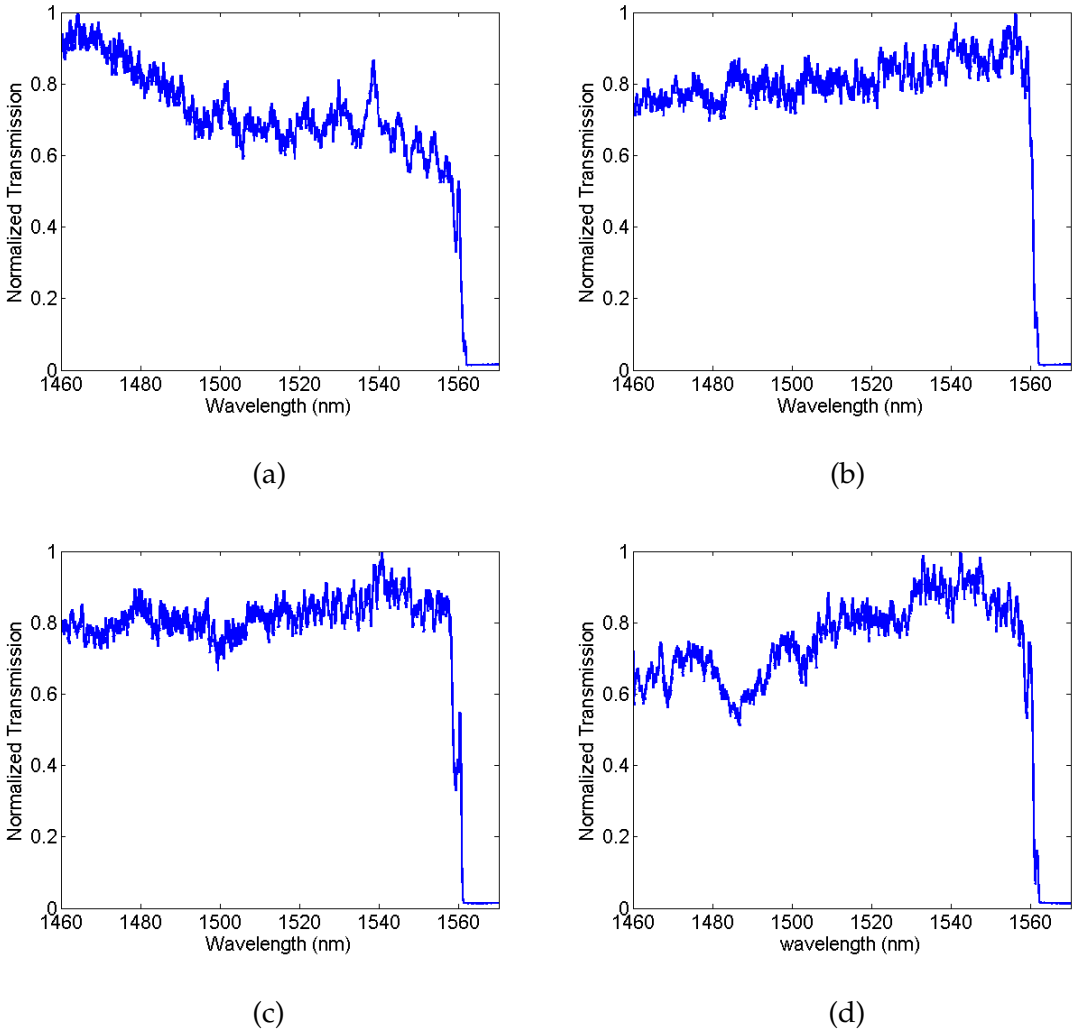

Figure 39: Characterization results of some of the fabricated couplers: (a) butt coupler, (b) air wedge coupler with length $7a$, (c) air hole taper coupler with length $9a$ and initial $r/a = 0.25$, and (d) period taper coupler with length initial $r/a = 0.24$ and length being 9 tapered periods. In each case the total length of the PCW was $50a$.

The characterized results are then used to calculate the ratio of average transmission at low group velocities to average transmission at high group velocities [3], where the low group velocity region is considered to be the last 20 nm of the transmission window close to the mode edge. The chosen low group velocity region of 20 nm corresponds to group indexes of 10 or more. For the results shown in Figure 39, the low group velocity region is from 1540 nm – 1560 nm. The high group velocity region, which was used to calculate the average transmission at high group velocities, is taken to be from 1460 nm – 1480 nm. There are a couple of things to note in the figure. First, for the three designed couplers the average transmission at low group velocities is larger than at high group velocities. This higher average transmission at low group velocities is due to radiation losses associated with high group velocity modes being above the light line. In simulations, we did not see the lower transmission at high group velocities effect, as we had used 2D-FDTD. Second, only in the last half of the low group velocity window do we see the transmission for the taper couplers (both air hole and period) to drop off as we approach slower and slower group velocities. Third, for the air wedge coupler a similar drop in transmission with decreasing group velocities is seen only in the last 4 nm. These two (second and third) observations agree well with the simulation result shown in Figure 37(a), where we see the transmission drop for $\omega_n l 0.27$. Fourth, for the butt coupled PCW (shown in Figure 39(a)) the transmission drops as we go to larger and larger wavelengths (lower and lower frequencies), and this observation also agrees very well with the simulation result in Figure 37. Fifth, for the period taper coupler we see a fairly strong transmission dip close to the high group velocity window. This dip may be due to the Fabry-Perot effect. Although, we do not see similar dips in the transmission spectra for the air wedge coupler or the air hole taper coupler for this sample, we see similar dips in all the couplers for different fabrications. These dips vary in position and intensity from

fabrication to fabrication, possibly due to changes in the device layer thickness from wafer to wafer and within a wafer. The company (Soitec, from where we buy our SOI wafers) quoted a six sigma value of change in the device layer thickness of $\sim$ 20 nm. Thus, characterization results from one round of fabrication can not be considered final. To have a better confidence level for our results, we fabricated four sets of samples and characterized them. The statistical averages of these four fabricated samples for each of the coupler are quoted in the Table 5.

Table 5: Statistical average of the ratio of average transmissions at low and high group velocities for different couplers [3].

No.	**Pattern Name, length, initial r/a**	**Statistical average of ratio of average transmissions at low and high group velocities**
1	Butt, – , –	0.61
2	Air wedge, 6a, –	0.94
3	Air wedge, 7a, –	1.03
4	Air wedge, 8a, –	0.98
5	Period taper, 9a, 0.23	1.07
6	Period taper, 9a, 0.24	1.12
7	Period taper, 9a, 0.25	0.98
8	Air hole taper, 7a, 0.25	0.85
9	Air hole taper, 8a, 0.25	0.92
10	Air hole taper, 9a, 0.25	0.9

From the table, it is evident that all of our designed couplers perform much better than the butt coupler. Of the three designs, air hole taper couplers provided the least performance improvement as compared to the butt coupler. The minimum improvement in transmission is 24% for a coupler with length 7a. For an air hole taper coupler, we had kept the initial r/a fixed at 0.25 and varied the length. Similar performances are obtained for couplers with length 8a and 9a, as shown in Table 5, with the statistical average of ratios (of average transmission at low group velocities to average transmission at high group velocities) being 0.92 and 0.90 respectively. For the air wedge coupler the best performance is obtained for a coupler of length 7a, same as the one found in our simulations, where this ratio

is 1.03. As mentioned above, a number greater than one is due to radiation losses for high group velocities modes that lie above the light line. The ratio of average transmissions at low and high group velocities for air wedge couplers of length $6a$ and $8a$ is 0.94 and 0.98 respectively. Even the worst of the air wedge couplers (air coupler of length $6a$) performs 33% better than the butt coupler at low group velocities. The best performance of all the couplers is obtained for the period taper coupler; the best performance being obtained for a period taper coupler of initial r/a = 0.24, with the ratio being equal to 1.12. The lengths of all the period taper couplers were kept fixed at $9a$. The ratio of average transmissions at low and high group velocities for other period taper couplers with initial r/a values of 0.23 and 0.25 was 1.07 and 0.98 respectively. The performance difference between the period taper and air hole taper couplers is probably due to better air hole placement accuracy of the e-beam lithography system. With e-beam lithography system there is much less control over the size of air holes. We have seen a variation of over 30 nm in the diameter of air holes from fabrication to fabrication. Even for a single fabrication the size of air holes is not constant and depends on the location of air hole with respect to other air holes. An isolated air hole requires more dose than an air hole in the center of the PC due to forward and backward scattering of electron beam.

Table 5 compares the transmission into low group velocity modes of the PCW relative to the transmission at high group velocity modes for each coupler. It does not show the exact enhancement in coupling over the butt coupler. For example, the table does not compare how much enhancement in transmission will we achieve by using one of our designed couplers over a butt coupler in the high group velocity region. To obtain this information we fabricated another sample consisting of ridge waveguide y-junctions. The idea was to put butt coupled PCWs

in one arm of the y-junctions and our designed couplers in the other arm and monitor the power output. Higher output power would imply better coupling [3]. The length of the PCWs in both arms of the y-junctions was 50a. Rather than fabricating all nine couplers (three coupler types with three configuration for each coupler), we only fabricated one for each type of coupler. For each coupler type we chose the parameters (length, initial r/a) that resulted in best performance, shown in Table 5. So for an air wedge coupler we chose the coupler with length 7a; for the air hole taper, 8a and initial r/a = 0.25; and for the period taper coupler, 9a and initial r/a = 0.24. The output intensities from the two arms, of each y-junction, were captured by an IR (infrared) camera. The intensities were recorded in 0.5 nm spacings for the first 5 nm of the transmission window (1460 – 1465 nm), i.e., in the high group velocity region. These intensities were then averaged and used to calculate the enhancement in efficiency as compared to a butt coupler. The efficiency enhancement is calculated by taking the ratio of average power output from the arm containing the designed coupler ($P_{out}^{Coupler}$) to the output power from the arm containing the butt coupler ($P_{out}^{Butt\ coupler}$) and is reported in Table 6.

Table 6: Ratio of output powers from the two arms of y-junction; one arm contains a butt coupled PCW and the other arm contains one of the designed couplers. The length of PCW in both the arms is 50a.

Coupler Name	**Efficiency improvement ($P_{out}^{Coupler}$/ $P_{out}^{Butt\ coupler}$)**
Air wedge coupler	1.1053
Air hole taper	1.0913
Period taper	1.1149

The table shows that all of our designed couplers show enhanced performance over a butt coupler. The performance for period taper and air wedge couplers is similar with 11% higher output power than the butt coupler. 11% higher output power would imply 5.5% better coupling per facet. For an air hole taper coupler

the output power is 9% greater than the butt coupler: a 4.5% better coupling performance than the butt coupler.

Based on the results mentioned in Tables 5 and 6, we get upto 5.5 % better transmission into high group velocity modes of the PCW using our designed couplers. At low group velocities the coupling efficiency is even higher. In using the data from Table 5 to calculate the exact coupling improvement over a butt coupler at low group velocities, we need to factor in the improvements at high group velocities as shown in Table 6. For each coupler we have to subtract the value given in column three of Table 5, half it (as there are two couplers per device) and then add half the improvement shown in Table 6. Thus, for an air wedge coupler of length $7a$ the improvement in coupling efficiency, at low group velocities, over a butt coupler is 26.5%. For the air hole taper coupler this improvement is 20%, and for the period taper, 31%. That is, we can couple 31 % more light into low group velocity modes of the PCW when we use period taper coupler rather than a butt coupler.

CHAPTER VII

ADIABATIC PERFECTLY MATCHED LAYERS FOR FDTD SIMULATION OF PCWS

Understanding and utilizing the unique properties of PCs require accurate simulation of these structures. The most commonly used simulation tools in the PC community are the plane-wave expansion (PWE) method and the finite-difference time-domain (FDTD) method. In a way, these methods complement each other; i.e, information obtained from these methods is different and usually complements one another. The FDTD [18] method, for example, has been widely used to obtain the wideband frequency response of PC structures for investigating the propagation of electromagnetic (EM) waves. For FDTD simulations, absorbing boundary conditions, for example Berenger's perfectly matched layer (PML) [10], are used to terminate the structures to simulate the infinite extent of the structure and eliminate spurious reflections from the boundaries of the simulation domain. Despite the wide spread use of the FDTD technique for the analysis and design of PC structures, its application to simulate PCWs presents unique challenges. The reflections from such a PML can be on the order of 20-30% in amplitude [70]. These reflections result in interference that compromises the accuracy of the simulation results.

Mekis et al. [80] showed that the reflection from the PCW-homogeneous PML (Berenger) interface is due to the k-mismatch. They showed that by reducing the k-mismatch using a distributed Bragg reflector (DBR) waveguide inside the PML, the amplitude reflection from the PML can be reduced to 3-5 percent [80]. Since a DBR waveguide can provide zero k-mismatch for only a single k value, Koshiba et al. [9] proposed using a PCPML by extending the PCW inside the PML; the

EM waves at the PCW-PCPML interface would be k-matched and would result in much lower reflection. Although the use of PCPML reduces the reflection to -30 dB level and below for high group velocity modes, the reflection at low group velocities remains at the same level (around -15 dB) as that for the Berenger's PML or the k-matched DBR waveguide PML. Thus, a new type of PML was needed for the investigation of PCWs at low group velocity regions. The need to have an absorbing boundary condition that performs well at low group velocities becomes even more important when we consider that most applications of PCWs target the low group velocity region and seldom are PCWs used in the high group velocity regime. Since the focus of my research was to utilize the low group velocity modes of PCW for making efficient devices, I also looked into this problem as part of my research. In this part of my research, I showed that by adiabatically matching the low group velocity modes of a PCW to large group velocity modes of the PML, the reflection from the PML can be reduced to -30 dB or below. In this chapter, I will present the approach we have taken to reduce the reflections from the PML at low group velocities. Again, as with other chapters of this thesis, I have written this chapter as a self contained document. I will first briefly discuss the simulation platform. I will then describe why the PCPML approach does not work well for low group velocity modes, and then I will provide details of our approach to solve this issue of large reflections from the PML for low group velocity modes of a PCW impinging on the PCW-PML interface.

7.1 Simulation Platform

The structure we have used in our simulations is shown in Figure 40. It consists of a dielectric slab waveguide connected to a PCW. The PCW is formed by removing one row of air holes in the ΓJ direction of a triangular lattice PC of air holes in silicon (n_{eff} = 2.811). The width of the slab waveguide is chosen to be the same as

that of the PCW and is shown in Figure 40 as d. The radius of the air holes, r, is 30% of the lattice period, a. To analyze the structure, we use the two dimensional (2D) FDTD technique. To take the finite thickness of the structure into account, we use the effective index technique as explained in Ref. [72]. We also employ perfectly matched layers (PMLs) around the structure at all boundaries. The lattice period is taken to be equal to 24 grid points in our FDTD grid.

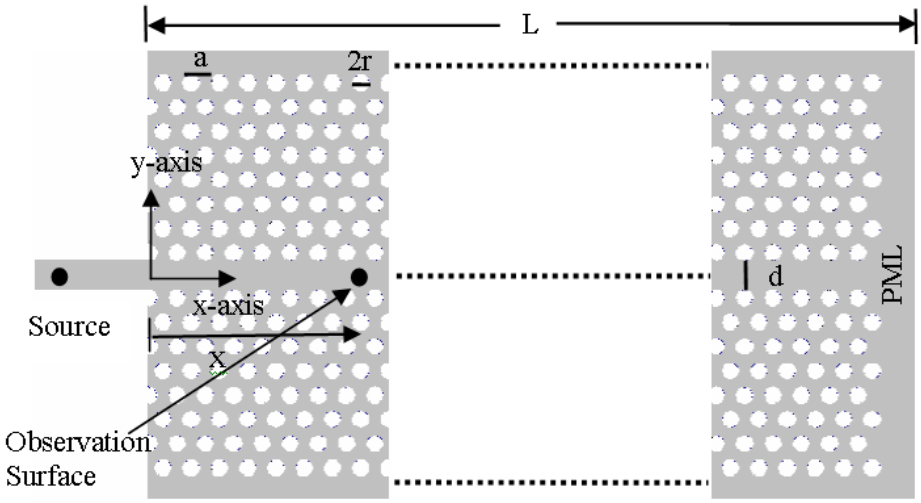

Figure 40: Structure used in our simulations showing the location of the source and the observation surface. The PC structure is formed by a triangular lattice of air holes in Si. The radius of each hole, *r*, is 30% of the lattice constant, *a*. The PCW is formed by removing one row of air holes. The origin of the co-ordinate system is in the middle of the slab at the slab-PCW interface. The observation surface is at a distance x from the slab-PCW interface.

To calculate the power reflection spectrum (reflection coefficient verses frequency) from the PML, we have used a pulsed Huygens source [62] to excite the fundamental TM mode (i.e. magnetic field normal to the plane of the periodicity of the PC) in the slab waveguide. The bandwidth of the pulse is chosen to cover the complete single mode region of the PCW. The PCW has one TM even (fundamental) mode and one TM odd mode in the PBG as shown in Figure 41. The single mode region is the frequency range ($0.2668 \leq \omega_n \leq 0.29$) of the even mode below the odd mode. To calculate the reflection spectrum, the time fields are recorded at

the observation surface. The incident/reflected power spectrum is calculated from the Fourier transform of the fields. The spectrum of the power reflection coefficient ($\Gamma(\omega)$) is then calculated as the ratio of the reflected power to the incident power ($\Gamma(\omega) = P_{x,ref}(\omega)/P_{x,inc}(\omega)$).

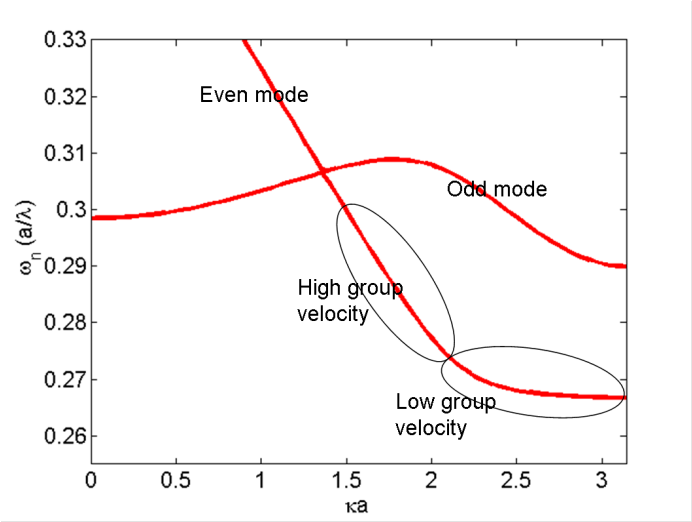

Figure 41: Dispersion diagram for TM modes (i.e. magnetic field normal to the plane of periodicity) of the PCW. Also indicated in the figure are even and odd modes of the PCW, as well as the high and low group velocity regions of the even mode.

7.2 Location of Observation Surface

The calculation of reflection coefficient requires caution when operating at low group velocity frequencies, where there is large group velocity dispersion (GVD). The large GVD causes different frequency components to arrive at the observation surface at different times. To ensure accuracy of results, it is important to separate — in the time domain — the reflected energy from the incident energy. To calculate the reflection coefficient, most researchers in the computational EM community use the center of the structure as the location of the observation surface. This location (center of the structure) of the observation surface — also used in Ref. [80, 9] — is not well suited for studying structures with large GVD, since the

maximum group velocity ratio for which the incident and reflected energy can be separated at the center of the structure is 3 and is length independent [73]. Let v_{g1} and v_{g2} be the two extreme group velocities contained in an impulse excitation of the PCW structure, i.e., $v_{g2} \leq v(\omega) \leq v_{g1}$. As shown in Figure 40, let the observation surface be at location x and the total length of the structure be L. Let t_2 be the time taken by the v_{g2} part of the incident pulse (traveling to the right in Figure 40 to reach the observation surface and t_1 be the time taken by v_{g1} part of the reflected pulse (traveling to the left after reflecting from the PCW-PML interface in Figure 40 to reach the observation surface. To separate the incident pulse from the reflected pulse at the observation surface, the relationship between the two times t_1 and t_2 is given by:

$$\begin{aligned} t_2 &< t_1 \\ \frac{x}{v_{g2}} &< \frac{2L-x}{v_{g1}} \\ \frac{v_{g1}}{v_{g2}} &< \frac{2L-x}{x} \end{aligned} \tag{48}$$

When $x = L/2$ as in Ref. [80, 9], Eq. 48 becomes:

$$\frac{v_{g1}}{v_{g2}} < 3. \tag{49}$$

Equation 49 clearly shows that irrespective of the total length of the structures, if the observation surface is at the center of the PCW structure ($x = L/2$), the maximum group velocity ratio that can be separated at the observation surface is 3.

If, however, we use $x = 10a$ and $L = 300a$ in Eq. 48, we get

$$\frac{v_{g1}}{v_{g2}} < 59. \tag{50}$$

Equation 50 shows that if we use a PCW of L = 300a with an observation surface placed at x = 10a, the maximum group velocity ratio that we can separate at the observation surface is 59. This group velocity ratio of 59 is more than what is used

in practical applications of PCWs. To make sure we get meaningful results, we find the incident field from a large reference PCW structure (L = 300a in Figure 40), where there is no overlap between the incident and the reflected pulses at the observation surface (at x = 10a). We record the incident field ($E_{y,inc}$, and $H_{z,inc}$) at this location. For the reflected field, we use smaller structures (e.g., L = 25a or 50a) with the observation surface at the same location (x = 10a) with respect to the slab-PCW interface and record the total electric field (E_{total}). The reflected electric field (E_{ref}) is then computed by:

$$E_{y,ref} = E_{y,total} - E_{y,inc}. \tag{51}$$

This can be done without any ambiguity since the $E_{y,inc}$ is the same in the two cases (large reference structure for $E_{y,inc}$ and small structure for $E_{y,total}$) as the structure to the left of the observation surface is the same in the two cases. To ensure that the effects of the interference due to multiple reflections present at the observation surface are not too drastic, we can average the reflected field over a number of simulations with different structure lengths (L in Figure 40). From our simulations we have found that with this approach the ripples we see in our reflection spectra are on the order of 2-3 dB only, which is insignificant when compared with -30 – 45 dB of reflection we observe.

7.3 Reasons for Failure of PCPML in Absorbing Low Group Velocity Modes

Using our simulation platform, as mentioned in Section 7.1, we simulated the performance of PCPML [9] in absorbing a pulse with a large GVD inside the PCW. The reflection from the PCPML is compared with Berenger's or homogeneous PML (HPML) in Figure 42, which shows that the PCPML works better than the HPML only at high group velocities ($\omega_n > 0.275$) and that the performance of the two PMLs is similar at low group velocities ($\omega_n \leq 0.275$) with less than a few dB better

performance for the PCPML [11]. Also note the difference in lengths of the PML (shown as a multiple of the lattice constant, a, in Figure 42), as we have used the same length of the PCPML as used in Ref. [9].

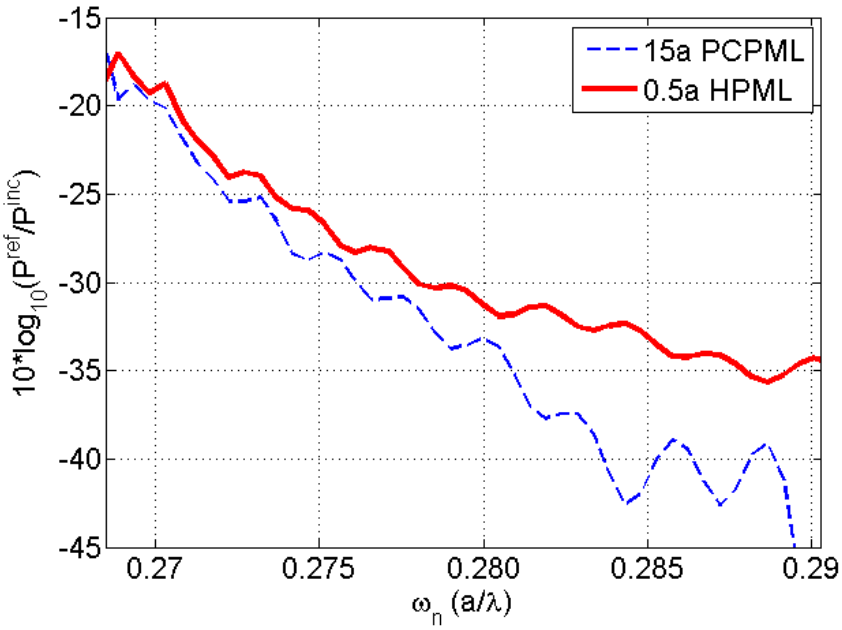

Figure 42: Comparison of reflection from a PCPML [9] (blue dashed) and an HPML [10] (red solid). The length of these PMLs are $15a$ and $0.5a$, respectively, with a being the lattice constant. All parameters of the PCW structure are the same as those in the caption of Figure 40.

The reason for this large reflection at low group velocities is primarily the k and group velocity mismatch between the PCW mode and the PCPML mode [73]. This fact becomes clear when we find the dispersion diagram of the PCW and the PCPML, which is modeled by a PCW with non-zero conductivity (σ). With $\sigma \neq 0$ the permittivity (ϵ) becomes a function of frequency (ω) and the dispersion diagram can not be computed with ω as the eigenvalue. Thus, the dispersion must be calculated with k as the eigenvalue [81]. Figure 43 plots the dispersion diagram of a PCW for two values of σ ($\sigma = 0$ and $\sigma = 0.03$). The figure shows that as soon as conductivity is added to the PCW, the dispersion changes drastically in the low group velocity regions of the dispersion diagram.

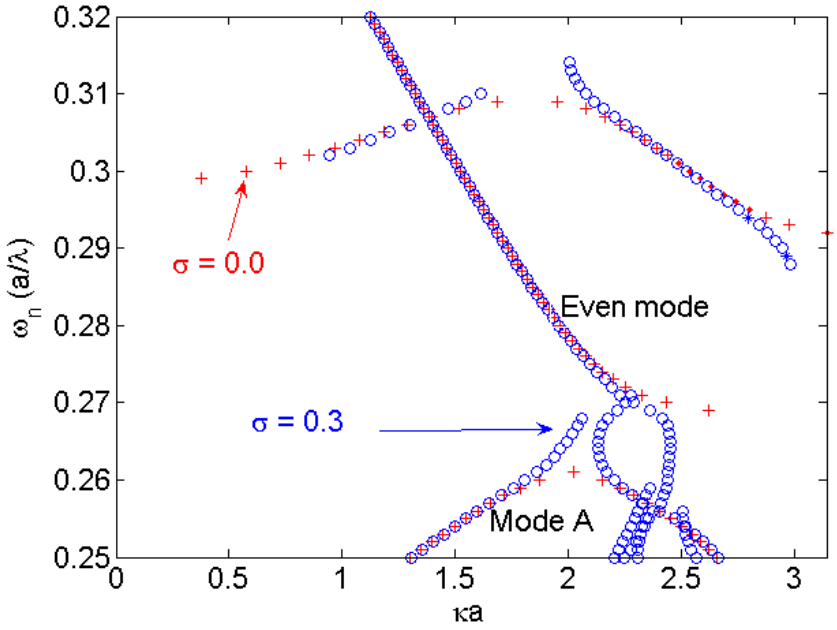

Figure 43: Dispersion diagram of the PCW of Figure 40 for different values of conductivity (σ). The curves shown have conductivity $\sigma = 0$ (red plus signs) and $\sigma = 0.03$ (blue circles). The modes of the two structures are almost the same for $\omega_n > 0.275$. However there is significant difference at $\omega_n < 0.275$, which corresponds to the low group velocity region.

The reason for the drastic change in the dispersion of the low group velocity region can be explained intuitively by considering that the zero group velocity points of the dispersion correspond to counter-propagating Floquet components of equal amplitudes that cancel one another. With $\sigma \neq 0$ the amplitudes of these counter-propagating Floquet components are no longer equal and hence, they do not cancel one another; as a result the slope of the dispersion changes in the low group velocity region of the dispersion. The effect of adding σ to the even mode dispersion is that the mode gap disappears and the even mode couples with the mode (mode A in Figure 43) lying below it. This coupling results in a drastic change in the dispersion of the low group velocity region of the even mode resulting in a large group velocity mismatch as well as a large k mismatch between the modes of the PCW and the PCPML (i.e., PCW with $\sigma \neq 0$). The field profile of mode A, shown in

Figure 44, has the same parity as the even mode, allowing it to couple to the even mode of the PCW and thus causing it to bend downwards.

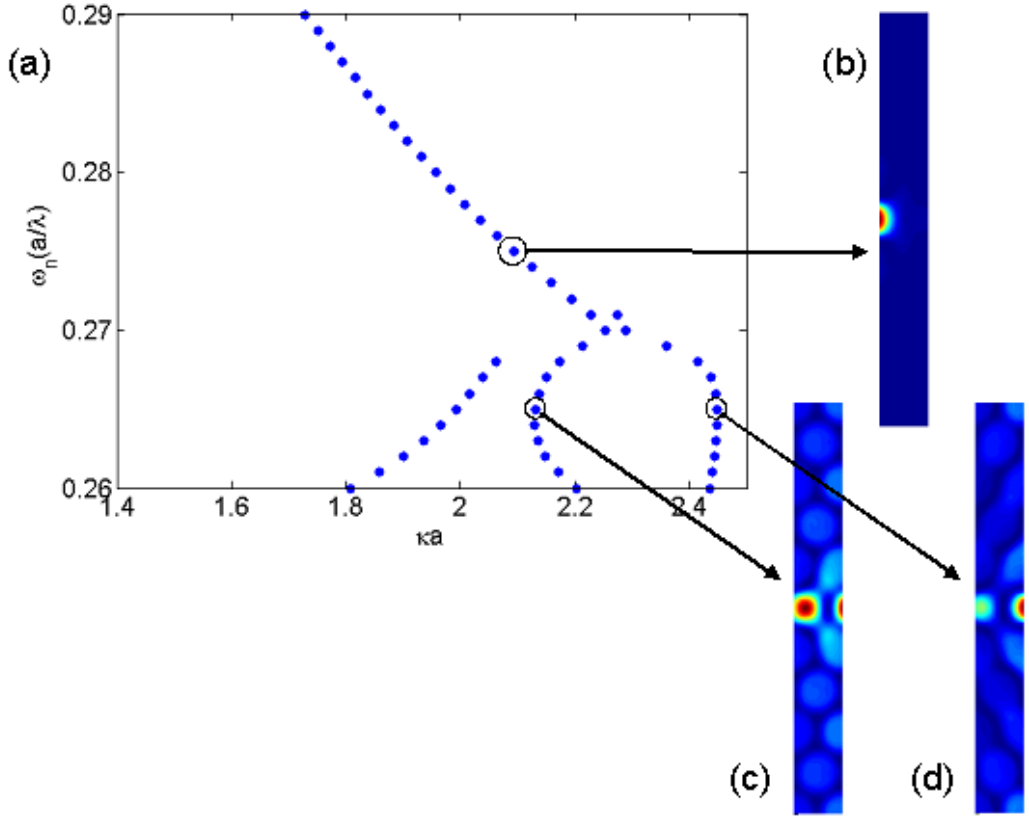

Figure 44: (a) Dispersion diagram of a PCW with $\sigma = 0.03$. The field profiles are calculated at (b) $\kappa a = 2.0942$ and $\omega_n = 0.275$, (c) $\kappa a = 2.138$ and $\omega_n = 0.266$, and (d) $\kappa a = 2.447$ and $\omega_n = 0.266$. All parameters of the PCW are the same as in Figure 40.

7.4 Adiabatically Matched PCPML and Discussion

Figure 43, in addition to providing the reason for large reflections at low group velocities for the PCPML, also provides the reason for the good performance of the PCPML at high group velocities. The dispersion for the linear part of the even mode (i.e., the high group velocity region ($\omega_n > 0.275$)), in Figure 43, does not change when conductivity is added. This results in a good group velocity and k match between the modes of the PCW and the PCPML over a large bandwidth

resulting in reduced reflections as compared to the homogeneous PML and the DBR waveguide PML [80] as shown in Ref. [9]. However, to reduce reflections at the low group velocity region ($\omega_n \leq 0.275$) a similar group velocity and k matching between the PCW and the PML region must be enforced.

Adiabatic matching has been used to reduce reflections from the interface between non-periodic structures and periodic structures [79, 82]. The same idea can be used to reduce reflections from the PCW-PCPML interface. Figure 45 shows the dispersion diagram of the PCW, in Figure 40, as a function of *r/a*. Figure 45 shows that the dispersion moves to lower frequencies as we reduce the radius of the air holes.

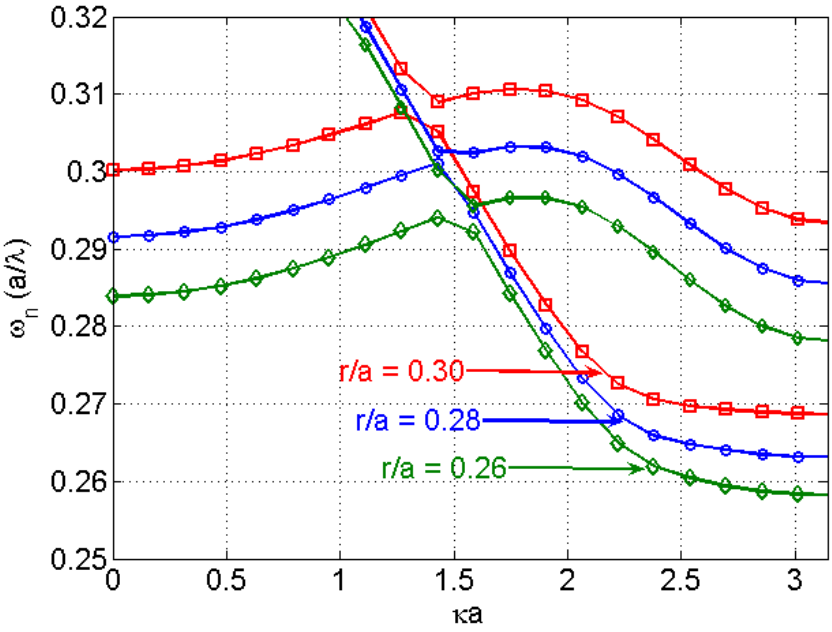

Figure 45: Dispersion of the PCW, in Figure 40, for different values of *r/a*: $r/a = 0.30$ (red squares), $r/a = 0.28$ (blue circles) and $r/a = 0.26$ (green diamonds).

The low group velocity modes of the PCW with r/a = 0.3 lie in the same frequency range as the the high group velocity modes of the PCW with r/a = 0.26. The low group velocity modes of the PCW with r/a = 0.3 can then be absorbed by adiabatically matching these modes to the large group velocity modes of a PCW

with r/a = 0.26 and then terminating the structure with a PCPML with r/a = 0.26. In this scheme that we call the adiabatically matched PCPML (AM-PCPML), the absorbing boundary consists of two regions as shown in Figure 46:

1) the adiabatic region in which r/a is adiabatically reduced from left to right, and

2) the PCPML region in which r/a is fixed.

In this scheme, the adiabatic (transition) region in Figure 46 matches the low group velocity modes of the PCW with a large *r/a* (e.g., *r/a* = 0.3) to high group velocity modes of a PCW with smaller *r/a* (e.g., *r/a* = 0.26). The second region is the PCPML region, with the smaller *r/a* (e.g., *r/a* = 0.26), which is used to absorb the incoming EM energy. The design of the first region is similar to the one presented in Ref. [79] and also explained in Chapter 6 of this thesis. The power reflected from such an AM-PCPML is compared with HPML and PCPML in Figure 47.

Figure 46: Simulation structure with adiabatically matched PCPML (AM-PCPML). The figure shows the adiabatic region, where the low group velocity modes of the PCW with *r/a* = 0.30 are matched to high group velocity modes of the PCW with an *r/a* = 0.26, and the PCPML (with *r/a* = 0.26) region.

The adiabatic region in our case consists of six periods of a PCW with *r/a* decreasing linearly from 0.3 to 0.26. The PCPML consists of three periods of PCW with *r/a* = 0.26. Figure 47(a) shows that the adiabatically matched PCPML performs much better than the PCPML in the low group velocity region ($\omega_n \leq 0.275$)

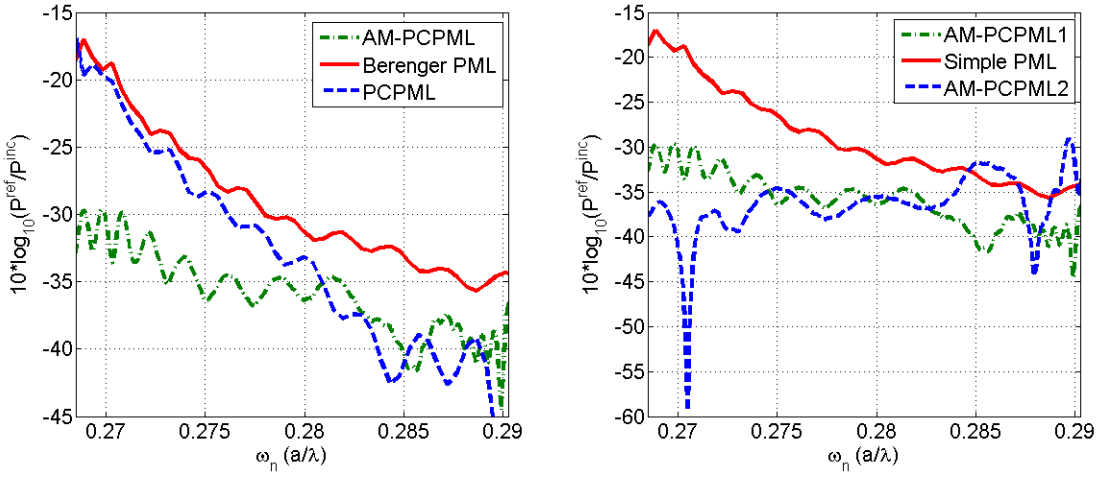

Figure 47: (a) Comparison of reflections from different PMLs: HPML (red-solid), PCPML (blue dashed) and adiabatically matched PCPML (green dash-dot) applied to the PCW shown in Figure 40. (b)Comparison of two variations of adiabatically matched PCPML: AM-PCPML1 (green dash-dot) and AM-PCPML2(blue dashed) [11].

and that the reflection is reduced by 13-16 dB in this region. The performance of the two PMLs in the high group velocity region ($\omega_n > 0.28$) is similar due to the similar dispersion characteristics of the two PMLs in this frequency range. We should also point out that the total length of the adiabatically matched PCPML, which includes the length of both the adiabatic region and the PCPML region, is $9a$, which is smaller than the length of PCPML ($15a$) reported in Ref. [9]. Thus, the adiabatically matched PCPML, as presented in this research, is a good choice in absorbing both high and low group velocity modes of a PCW.

The adiabatically matched PCPML presented in Figure 47(a) works better or similar than all other reported works [80, 9] in the single mode region of the PCW. If we consider only the low group velocity region then we can do even better. We ran a number of simulations varying the parameters (the final r/a, which continues in the PCPML region, and the length) of the adiabatic region of our designed adiabatically matched PCPML. We found that if we use a final r/a of 0.25 and a length of $9a$ for our adiabatic region, we get the best performance for our adiabatically

matched PCPML [11]. This is shown in Figure 47(b), where we are comparing the two adiabatically matched PCPMLs.

1) AM-PCPML1: with final r/a = 0.26 and length 6a.

2) AM-PCPML2: with final r/a = 0.25 and length 9a.

The figure shows clearly that AM-PCPML2 performs better than AM-PCPML1 in the low group velocity region with almost a 5 dB further reduction in the reflection. This AM-PCPML2 performs better than the PCPML by more than 18 dB. The two variations of adiabatically matched PCPML, presented in this chapter, can be utilized based on the application. For applications requiring simulations at just the low group velocities, AM-PCPML2 would be a better choice. Whereas, for applications involving either just the large group velocities or a combination of both large and low group velocities, AM-PCPML1 would be the better choice. Also note that this idea of adiabatically matched PCPML can be easily extended to any periodic structure exhibiting low group velocity modes or modes with large GVD. The main idea is to match the low group velocity modes of the periodic structure to the high group velocity modes of a similar structure before adding conductivity to the periodic structure for absorbing the incident EM energy.

In this part of research, we presented a new form of an absorbing boundary condition that performs optimally for absorbing both the low and high group velocity modes of a periodic electromagnetic structure (e.g., a PCW). The low reflection at low group velocities from the presented adiabatically matched PCPML is achieved by adiabatically converting the dispersive and low group velocity mode of the periodic structure to a high group velocity mode of a similar periodic structure before applying conductivity to the periodic structure. We showed that the reflection from the adiabatically matched PCPML for waves incident from a PCW structure

at the low group velocity region is 18 dB lower than the best results reported earlier (using other ideas to implement the PML) while having similar performance at the high group velocity region. This idea of adiabatically matched PCPML can be extended to simulate any structure that exhibits dispersive behavior with both low and high group velocity regions.

CHAPTER VIII

REFRACTIVE INDEX SENSING USING SLOW LIGHT IN PHOTONIC CRYSTAL WAVEGUIDES

Photonic Crystals (PCs) have generated much interest due to their unique properties. Of special research interest have been two dimensional (2D) PCs, which can be manufactured with mature semiconductor fabrication processes. By introducing defects in perfect PCs, cavities and waveguides can be obtained, which form building blocks for an integrated optics platform. PC waveguides (PCWs) allow unprecedented control for light guiding by allowing low-loss, ultra-compact bends [75] that can be very useful for designing very compact photonic structures. Another important property of light in these PCWs is the existence of low group velocity modes, which are not possible in waveguides with continuous translational symmetry. These low group velocity modes have allowed demonstration of on-chip slow light [53, 57], high efficiency Raman amplification [38], and compact thermo-optic switch [39].

One of the application areas for PCs is compact biological/chemical sensing. Optics based biological/chemical sensors operate by detecting a change in refractive index (RI) or absorption of light. PC-based devices hold promise to be more compact as they use band gap rather than index contrast to confine light. Most of the optical sensors (based on detecting the RI change) demonstrated to date are based on resonance shift [83, 84, 85]. The sensitivity of these devices is a function of line width of the resonance. The maximum detectable shift, on the other hand, is governed by the free spectral range (FSR). Since the line width and FSR are related, therefore the sensitivity and the maximum detectable range of these sensors

are also related. In this chapter, I present our design of a PCW-based RI sensor. I show that by using PCWs in their low group velocity regime we can achieve a compact sensor that overcomes this inherent interdependency of sensitivity and maximum detectable range of resonance-based sensors. I also compare the performance of a PCW-based sensor to that of a ridge waveguide based sensor and show that a factor of eight enhanced sensitivity can be obtained by using PCWs as the sensing element.

8.1 Simulation and Theoretical Analysis

A Mach-Zahnder interferometer (MZI) measures the phase difference between its two arms. By placing a material with unknown RI in one of its arms, this phase difference can be used to measure the RI of that material. Figure 48 shows a schematic of an MZI used to calculate the RI of a material. The phase difference in the two arm is given by:

$$\Delta\phi = (n_1 - n_2)k_o L = (k_1 - k_2)L = \Delta k L. \tag{52}$$

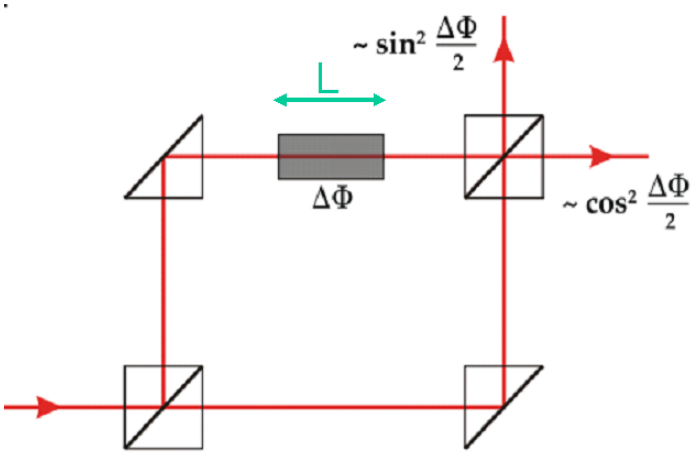

Figure 48: A schematic of MZI for determining the RI of an unknown material.

Using Eq. 52, we can find the RI of the material of a given length, L. In our research, we chose to use PCWs in the two arms of an MZI. With one arm infiltrated with

a liquid with an unknown RI, we can calculate the RI of the liquid by measuring the phase shift obtained at the output. For ease of detection, we decided to use an unbalanced version of MZI. In an unbalanced MZI the two arms are not of equal length. The unequal lengths of the two arms result in spectral fringes as a function of frequency. This can be seen by writing Eq. 52 as [86]:

$$\Delta\phi = k\Delta L = \frac{\omega}{c}\Delta L \tag{53}$$

$$\begin{aligned}\frac{\partial\Delta\phi}{\partial\omega} &= \frac{\partial k}{\partial\omega}\Delta L \\ &= \frac{n_g}{c}\Delta L\end{aligned} \tag{54}$$

Equation 53 shows that for an unbalanced MZI, with ΔL path difference between the two arms, the phase difference will be a function of frequency. As a result, we will get spectral fringes as a function of frequency [12]. In this case, any change in RI in one of the arms will result in a shift in the spectral fringes. This shift in spectral fringes is a lot easier to detect than a corresponding change in output intensity, which will be the case for a balanced MZI as shown in Figure 48. Another important thing to note is that in this architecture of an unbalanced MZI, the period of the spectral fringes can be controlled by controlling the path difference (ΔL) between the two arms. Thus, in this architecture the maximum detectable RI change, which depends on the period of spectral fringes, is independent of the sensitivity to the change in RI [12]. This is usually not the case in resonance-based sensing architectures where the resonance line width and the FSR are related. In waveguide-based sensors the fringe shift/RIU (RI unit) is directly proportional to the interaction length of the device. This again, is an added advantage of using this architecture as compared to a resonance-based architecture, where the interaction volume (and hence the resonance shift/RIU) can not be changed without changing the resonance line shape and the FSR. Thus, this architecture allows independent control of all three factors; i.e. sensitivity, spectral shift/RIU, and the maximum

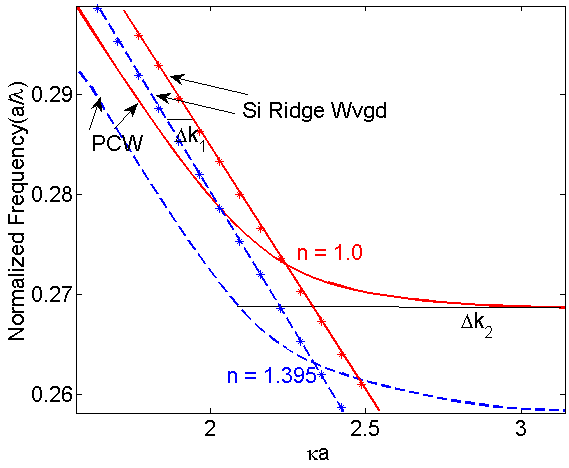

Figure 49: Dispersion diagram of a PCW (without asterisks) and a ridge waveguide (with asterisks) for two different values of hole/cladding RI: n = 1.0 (red, solid) and n = 1.395 (blue, dashed). Δk_1 and Δk_2 represent the change in wavevector for the ridge waveguide and the PCW respectively.

detectable RI change [12].

Equation 52 also shows that a smaller device is needed to obtain the same phase shift if the Δk between the two arms is larger. This motivated us to use PCW as the sensing element in the MZI. PCWs, operating at low group velocities, offer much larger Δk as a function of frequency as compared to a simple ridge waveguide. Figure 49 compares the Δk available for a ridge waveguide and a PCW.

From Figure 49 it is evident that a much larger Δk is available when operating at low group velocities in a PCW; thus much smaller footprint is required to have a sensor of same performance when PCWs (operating at low group velocities) are used instead of ridge waveguides. The dispersion diagram of a PCW was obtained using a 2D plane-wave expansion code using a super-cell technique [17]. The dispersions for the ridge waveguide are obtained by solving the mode equations [87] for a symmetric slab waveguide with a silicon core and the cladding RI as given in Figure 49.

To quantify the reduction in size that is achievable by using PCWs rather than

ridge waveguides in the MZI configuration, we simulated the length of a PCW and a slab waveguide required to achieve a phase difference of $\pi/10$ for an RI change of 0.0001. To calculate the required length, we first generated the dispersions for both the PCW and the slab waveguide for two values of hole/cladding RI ($n = 1.2$ and $n = 1.2001$). The dispersion diagrams were used to calculate Δk as a function of frequency (ω). This Δk is then used to calculate the required length of the PCW and the slab waveguide for a total phase change of $\pi/10$ ($\Delta\phi = \pi/10$ in Eq. 52). The required length as a function of frequency (ω) is plotted in Figure 50.

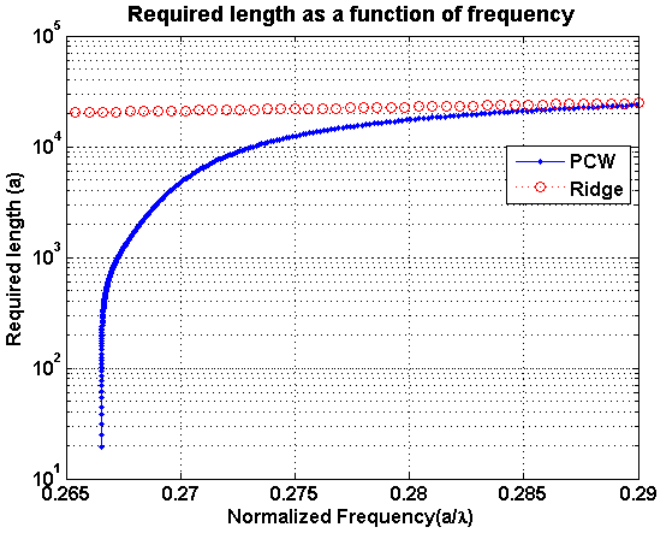

Figure 50: The required length of a PCW (blue solid line with dots) and a slab waveguide (red open circles) as a function of normalized frequency [12].

Figure 50 shows that the required length for a ridge waveguide is similar in most of the frequency range as the dispersion is negligible. On the other hand, for a PCW the required length changes from a value similar to what is required for a ridge waveguide to a value that is almost three orders of magnitude less [12]. This huge change in required length as a function of frequency for a PCW is due to the large dispersion available in PCWs. Thus, theoretically speaking, PCWs have the potential to reduce the size of a chemical/biological sensor by up to three orders of magnitude.

8.2 Fabrication and Experimental Characterization

One of the issues with using PCWs is the amount of loss associated with propagation at low group velocities. Due to this loss, it is not possible to probe the maximum group index available theoretically in a PCW due to large propagation loss associated with propagation at low group velocities. To find out what reduction in sensor size (i.e., what group index we can experimentally observe) is possible over a ridge waveguide based sensor, we fabricated PC and ridge waveguide-based RI sensors in an unbalanced MZI configuration. The difference in the two arms of the interferometer was chosen to be 105 μm. This path difference gave us a spectral fringe spacing of around 5 nm around 1550 nm [12]. This, somewhat arbitrary, choice of path difference was motivated by two factors:

i) to be able to probe different group indexes and

ii) to determine the sensing performance at different group indexes.

The sensor was fabricated using the procedure outlined in Chapter 3. An optical image of the fabricated device is shown in Fig 51.

There are a few of things to note in the optical microscope image of the fabricated structures.

a) In this architecture, the microfluidic channel runs perpendicular to the MZIs. This allows close packing of multiple sensors in a single microfluidic channel with the same liquid having access to multiple sensors. This architecture would be very useful for multiplex sensing and allows saving a lot of real estate on chip.

b) For PCW-based sensors, we have a PCW in both the arms of the unbalanced MZI. This is done to ensure we have similar coupling/propagation losses in

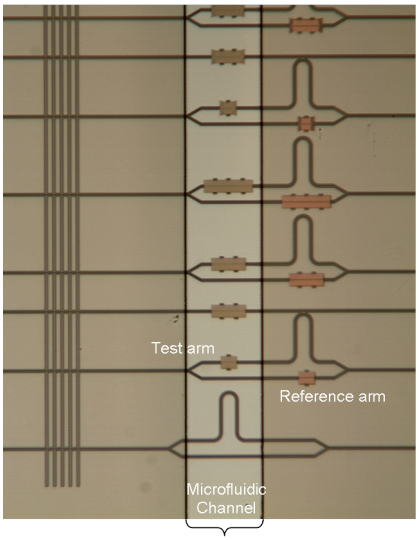

Figure 51: Optical microscope image of the fabricated RI sensor with multiple devices. The bottom most pattern is based on ridge waveguides whereas all others are based on PCWs with different lengths and ridge-to-PCW couplers [12].

the two arms so that the fringe contrast is not adversely affected by different amount of losses in the two arms.

c) Although we have PCWs in both the arms, only the PCWs in the test arms are exposed to the material. These are the PCWs that lie inside the microfluidic channel as shown in Figure 51.

d) The bottom most pattern with different lengths of ridge waveguides being exposed to the liquid in the two arms allows extracting the performance of a ridge waveguide based sensor.

e) Although some part of reference arm is also exposed to the fluid, but since the dispersions in the exposed region of the two arms is different, it is relatively straightforward to cancel the effect of ridge waveguide in the reference arm being exposed to the fluid. To do this, the bottom most pattern of the fabricated device, which has different lengths of ridge waveguide exposed to liquid, allows us to extract the behavior of the ridge waveguide and subtracts it for PCW-based structures.

f) For PCW-based sensors we fabricated two sets of sensors; one with simple butt coupling between the ridge and the PC waveguide and other with period taper couplers. This would allow us an independent verification of the coupler performance by comparing the group delays we can probe for different couplers. Also with better coupling into the PCW, we expect to get better fringe contrast and hence better sensor performance. The details of our designed period taper coupler can be found in Chapter 6 or in Ref. [79].

g) We also fabricated 100-period long PCWs coupled to ridge waveguides to study the shift in the mode edge due to different RI liquids and compare the performance of a PCW-based sensor that operates on a resonance shift principle, similar to one presented in Ref. [84], with our design.

We tested the fabricated devices with our swept-wavelength setup. For the details of the setup see Section 5.5 of Chapter 5. To test the performance of our fabricated devices, we have used certified refractive index oils from Cargille Labs. We decided to use oils with RI values 1.300, 1.305 and 1.31 as these values are close to the RI of water at IR wavelengths (1.318 at 1.55 μm and 25 ^{o}C) [88, 89]. For the ease of cleaning, we used SU-8 microfluidic channels and did not cap/seal these with PDMS on top. The thickness of our SU-8 microfluidic channel was around 2 μm. To make sure the oil goes through all the holes in the PCW we would wait 30 minutes before characterizing our samples. Recording data at different time intervals after dispensing the oil, we found that 30 minutes is more than enough for oil to completely infiltrate the holes. The sample was cleaned using 1,1,1-Trichloroethane, Acetone and Isopropanol (IPA) after recording data with each RI oil. 1,1,1-Trichloroethane is widely used for degreasing IC chips and metal parts. Another important thing to note is that due to the large thermo-optic coefficient of silicon ($1.84x10^{-4}K^{-1}$ [90]) the spectrum shifts from one measurement to another

unless the sample is mounted on a temperature-controlled stage. Since we did not have a temperature-controlled stage to mount our sample on, we used the shift in the mode cut off wavelength of a 100-period long PCW, fabricated alongside the sensors, to calculate the shift due to temperature changes for measurements with different RI oil. Figure 52 shows the effect of temperature drift on the reference spectrum. The figure shows the spectra of a 100-period long butt-coupled PCW at three different times. The spectra shifts by around 55.3 pm in roughly 15 hours. To interpret the data correctly, it is important to compensate for this shift in spectra due to the temperature drift. To compensate for this temperature drift, we would record the reference spectra before each measurement with an RI oil. These reference spectra, taken before each RI oil measurement, allow us to correct for the shift in spectra due to the temperature drift over time.

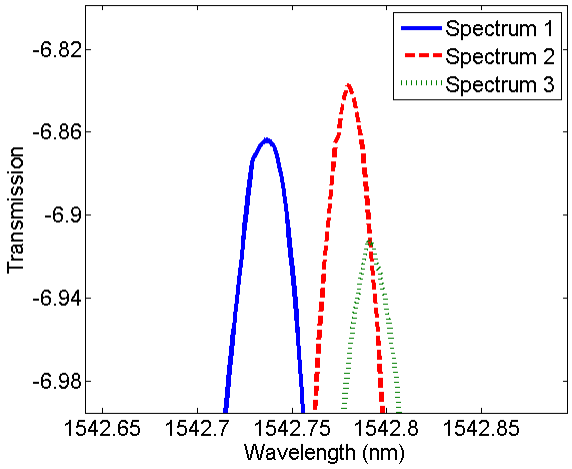

Figure 52: Spectra of a butt-coupled 100-period long PCW at three different times; at night (blue solid), the next morning (red dashed) and the next afternoon (green dotted). The spectra has shifted by around 55.3 pm in around 15 hours.

In Figure 53, we show the spectra obtained from a ridge waveguide in an unbalanced MZI and a 100-period long PCW in an unbalanced MZI Figure. The fringes from the ridge waveguide, in Figure 53(a), are uniformly spaced where as those from the PCW [Figure 53(b)] are not. The constantly changing fringe spacing in

a PCW-based MZI is due to the large dispersion present in a PCW, and the fringe spacing gets smaller and smaller as we probe larger and larger group indexes [12]. The fringes disappear for wavelengths greater than 1565 nm due to the mode cut-off of the PCW in the test arm of the MZI. The mode cut-off of the PCW in the reference arm of the MZI occurs at much larger wavelengths as it is covered with SU-8; the refractive index of SU-8 (1.57 [91]) is greater than that of air (1.0) or oils (n = 1.30 – 1.31). The geometrical parameters (r/a = 0.28 and a = 410 nm) of the PCWs are same for both arms of the MZI.

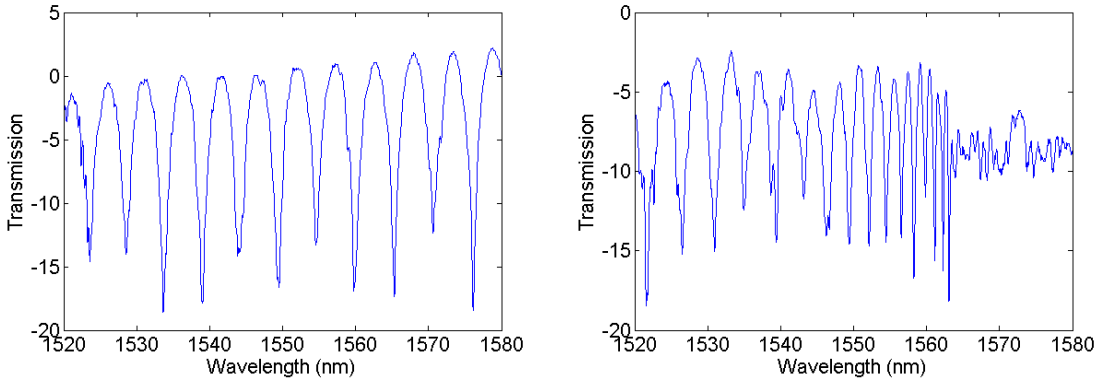

(a) (b)

Figure 53: Fringe spacings for a ridge waveguide (a) and a 100 period PCW (b) based unbalanced MZI. Reduced fringe spacing for the PCW case is due to the reduced group velocity [12].

To calculate the sensitivity of the sensors, we obtained the spectra for three different values of refractive index oils; n = 1.30, 1.305, and 1.31. The obtained spectra are shown in Figure 54 for a ridge waveguide, a 150-period long PCW, a 50-period long PCW (all in an unbalanced MZI configuration), and a straight 100-period long PCW (without MZI).

For a ridge waveguide, we see (in Figure 54(a)) that the spectrum shifts by 0.85 nm for an RI change of 0.01. Thus the sensitivity of a ridge waveguide based sensor, with 105 μm path difference between the two arms of the MZI, is 85 nm/RIU. We

characterized the shift in all the spectral dips (22 in total) in our scanned wavelength range of 1460 nm - 1580 nm, and found that the shift sensitivity is the same for all the dips. This similar shift sensitivity is due to the negligible change (as a function of frequency) in the group index of a ridge waveguide mode as shown in Figure 49. The performance of different sensors (ridge waveguide or PCW) with different lengths of PCW (100a and 150a) and configurations (MZI or no MZI) are presented in Table 7. The first column of the table mentions the coupler type and the length of the PCW. The lengths of the PCWs are mentioned in terms of *a* (period of PC, 410 nm in this case). For the ridge waveguide based sensor a length of $105\mu m$ is mentioned, which refers to the total length difference of the ridge waveguide in the two arms of the unbalanced MZI. The second column refers to the configuration of each sensor; MZI refers to the sensor being in an unbalanced MZI configuration, and No MZI refers to a sensor (which does not employ an MZI) using the shift in the mode cut-off of the fundamental mode of the PCW for sensing. The *Sensitivity* column mentions the raw shift of the feature as a function of RI of the oil. This is the sensitivity that is recorded and also displayed in Figure 54 for some of the sensors. The *Compensated Sensitivity* column mentions the actual sensitivity of the sensor after subtracting the effect of the ridge waveguide in the reference arm of the sensor [12].

Table 7 shows that the performance of sensors with the same length of the PCW, but with different coupler designs, is different. This is due to the fact that our designed *Air Wedge* coupler [79] allows better coupling of light from a ridge waveguide to slow light in a PCW. With better coupling into slow light, we are able to probe larger group indexes that result in improved performance of sensors based on our designed couplers. More details on our coupler design can be seen in Chapter 6. For an unbalanced MZI sensor with a 150-period long PCW (61 μm) in one arm and a ridge waveguide in the other arm, the spectrum shifts by 1.29 nm (see

Table 7: Performance of different RI sensors; *a* refers to the period of PC, which in this case was 410 nm.

Coupler Type and length	Configuration	Sensitivity (nm/RIU)	Compensated Sensitivity (nm/RIU)
AirWedge, 150*a*	MZI	129.54	179.07
Butt Coupled, 150*a*	MZI	109.29	158.82
AirWedge, 100*a*	MZI	121.72	155.01
Butt Coupled, 100*a*	MZI	109.83	143.12
Butt Coupled, 50*a*	MZI	115.16	131.81
Butt Coupled, 100*a*	No MZI	129	129
AirWedge, 100a	No MZI	129	129
RidgeWaveguide, 105 um	MZI	85.26	85.26

Figure 54(b)) resulting in a 129 nm/RIU shift sensitivity. However, when we subtract the effect of the ridge waveguide in the other arm (since the ridge waveguide in the reference arm is also exposed to the RI oils) the actual shift sensitivity comes out to be 179 nm/RIU. Thus, we see a factor of *3.64* enhanced sensitivity over a ridge waveguide based sensor. We have used the spectral dip in the low group velocity region of the PCW to calculate this dip. If we use the spectral dips at lower wavelengths, where the group index is smaller, this shift is much smaller. This smaller shift for smaller group indexes is expected from our discussion above (see Eq. 54), which shows that the phase shift is directly proportional to the group index. Figure 54(b) shows that the two dips for oils with refractive indexes 1.3 and 1.31 (red solid and the blue dotted curve) lie on top of one another. Although it may suggest that our designed sensors also suffer from the same problem as resonance-based sensors with multiple resonances and small FSR, but this can easily be avoided in our case by designing the path difference in the two arms to be much smaller than $105\mu m$ as used in the present case. Hence, our designed sensors do not suffer from the ambiguity arising due to close spacing of resonances as would be the case for microring- or microdisk-based sensors in particular and for

any resonance based sensor in general. We also calculated the shift sensitivity for a 100-period long (41 μm) and a 50-period long (20.5 μm) PCW in an unbalanced MZI (see Figure 54(b) and (c), and Table 7) and found these to be 122 nm/RIU and 115 nm/RIU, which after compensating for the presence of ridge waveguide in the reference arm come to be around 155 nm/RIU and 132 nm/RIU respectively. These spectral shifts for a 100-period long and a 50-period long PCW, indicate a factor of *4.67* and *7.92* enhanced sensitivity over a ridge waveguide-based sensor. The larger enhancement factor observed for smaller length PCW is due to the fact that the losses in a longer PCW are higher. Thus, the group indexes that we can sample in shorter PCWs are greater than that for a longer PCW. In order to compare the performance of our designed sensors with that of a sensor based on the shift of the mode cut-off of a PCW [84], we also characterized the shift in the mode cut-off of a 100-period long PCW and found the shift sensitivity to be around 129 nm/RIU. Another thing to keep in mind is that this number does not change if we use a longer or shorter PCW as the mode cut-off is determined by the PCW parameters and not by the length of the PCW. Comparing this shift sensitivity of 129 nm/RIU (for a sensor based on mode cut-off shift) to the sensitivity of 179 nm/RIU for a 150-period long PCW and 155 nm/RIU for a 100-period long PCW (both used in an unbalanced MZI configuration) proves our earlier assertion that using a sensor based on phase accumulation rather than a shift in a spectral feature (e.g. mode cut-off shift, resonance shift) allows the flexibility to tune the shift sensitivity.

Although the experimentally demonstrated sensitivity enhancement in using a PCW instead of a ridge waveguide for sensing is 7.92, and much less than the theoretically predicted value of three orders of magnitude (see Figure 50), this is not a limitation of our sensor design. With better quality fabrication it should be possible to increase this enhancement factor to 10 even for larger PCWs (e.g. 150 period), as group indexes of 50 have already been demonstrated experimentally

[53] with low loss for a 200-period long PCW. With these high enhancement factors available with a 150-period long PCW, we should be able to increase the shift in spectral dip per RIU from 179 nm/RIU (demonstrated in this work) to around 500 nm/RIU, which is better than any other reported sensor performance.

In conclusion, we have presented a unique design for an integrated optical RI sensor that overcomes the limitations of resonance-based sensors. Our architecture, which is based on phase accumulation rather than a resonance shift, allows tunable sensitivity (spectral shift/RIU) simply by changing the length of the interaction region. Our sensing architecture also allows ease of detection by using unbalanced MZI rather than a balanced one to detect a shift in spectral dip compared to a change in the output intensity. Similarly, by using PCWs operating in their low group velocity region, the actual sensor size can be reduced considerably when compared with a ridge waveguide-based sensors. We showed a factor of 8 improvement in the sensitivity by using a PCW instead of a ridge waveguide. The highest spectral shift reported in this work is around 180 nm/RIU for a 150 period long PCW with the potential to obtain 500 nm/RIU with improved fabrication.

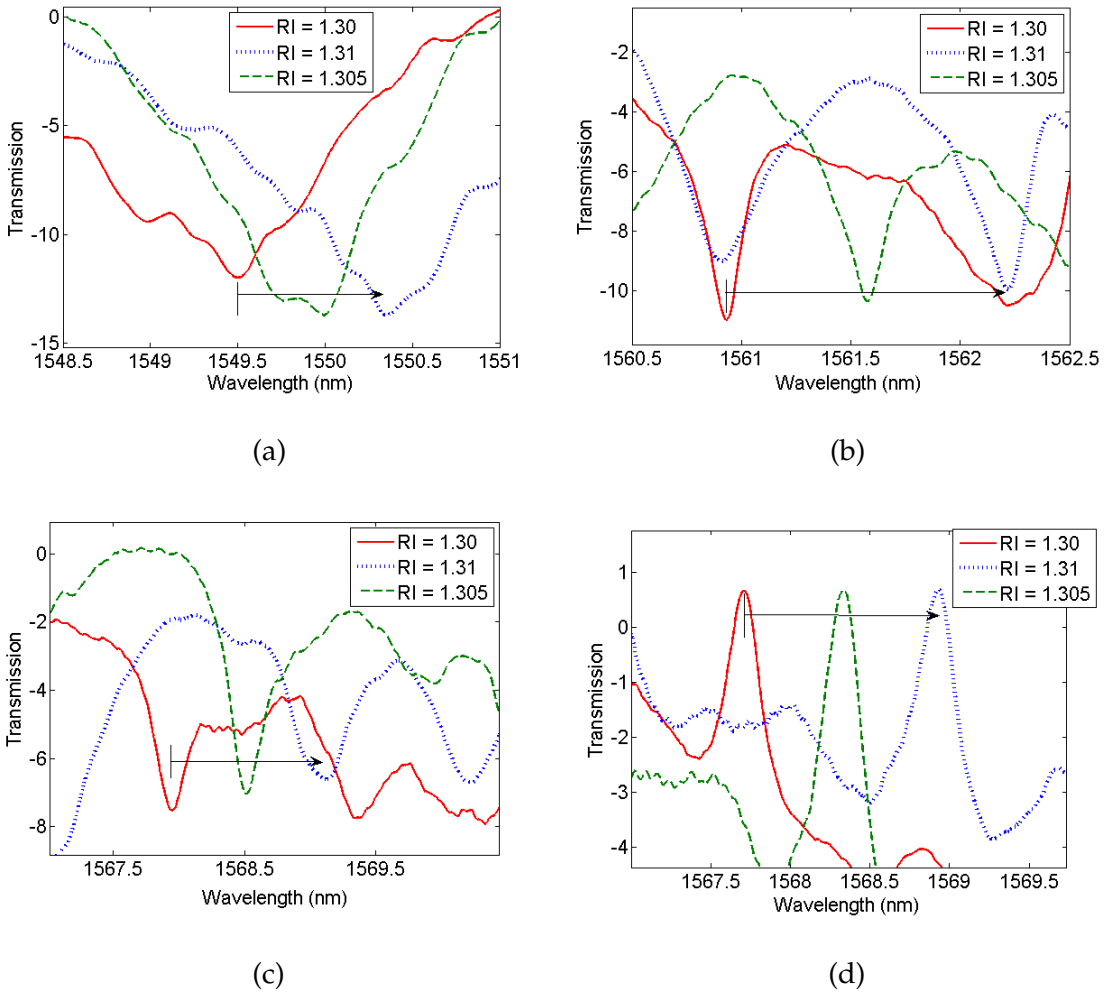

Figure 54: Sensor performance for (a) a ridge waveguide-based unbalanced MZI, (b) a 150-period long PCW-based unbalanced MZI, (c) a 50-period long PCW-based unbalanced MZI, and (d) a 100-period long PCW without MZI. The spectra in each case is taken for three different values of hole/cladding RI: n = 1.3 (red solid), n = 1.305 (green dashed), and n = 1.31 (blue dotted).

CHAPTER IX

FUTURE DIRECTIONS

In previous chapters, I have presented my work in the area of photonic crystal waveguides (PCWs). I have looked into some of the issues with the use of PCWs for integrated optics applications. I have also presented a sensing architecture using these PCWs. PCWs generated huge interest in the integrated optics community due to the unique features, such as: dispersion engineering, existence of slow light, and the huge dispersion available in these structures. These unique properties have been the corner stone of all the work in this field, as such properties do not exist in other waveguide platforms. However, recently the interest in using PCWs has been declining, and the interest in only a few of the initially thought of applications remain. The biggest factor contributing to this decline in interest is the losses associated with propagation of light in PCWs even in the intrinsically loss-less region of operation below the light line. These losses are attributed to the imperfections arising because of current limitations of fabrication. For example, Vlasov et al. [92] have reported the losses in a PCW to be around 8 times more than a silicon ridge waveguide. This factor of 8 higher loss is for frequency just below the light line where the group velocity is still relatively high. At lower group velocities the losses are still higher. For example, a group index of 230 has only been measured for a relatively short PCW of 46 periods only [67]. 3D PCWs can help by eliminating the light line issues in the 2D PCWs, but even band gap confinement in the third direction will not reduce the fabricated induced losses. These high propagation losses have largely reduced the application of PCWs to areas where only short length of PCWs is required. The most important next step

would be to reduce the propagation losses in these PCWs.

A logical extension of my work in using PCWs for refractive index sensing will be to design sensors for specific chemical/biological application. This can include detecting viruses and pathogens for applications in medical industry, or detecting explosives or other hazardous chemicals in homeland security applications. For these applications we need to cover the sensing element with coatings that bind specifically to a single chemical or biological agent. Another potential application of my designed sensor will be in areas requiring strict control of percentage of ingredients in a liquid mixture or to keep track of degradation of liquids. Application areas for such an application will include food industry, where we can keep track of the health of frying oils, or making sure that a drink consists of exact percentage of different liquid ingredients. Pharmaceutical industry will also benefit from such a compact sensor to keep track of percentage of different mixtures.

Another application of using PCWs operating at low group velocities in an unbalanced MZI architecture can be in making compact electro-optic and thermo-optic modulators. An added fabrication step for realizing these applications is to deposit metals in close proximity to the PCWs. It is expected that this architecture of slow light PCWs in an unbalanced MZI will result in a more compact and a wider bandwidth modulators than those reported earlier in literature [39, 93, 94].

REFERENCES

[1] M. Askari, C. M. Reinke, and A. Adibi, "Modeling photonic crystal waveguides as dispersive homogeneous media for efficient analysis of wave propagation," under preparation.

[2] M. Askari, M. Soltani, B. Momeni, and A. Adibi, "Systematic design of wide bandwidth photonic crystal waveguide bends with high transmission and low dispersion," *IEEE Journal of lightwave technology*, vol. 28, pp. 1707–1713, 2010.

[3] M. Askari, B. Momeni, S. Yegnanarayanan, and A. Adibi, "Group velocity independent coupling of light into photonic crystal waveguides," under preparation.

[4] [Online]. Available: http://nanolithography.gatech.edu/zep520acurve.html

[5] H. Benisty, S. Olivier, C. Weisbuch, M. Agio, M. Kafesaki, C. Soukoulis, M. Qiu, M. Swillo, A. Karlsson, B. Jaskorzynska *et al.*, "Models and measurements for the transmission of submicron-width waveguide bends defined in two-dimensional photonic crystals," *Quantum Electronics, IEEE Journal of*, vol. 38, no. 7, pp. 770–785, 2002.

[6] N. Moll and G. Bona, "Bend design for the low-group-velocity mode in photonic crystal-slab waveguides," *Applied Physics Letters*, vol. 85, no. 19, pp. 4322–4324, 2004.

[7] A. Chutinan, M. Okano, and S. Noda, "Wider bandwidth with high transmission through waveguide bends in two-dimensional photonic crystal slabs," *Applied Physics Letters*, vol. 80, p. 1698, 2002.

[8] M. Askari and A. Adibi, "Wide bandwidth photonic crystal waveguide bends," in *Proceedings of SPIE*, vol. 7609, Feb. 2010, pp. 760 918–1–11.

[9] M. Koshiba, Y. Tsuji, and S. Sasaki, "High-performance absorbing boundary conditions for photonic crystal waveguide simulations," *IEEE Microwave and Wireless Components Letters*, vol. 11, no. 4, pp. 152–154, APR 2001.

[10] J. Berenger, "A perfectly matched layer for the absorption of electromagnetic waves," *Journal of computational physics*, vol. 114, no. 2, pp. 185–200, 1994.

[11] M. Askari, B. Momeni, C. M. Reinke, and A. Adibi, "Adiabatically matched perfectly matched layer for absorbing slow group velocity modes in photonic crystal waveguides," in *OSA Annual*, 2010.

[12] M. Askari, S. Yegnanarayanan, and A. Adibi, "Photonic crystal waveguide based sensor," in *Proceedings of SPIE*, San Fransisco, CA, Jan. 2011.

[13] E. Yablonovitch, "Inhibited spontaneous emission in solid-state physics and electronics," *Physical Review Letters*, vol. 58, no. 20, pp. 2059–2062, 1987.

[14] S. John, "Strong localization of photons in certain disordered dielectric superlattices," *Physical Review Letters*, vol. 58, no. 23, pp. 2486–2489, 1987.

[15] J. Lourtioz, H. Benisty, V. Berger, J. Gerard, D. Maystre, and A. Tchelnokov, *Photonic crystals: towards nanoscale photonic devices*. Springer Verlag, 2008.

[16] K. Sakoda, *Optical properties of photonic crystals*. Springer Verlag, 2005.

[17] J. Joannopoulos, R. Meade, and J. Winn, *Photonic crystals: molding the flow of light*. Princeton Univ Press, 2005.

[18] K. S. Yee, "Numerical solution of initial boundary value problems involving maxwells equations in isotropic media," *IEEE Transactions On Antennas And Propagation*, vol. 14, no. 3, pp. 302–&, 1966.

[19] A. Taflove and S. Hagness, *Computational electrodynamics: the finite-difference time-domain method*. Artech House Norwood, MA, 2005.

[20] D. Maystre, "Diffraction gratings," *SPIE Milestone Series, Bellingham: SPIE-The International Society for Optical Engineering,— c1993, edited by Maystre, D.*, 1993.

[21] M. Moharam and T. Gaylord, "Rigorous coupled-wave analysis of metallic surface-relief gratings," *Journal of the Optical Society of America A*, vol. 3, no. 11, pp. 1780–1787, 1986.

[22] R. Petit and L. Botten, *Electromagnetic theory of gratings*. Springer-Verlag Berlin, 1980.

[23] M. Kesler, J. Maloney, B. Shirley, and G. Smith, "Antenna design with the use of photonic band-gap materials as all-dielectric planar reflectors," *Microwave and Optical Technology Letters*, vol. 11, no. 4, pp. 169–174, 1996.

[24] S. Noda, M. Imada, M. Okano, S. Ogawa, M. Mochizuki, and A. Chutinan, "Semiconductor three-dimensional and two-dimensional photoniccrystals and devices," *IEEE Journal of Quantum Electronics*, vol. 38, no. 7, pp. 726–735, 2002.

[25] A. Adibi, Y. Xu, R. Lee, A. Yariv, and A. Scherer, "Properties of the slab modes in photonic crystal optical waveguides," *Journal of lightwave technology*, vol. 18, no. 11, p. 1554, 2000.

[26] Y. Akahane, T. Asano, B. Song, and S. Noda, "High-q photonic nanocavity in a two-dimensional photonic crystal," *nuclear magnetic resonance*, vol. 414, pp. 883–887, 2001.

[27] H. Benisty, H. De Neve, and C. Weisbuch, "Impact of planar microcavity effects on light extraction-part i: basic concepts and analytical trends," *IEEE Journal of Quantum Electronics*, vol. 34, no. 9, pp. 1612–1631, 1998.

[28] ——, "Impact of planar microcavity effects on light extraction-part ii: selected exact simulations and role of photon recycling," *IEEE Journal of Quantum Electronics*, vol. 34, no. 9, pp. 1632–1643, 1998.

[29] K. Inoue, M. Sasada, J. Kawamata, K. Sakoda, and J. Haus, "A two-dimensional photonic crystal laser," *Japanese Journal of Applied Physics Part 2 Lettersw*, vol. 38, pp. 157–159, 1999.

[30] H. Park, S. Kim, S. Kwon, Y. Ju, J. Yang, J. Baek, S. Kim, and Y. Lee, "Electrically driven single-cell photonic crystal laser," *Science*, vol. 305, no. 5689, p. 1444, 2004.

[31] H. Kosaka, T. Kawashima, A. Tomita, M. Notomi, T. Tamamura, T. Sato, and S. Kawakami, "Superprism phenomena in photonic crystals," *Physical Review B*, vol. 58, no. 16, pp. 10 096–10 099, 1998.

[32] B. Momeni, J. Huang, M. Soltani, M. Askari, S. Mohammadi, M. Rakhshandehroo, and A. Adibi, "Compact wavelength demultiplexing using focusing negative index photonic crystal superprisms," *Optics Express*, vol. 14, no. 6, pp. 2413–2422, 2006.

[33] T. Matsumoto, S. Fujita, and T. Baba, "Wavelength demultiplexer consisting of photonic crystal superprism and superlens," *Optics Express*, vol. 13, no. 26, pp. 10 768–10 776, 2005.

[34] B. Momeni, E. Hosseini, M. Askari, M. Soltani, and A. Adibi, "Integrated photonic crystal spectrometers for sensing applications," *Optics Communications*, 2009.

[35] M. Notomi, "Theory of light propagation in strongly modulated photonic crystals: Refractionlike behavior in the vicinity of the photonic band gap," *Physical Review B*, vol. 62, no. 16, pp. 10 696–10 705, 2000.

[36] T. Krauss, "Why do we need slow light?" *Nature Photonics*, vol. 2, no. 8, pp. 448–450, 2008.

[37] ——, "Slow light in photonic crystal waveguides," *Journal of Physics D Applied Physics*, vol. 40, no. 9, p. 2666, 2007.

[38] J. McMillan, X. Yang, N. Panoiu, R. Osgood, and C. Wong, "Enhanced stimulated raman scattering in slow-light photonic crystal waveguides," *Optics letters*, vol. 31, no. 9, pp. 1235–1237, 2006.

[39] L. Gu, W. Jiang, X. Chen, and R. Chen, "Thermooptically tuned photonic crystal waveguide silicon-on-insulator mach–zehnder interferometers," *IEEE Photonics Technology Letters*, vol. 19, no. 5, pp. 342–344, 2007.

[40] Z. Dutton, N. Ginsberg, C. Slowe, and L. Hau, "The art of taming light: ultra-slow and stopped light," *Europhysics News*, vol. 35, no. 2, pp. 33–39, 2004.

[41] L. Hau, S. Harris, Z. Dutton, and C. Behroozi, "Light speed reduction to 17 metres per second in an ultracold atomic gas," *Nature*, vol. 397, no. 6720, pp. 594–598, 1999.

[42] M. Bigelow, N. Lepeshkin, and R. Boyd, "Superluminal and slow light propagation in a room-temperature solid," *Science*, vol. 301, no. 5630, p. 200, 2003.

[43] A. Yariv, Y. Xu, R. Lee, and A. Scherer, "Coupled-resonator optical waveguide: a proposal and analysis," *Optics Letters*, vol. 24, no. 11, pp. 711–713, 1999.

[44] A. Melloni, F. Morichetti, and M. Martinelli, "Linear and nonlinear pulse propagation in coupled resonator slow-wave optical structures," *Optical and Quantum Electronics*, vol. 35, no. 4, pp. 365–379, 2003.

[45] R. Grover, V. Van, T. Ibrahim, P. Absil, L. Calhoun, F. Johnson, J. Hryniewicz, and P. Ho, "Parallel-cascaded semiconductor microring resonators for high-order and wide-fsr filters," *Journal of Lightwave Technology*, vol. 20, no. 5, p. 872, 2002.

[46] O. Painter, K. Srinivasan, and P. Barclay, "Wannier-like equation for the resonant cavity modes of locally perturbed photonic crystals," *Physical Review B*, vol. 68, no. 3, p. 35214, 2003.

[47] Z. Li and K. Ho, "Light propagation in semi-infinite photonic crystals and related waveguide structures," *Physical Review B*, vol. 68, no. 15, p. 155101, 2003.

[48] J. E. Heebner, R. Boyd, and Q. Park, "Slow light, induced dispersion, enhanced nonlinearity, and optical solitons in a resonator-array waveguide," *Physical Review E*, vol. 65, no. 3, p. 36619, 2002.

[49] J. Poon, J. Scheuer, Y. Xu, and A. Yariv, "Designing coupled-resonator optical waveguide delay lines," *Journal of the Optical Society of America B*, vol. 21, no. 9, pp. 1665–1673, 2004.

[50] F. Xia, L. Sekaric, and Y. Vlasov, "Ultracompact optical buffers on a silicon chip," *Nature Photonics*, vol. 1, no. 1, pp. 65–71, 2007.

[51] F. Morichetti, A. Melloni, C. Canavesi, F. Persia, M. Martinelli, and M. Sorel, "Tunable slow-wave optical delay-lines," *Slow and Fast Light*, 2006.

[52] D. Leuenberger, J. Yao, M. Lee, and M. Wu, "Experimental demonstration of mems-tunable slow light in silicon microdisk resonators," *Slow and Fast Light*, 2006.

[53] J. Li, T. White, L. O'Faolain, A. Gomez-Iglesias, and T. Krauss, "Systematic design of flat band slow light in photonic crystal waveguides," *Optics Express*, vol. 16, no. 9, pp. 6227–6232, 2008.

[54] Y. Hamachi, S. Kubo, and T. Baba, "Slow light with low dispersion and nonlinear enhancement in a lattice-shifted photonic crystal waveguide," *Optics Letters*, vol. 34, no. 7, pp. 1072–1074, 2009.

[55] L. Dai and C. Jiang, "Photonic crystal slow light waveguides with large delay-bandwidth product," *Applied Physics B-Lasers And Optics*, vol. 95, no. 1, pp. 105–111, Apr. 2009.

[56] T. Baba, H. Sasaki, J. Adachi, T. Kawasaki, and D. Mori, "Dispersion-free slow light pulse and its functionalities," in *Proceedings of SPIE*, vol. 7226, 2009, p. 722604.

[57] T. Baba, T. Kawaaski, H. Sasaki, J. Adachi, and D. Mori, "Large delay-bandwidth product and tuning of slow light pulse in photonic crystal coupled waveguide," *Optics Express*, vol. 16, no. 12, pp. 9245–9253, 2008.

[58] M. N. O. Sadiku, *Elements of Electromagnetics*. Oxford University Press, 1995.

[59] N. W. Ashcroft and D. N. Mermin, *Solid State Physics*, 1st ed. Toronto: Thomson Learning, January 1976.

[60] Y. Liu, "Fourier analysis of numerical algorithms for the maxwell's equations," *J. Computational Physics*, vol. 124, pp. 396–416, 1996.

[61] C. M. Reinke, "Design, simulation, and characterization toolset for nano-scale photonic crystal devices," Ph.D. dissertation, Georgia Institute of Technology, 2009.

[62] D. Merewether, R. Fisher, and F. Smith, "On implementing a numeric huygen's source scheme in a finite difference program to illuminate scattering bodies," *IEEE Transactions on Nuclear Science*, vol. 27, pp. 1829–1833, 1980.

[63] Z. Sacks, D. Kingsland, R. Lee, and J. Lee, "A perfectly matched anisotropic absorber for use as an absorbing boundary condition," *Antennas and Propagation, IEEE Transactions on*, vol. 43, no. 12, pp. 1460–1463, 1995.

[64] S. A. Campbell, *The Science and Engineering of Microelectronic Fabrication*. Oxford University Press, 1996.

[65] [Online]. Available: http://www.dowcorning.com/content/publishedlit/11-1547e-01.pdf

[66] T. Nishida, M. Notomi, R. Iga, and T. Tamamura, "Quantum Wire Fabrication by E-Beam Elithography Using High-Resolution and High-Sensitivity E-Beam Resist ZEP-520," *Jpn. J. Appi. Phys. Vol*, vol. 31, pp. 4508–4514, 1992.

[67] R. Jacobsen, A. Lavrinenko, L. Frandsen, C. Peucheret, B. Zsigri, G. Moulin, J. Fage-Pedersen, and P. Borel, "Direct experimental and numerical determination of extremely high group indices in photonic crystal waveguides," *Optics express*, vol. 13, no. 20, pp. 7861–7871, 2005.

[68] M. Askari and A. Adibi, "Analysis of pulse propagation in photonic crystal wavegiudes for optical delay line design," in *Optics in the Southeast (OISE)-2005*, Charlotte, NC, 2005.

[69] T. Sondergaard and K. H. Dridi, "Energy flow in photonic crysal waveguides," *Physical Review B*, vol. 61, pp. 15 688–15 696, 2000.

[70] A. Mekis, J. Chen, I. Kurland, S. Fan, P. Villeneuve, and J. Joannopoulos, "High transmission through sharp bends in photonic crystal waveguides," *Physical Review Letters*, vol. 77, no. 18, pp. 3787–3790, 1996.

[71] S. Boscolo, C. Conti, M. Midrio, and C. Someda, "Numerical analysis of propagation and impedance matching in 2d photonic crystal waveguides with finite length," *Journal of Lightwave Technology*, vol. 20, no. 2, pp. 304–310, 2002.

[72] C. Pollock, *Fundamentals of optoelectronics*. Irwin Chicago, 1995.

[73] M. Askari, B. Momeni, C. M. Reinke, and A. Adibi, "Absorbing boundary conditions for low group velocity electromagnetic waves in photonic crystals," *Applied Optics*, accepted.

[74] M. Askari, B. Momeni, M. Soltani, and A. Adibi, "Optimal photonic crystal bends with linear dispersion," in *Proceedings of SPIE*, vol. 6480, 2007, p. 64800Z.

[75] M. Askari and A. Adibi, "Experimental demonstration of large bandwidth photonic crystal waveguide bends," under preparation.

[76] M. Gnan, I. Ntakis, P. Pottier, R. De La Rue, and P. Bassi, "Systematic investigation of misalignment effects at junctions between feeder waveguide and photonic crystal channel waveguide," *Journal of Optical Networking*, vol. 6, no. 2, pp. 90–101, 2007.

[77] P. Bienstman, S. Assefa, S. Johnson, J. Joannopoulos, G. Petrich, and L. Kolodziejski, "Taper structures for coupling into photonic crystal slab waveguides," *Journal of the Optical Society of America B*, vol. 20, no. 9, pp. 1817–1821, 2003.

[78] A. Talneau, P. Lalanne, M. Agio, and C. Soukoulis, "Low-reflection photonic-crystal taper for efficient coupling between guide sections of arbitrary widths," *Optics letters*, vol. 27, no. 17, pp. 1522–1524, 2002.

[79] M. Askari, B. Momeni, S. Yegnanarayanan, A. Eftekhar, and A. Adibi, "Efficient coupling of light into the planar photonic crystal waveguides in the slow group velocity regime," in *Proceedings of SPIE*, vol. 6901, 2008, p. 69011A.

[80] A. Mekis, S. Fan, and J. Joannopoulos, "Absorbing boundary conditions for fdtd simulations of photoniccrystal waveguides," *IEEE Microwave and Guided Wave Letters*, vol. 9, no. 12, pp. 502–504, 1999.

[81] Y. Hsue and T. Yang, "Applying a modified plane-wave expansion method to the calculations of transmittivity and reflectivity of a semi-infinite photonic crystal," *Physical Review E*, vol. 70, no. 1, p. 16706, 2004.

[82] B. Momeni and A. Adibi, "Adiabatic matching stage for coupling of light to extended bloch modes of photonic crystals," *Applied Physics Letters*, vol. 87, p. 171104, 2005.

[83] C. Barrios, "Optical slot-waveguide based biochemical sensors," *Sensors*, vol. 9, no. 6, pp. 4751–4765, 2009.

[84] N. Skivesen, A. Têtu, M. Kristensen, J. Kjems, L. H. Frandsen, and P. I. Borel, "Photonic-crystal waveguide biosensor," *Opt. Express*, vol. 15, no. 6, pp. 3169–3176, 2007. [Online]. Available: http://www.opticsexpress.org/abstract.cfm?URI=oe-15-6-3169

[85] K. De Vos, I. Bartolozzi, E. Schacht, P. Bienstman, and R. Baets, "Silicon-on-insulator microring resonator for sensitive and label-free biosensing," *Optics Express*, vol. 15, no. 12, pp. 7610–7615, 2007.

[86] M. Askari and A. Adibi, "Refractive index sensing using photonic crystal waveguides in a mach-zahnder interferometer configuration," *Optics Express*, under preparation.

[87] C. Pollock and M. Lipson, *Integrated photonics*. Springer Netherlands, 2003.

[88] G. M. Hale and M. R. Querry, "Optical constants of water in the 200-nm to 200-µm wavelength region," *Appl. Opt.*, vol. 12, no. 3, pp. 555–563, 1973. [Online]. Available: http://ao.osa.org/abstract.cfm?URI=ao-12-3-555

[89] [Online]. Available: http://refractiveindex.info

[90] G. Ghosh, *Handbook of thermo-optic coefficients of optical materials with applications*. Academic Press: San Diego, 1998.

[91] A. Borreman, S. Musa, A. Kok, M. Diemeer, and A. Driessen, "Fabrication of polymeric multimode waveguides and devices in su-8 photoresist using selective polymerization." pp. 83–86, 2002. [Online]. Available: http://doc.utwente.nl/58192/

[92] S. McNab, N. Moll, and Y. Vlasov, "Ultra-low loss photonic integrated circuit with membrane-type photonic crystal waveguides," *Optics Express*, vol. 11, no. 22, pp. 2927–2939, 2003.

[93] L. Gu, W. Jiang, X. Chen, L. Wang, and R. Chen, "High speed silicon photonic crystal waveguide modulator for low voltage operation," *Applied physics letters*, vol. 90, p. 071105, 2007.

[94] Q. Xu, B. Schmidt, S. Pradhan, and M. Lipson, "Micrometre-scale silicon electro-optic modulator," *Nature*, vol. 435, no. 7040, pp. 325–327, 2005.

VITA

Askari was born in Abbottabad, Pakistan. He received his B.E. degree in Electrical Engineering from College of Electrical and Mechanical Engineering (CEME), National University of Sciences and Technology (NUST) Pakistan in 2001. He received his M.Sc. in Electrical Engineering from Georgia Institute of Technology in 2007. His research interests include wave propagation in periodic medium, optical fibers, light generation and detection, and non-linear optics. His other interest includes playing cricket, squash, and badminton. He also enjoys reading about comparative study of religions.